

Measurement of ω mesons
via radiative decay mode
in Au+Au collisions at $\sqrt{s_{NN}}=200\text{GeV}$

Misaki Ouchida
(M052187)

Hiroshima University

Abstract

The modification of experimentally observable properties of vector mesons such as mass and width, when embedded in a hot and dense medium created by the relativistic heavy-ion collisions, is one of the most fundamental research issues in hadron physics. It could be linked to the chiral symmetry restoration, that is, the intricate key for searching the source of hadron masses. The radiative decay mode of ω mesons ($\omega \rightarrow \pi^0\gamma$) is a promising approach for this study. Since the radiative reaction is likely to less interact in the medium than charged particle's reaction due to its electromagnetic coupling, it is a clean way to investigate the properties. Furthermore, it has a large branching ratio, about 9% and doesn't have to concern the contamination of ρ mesons that all e^+e^- experiments suffer from.

We measure ω mesons via radiative decay mode in Au+Au collisions at C.M.S. collision energy per nucleon pair of 200GeV taken at the PHENIX experiment using the Relativistic Heavy Ion Collider (RHIC). The RHIC is proven to have an enough energy for researching the chiral phase transition leading to the expected mass modification. Since it is very challenging to search specific particles in the high multiple collisions, the simulation is carried out in advance to calculate an acceptance and to check a multiplicity dependence. The main issue of this analysis is the huge combinatorial background inevitable for reconstructing particles from the three-body decay mode. So we emphasis on doing the feasibility study using both simulation and real data to search the best parameters such as momentum and energy for selecting π^0 and γ before reconstructing ω . Finally, we find best values for each parameter that can improve S/\sqrt{B} . After introducing these parameters, reconstructed ω invariant mass spectra as a function of ω transverse momentum are shown and discussed. A further improvement of ω identification and how to approach the low momentum region where the in-medium modification mainly dominate are considered.

Contents

1	Introduction	1
1.1	Chiral Symmetry Restoration	3
1.2	Low Mass Vector Mesons	6
1.2.1	Medium Modification	6
1.2.2	Current Status	9
1.3	Motivation	15
2	Experimental Setup	17
2.1	RHIC	17
2.2	PHENIX Detector	19
2.2.1	Global Detectors	21
2.2.2	Muon Arm Detectors	23
2.2.3	Central Arm Detectors	24
2.2.4	Electro Magnetic Calorimeter	27
2.3	Computing	33
3	Analysis	36
3.1	Quest for ω mesons	36
3.2	Data Set	38
3.3	Simulation	39
3.3.1	Event Generator	39
3.3.2	Detector Simulation	40
3.3.3	Multiplicity Dependence	42
3.3.4	Cut Optimization	47
3.3.5	Feasibility	53
3.4	Signal Selection	60
3.4.1	Trigger	60
3.4.2	Photon Identification	62

3.4.3	Distribution of π^0 Invariant Mass	65
3.4.4	Best Cuts for Reconstructing ω	67
4	Results and Discussion	68
4.1	Invariant Mass Spectra	68
4.2	Background Consideration	72
4.2.1	Combinatorial Background	72
4.2.2	Mixed Events Trail	74
4.3	Outlook	80
5	Conclusion	81
A	Kinematics	83

Chapter 1

Introduction

The goal of the relativistic heavy ion physics is to explore nature's most basic ingredients and phenomena. Today, nuclear matter is said to be constructed by the most fundamental particle, quarks and leptons. Quarks themselves can't be 'liberated' due to gluons that holds together them via the strong force except in *the extreme conditions*.

The state of the nuclear matter is described by the Quantum Chromodynamics (QCD), the modern theory of the strong interaction. The QCD exhibits a property called the asymptotic freedom[1], that is, the coupling strength of gluons decreases with increasing energy and momentum. This is the clue that the heavy ion physics stand for. As nuclear matter is heated and compressed, hadrons occupy more and more of the available space. Eventually they start to overlap and the initially confined quarks and gluons begin to 'percolate' between the hadrons thus being 'liberated'! This state of matter, the hot and dense fireball made of 'liberated' quarks and gluons is commonly called as the Quark Gluon Plasma (QGP).

This simple picture has originally provided the basis for models of the quark-hadron transition and has been essentially confirmed by numerical QCD lattice calculations at finite temperature[2]. The Figure 1.1 shows a sketch of the QCD phase diagram. Although the phase boundary between the hadron matter and the QGP is not well known, lattice calculations gave an estimation of the critical temperature T_c and the baryon density needed for the QGP creation. From there we can estimate that T_c is about up to 170 MeV and the density is approximately from 5 to 20 times of the normal nuclear matter . However, the systematic error of the lattice result is not known since it is unattainable using the reweighting method[2] to consider

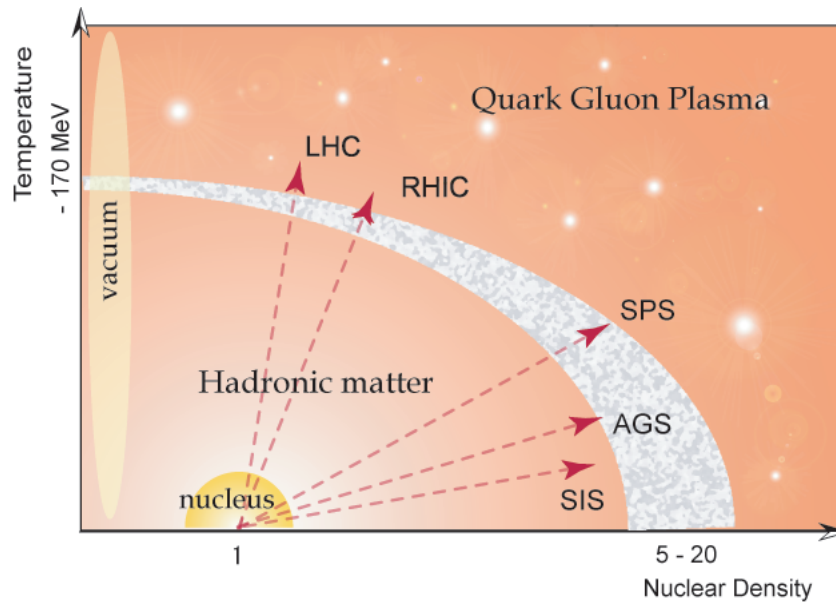


Figure 1.1: Sketch of the QCD phase diagram

the volume $V \rightarrow \infty$ when calculating the nuclear density going to 0.

Some relativistic heavy ion collisions were conducted already and some are still in operation or in preparation. The Heavy Ion Synchrotron (SIS) ($\sqrt{s} \simeq 2A$ GeV) at GSI in Darmstadt, the Alternating Gradient Synchrotron (AGS) ($\sqrt{s} \simeq 5A$ GeV) at the Brookhaven National Laboratory (BNL) in New York and the Super Proton Synchrotron (SPS) ($\sqrt{s} \simeq 20A$ GeV) at CERN in Geneva began in mid 80's. The Relativistic Heavy Ion Collider (RHIC) ($\sqrt{s} = 200A$ GeV) at the BNL has been ongoing since 2000 and the Large Hadron Collider (LHC) ($\sqrt{s} \sim 1.5A$ TeV) at CERN is planned to operate from 2007. According to the model predictions[3], RHIC and SPS energy are indeed lying on the phase boundary. AGS is below the boundary line, however, it is not excluded that the fireball in the initial state appears in the deconfined phase since the initial energy density expected at AGS is of the order of $1 \text{ GeV}/\text{fm}^3$ thus, it is larger than the critical energy density along the boundary. The LHC is hoped for crossing the boundary in the near future.

1.1 Chiral Symmetry Restoration

There are two fundamental properties of the QGP. The one is the deconfinement explained previously, the other is *Chiral Symmetry Restoration*.

Chirality, coming from the Greek word " $\chi\epsilon\iota\rho$ " has the meaning of "hand" [4]. An object or a system has *chirality* if it differs from its mirror image. Such objects then come in two forms, *L* (left-handed) and *R* (right-handed), which are mirror images of each other. The Figure 1.2 shows a image of an object having both *L* and *R*. If a particle has mass, both *L* and *R* components must exist. The reason is that massive particles travel slower than the speed of light and a particle that appears *L* in a particular reference frame will look *R* from a reference frame moving faster than the particle (a bird in the Figure 1.2). That means, *chirality* is not conserved; in a massless world *chirality* is conserved, but this is sufficient but not necessary condition.

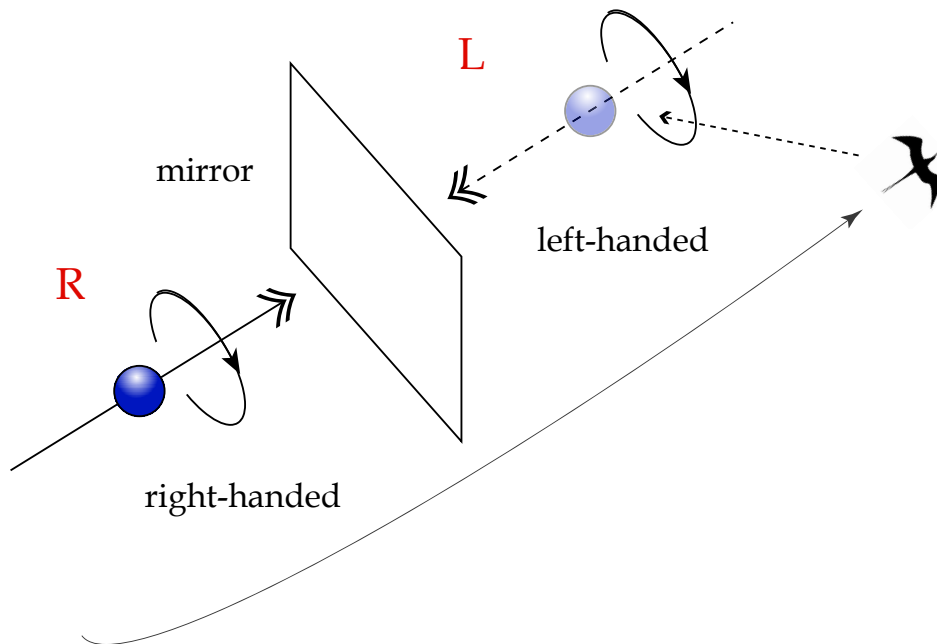


Figure 1.2: Image of the Chiral Symmetry

In QCD, it can be encoded in following Lagrangian[5]

$$\mathcal{L}_{QCD} = -\frac{1}{4}F_{\mu\nu}^{(a)}F^{(a)\mu\nu} + i\sum_q\bar{\psi}_q^i\gamma^\mu(D_\mu)_{ij}\psi_q^j - \sum_q m_q\bar{\psi}_q^j\psi_{qi}, \quad (1.1)$$

$$F_{\mu\nu}^{(a)} = \partial_\mu A_\nu^a - \partial_\nu A_\mu^a - g_s f_{abc}A_\mu^b A_\nu^c, \quad (1.2)$$

$$(D_\mu)_{ij} = \delta_{ij}\partial_\mu + ig_s\sum_a\frac{\lambda_{i,j}^a}{2}A_\mu^a, \quad (1.3)$$

where g_s is the QCD coupling constant, and the f_{abc} are the structure constants of the SU(3) algebra. The $\psi_q^i(x)$ are the 4-component Dirac spinors associated with each quark field of 3 color i and flavor q , and the $A_\mu^a(x)$ are the 8 gluon fields.

Let us explain roughly the Equation (1.1). The first term, $\frac{1}{4}F_{\mu\nu}^{(a)}F^{(a)\mu\nu}$, corresponds to the free gluon field, the second term, $i\sum_q\bar{\psi}_q^i\gamma^\mu(D_\mu)_{ij}\psi_q^j$, corresponds to the interaction of quark in the gluon field and the last term, $\sum_q m_q\bar{\psi}_q^j\psi_{qi}$, corresponds to the free quarks of mass m_q in a rest state. m_q represents the diagonal matrix of current quark masses,

$$m_q = \begin{pmatrix} m_u & & & \\ & m_d & & \\ & & m_s & \\ & & & \ddots \end{pmatrix}, \quad (1.4)$$

which are parameters of the Standard Model. With $m_u, m_d, m_s \simeq 4, 7, 150$ MeV and $m_c, m_b, m_t \simeq 1.5, 4.5, 175$ GeV. There is an obvious separation into sectors of 'light' and 'heavy' quarks.

Chiral symmetry of QCD means that all states have a chiral partner with opposite parity and equal mass. But in the real world, the mass term is not 0 as above so then a mass of a chiral partner is not equal to an associate particle. For instance, ρ ($J^P = 1^-$) $m=770$ MeV has a chiral partner as a_1 ($J^P = 1^+$) $m=1250$ MeV and $N(1/2^+)$ $m=940$ MeV has a chiral partner as $N^*(1/2^-)$ $m=1535$ MeV. The difference is too large to be explained by the small current quark masses. It can be concluded that the chiral symmetry is spontaneously broken and taking it conversely, constituent quark masses can be generated by the spontaneous breaking of the chiral symmetry. It is said that the structure of the lowest-mass hadrons (involved the light-quark sector comprised of u, d, s quarks) is largely determined by chiral symmetry

and its dynamical breaking in the physical vacuum. And many models link the hadron masses to the quark condensate.

In the physical vacuum, quarks and gluons condense giving rise to non-vanishing vacuum expectation values $\langle\bar{\psi}\psi\rangle$ [7], also called *condensate*, that is their average, mathematical expectation value in the vacuum. Let us consider the one of such *condensate* for quarks, the quark condensate $\langle\bar{q}q\rangle$. The Figure 1.3 is a three dimension picture showing the correlation between the quark condensate and QCD phase diagram (see the Figure 1.1).

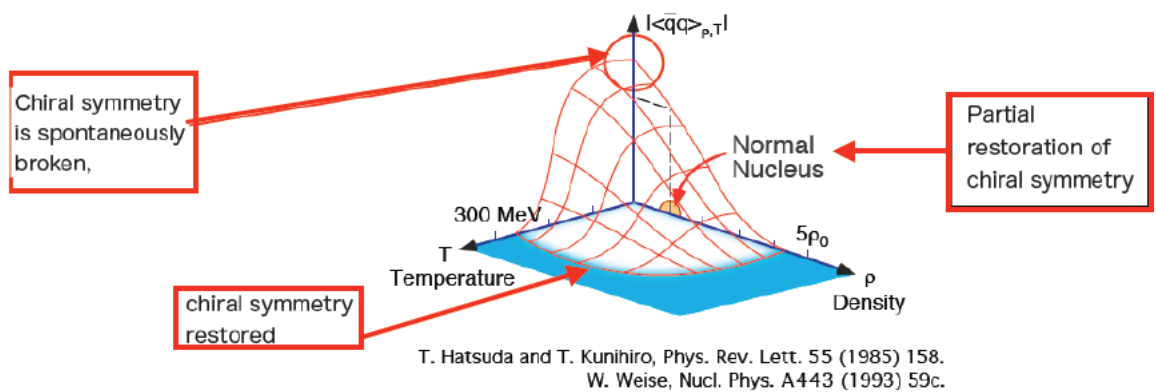


Figure 1.3: The quark condensate and QCD phase diagram [8]

In the case of QCD, if the chiral symmetry is spontaneously broken, the quark condensate is non-zero and said to be: $\langle\bar{q}q\rangle \approx 250 \text{ MeV}^3$. At high temperatures or high densities (the blue field in the Figure 1.3), numerical QCD calculations predict that the quark condensate vanishes: $\langle\bar{q}q\rangle \rightarrow 0$, i.e. chiral symmetry is restored in this region. This means, there is a transition of the system that constitute mass when it's going to *the extreme condition*. We will discuss the probe of the Chiral Symmetry Restoration in the next section.

1.2 Low Mass Vector Mesons

Low-mass vector mesons are considered the most sensitive probe of chiral symmetry restoration. The key is their lifetimes (see the Figure 1.4).

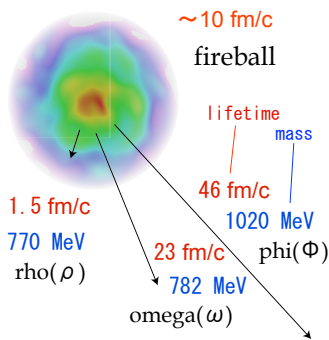


Figure 1.4: Lifetimes

The typical fireball, the hot and dense matter called QGP discussed previously, is said to have ~ 10 fm/c lifetime [9]. While some low-mass vector mesons, ϕ , ω and ρ have lifetimes as 46 fm/c, 23 fm/c and 1.3 fm/c respectively. This means, a lot of vector mesons (most of the ρ mesons) have a chance of decaying inside the medium. They should provide an unique tool to observe in-medium modifications of its properties (e.g. mass and/or width) which could be linked to the Chiral Symmetry Restoration. In this section, we're going to describe how the matter effects vector mesons' properties by a theoretical calculation first and going to report

the current experimental status next.

1.2.1 Medium Modification

The most common approach to evaluate medium effects on vector mesons properties consists of evaluating effective interactions with surrounding hadrons from the heat bath[14][10], leading to in-medium insertions which are resummed in the propagator as (here for the ρ),

$$D_\rho(M, q; \mu_B, T) = [M^2 - (m_p^{(0)})^2 - \Sigma_{\rho\pi\pi} - \Sigma_{\rho B} - \Sigma_{\rho M}]^{-1}, \quad (1.5)$$

where M , $m_p^{(0)}$:mass and bare mass, q :momentum, μ_B :baryon density and T :temperature. The different contributions may be classified as; modifications of the pions in the $\pi\pi$ decay ($\Sigma_{\rho\pi\pi}$), direct ρ -baryon couplings ($\Sigma_{\rho B}$) and direct ρ -meson couplings ($\Sigma_{\rho M}$).

The imaginary part of the propagator ($\text{Im}D_\rho$) coincides with the spectral function up to a factor of (-2). The Figure 1.5 and The Figure 1.6 show its value for rho and omega mesons. They agree in that the main effect is a substantial broadening, accompanied by a small upward mass shift.

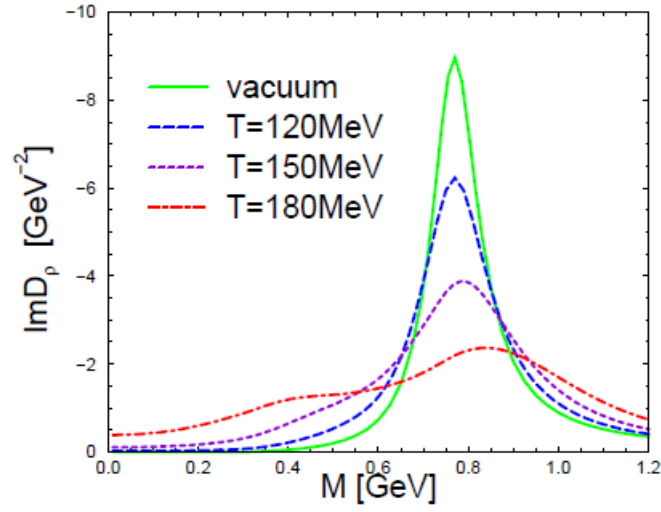


Figure 1.5: ρ meson spectral function, $\text{Im}D_\rho(M, q = 0)$, in hadronic matter under approximate conditions ($\mu_B = 330\text{MeV}$)[11].

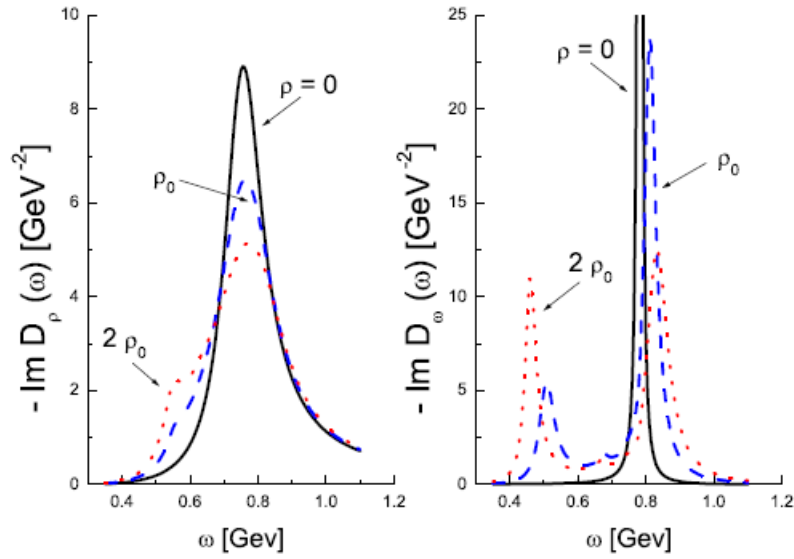


Figure 1.6: ρ meson and ω meson spectral function in nuclear matter at $\rho = \rho_0$ and $\rho = 2\rho_0$, compared to those in the vacuum[12].

How is the degeneracy of chiral partners realized? Do the masses drop to zero? Do the widths increase? The fact is that there is no good answer to any of these questions so far. The one theory which has just shown was done by Ralf.Rap *et al.* It expected that the mean of vector meson's mass would barely shift to upward and width would get broader, however, the other calculations based on different models result in different way. The Figure 1.7 is such one result done by T.Hatsuda and S.H.Lee using QCD sum rules[13]. It shows that the mass shift inversely downward.

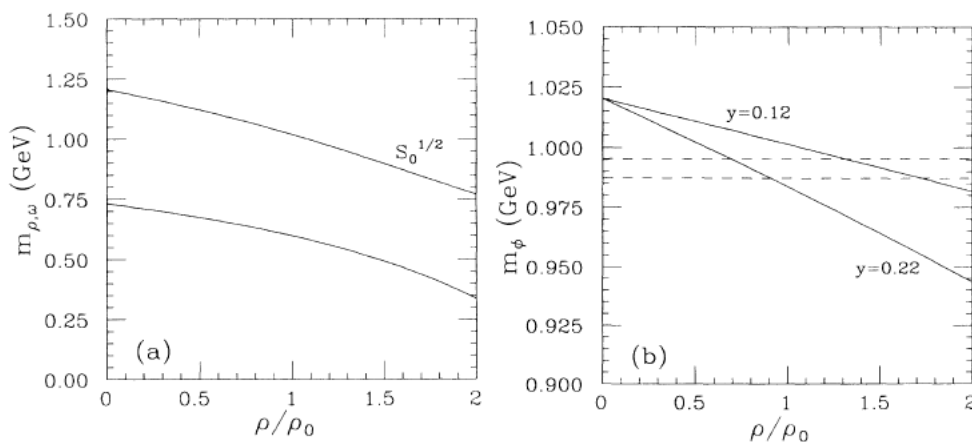


Figure 1.7: (a) The ρ - ω meson mass m and the continuum threshold $S_0^{1/2}$ as a function of ρ/ρ_0 . (b) The same figure for the ϕ -meson mass with two typical values of y (the strangeness content in the nucleon). Dashed lines indicate the K^0K^0 and K^+K^- threshold at $\rho = 0$ which are the main decay modes of ϕ .

Since there's no clear consistent results for the theoretical approach to search for the effect of Chiral Symmetry Restoration, we couldn't estimate how the vector meson's mass exactly change in advance. Therefore, it can be said that this is the example where experiments has the potential to guide the theory. Next, we compare the current experimental results.

1.2.2 Current Status

A lot of experimental challenges for searching the in-medium modifications of vector mesons had been executed and some experiments are still in advance. We are going to introduce following five major experiments producing interesting results. *KEK* (Japan), *Jlab* (U.S.) and *CBELSA/TAPS* (Germany) are the experiments using elementary reactions using fixed targets for creating high density. *CERES* and *NA60* (Both in CERN at Geneva) are the heavy ion experiments for creating high temperature. The merit of the elementary reactions is that those are well controlled conditions since there's no time dependence of baryon density. The demerit is the small medium effects because the reaction temperature is low. On the other hand, the merit of the heavy ion collisions is the sizable effects due to high densities and temperatures. The demerit is that any signal represents an integration over the full space-time history of the heavy-ion collision with strong variations in densities and temperatures[15].

The Figure 1.8 shows a comparison of the five experiments' results for each vector meson. Let us see them one by one.

	KEK	Jlab	CBELSA/TAPS	CERES	NA 60
ω	–	–	mass shift: -14% $\Gamma_{\omega}(\rho=\rho_0)\approx 100\text{MeV}$	–	–
ρ	mass shift: -9% no broadening	no mass shift some broadening	–	broadening favored over density dependent mass shift	no mass shift strong broadening
Φ	mass shift: -4% $\Gamma_{\phi}(\rho_0)=47\text{MeV}$	–	–	–	–

Figure 1.8: Current status of in-medium modifications of vector mesons[15].

KEK

The invariant mass spectra of e^+e^- pairs produced in 12 GeV $p + A$ interactions are measured at the KEK Proton Synchrotron [16][17]. Copper and carbon targets are used to study the nuclear-size dependence of e^+e^- invariant mass distributions (see the Figure 1.9). On the low-mass side of the ω meson peak, a significant enhancement over the known hadronic sources has been observed. Also a significant excess on the low-mass side of the ϕ meson peak is observed in the low $\beta\gamma (= \beta/\sqrt{1-\beta^2})$ region of ϕ mesons ($\beta\gamma < 1.25$) with copper targets.

Jlab

While KEK measured vector mesons, the CEBAF Large Angle Spectrometer (CLAS) detector located in the Jefferson Laboratory (Jlab) collected data in 2002[18]. The experiment had the conditions with an intense photon source, and ^2D , ^{12}C , ^{48}Ti , ^{56}Fe and ^{208}Pb targets. The method is same as KEK, however, it tuned out the results is inconsistent. The results are compatible with no mass shift at all and have a normal width broadening.

CBELSA/TAPS

The photoproduction of ω mesons on nuclei has been investigated using the Crystal Barrel/TAPS experiment at the ELSA tagged photon facility in Bonn[19]. Results obtained for Nb are compared to a reference measurement on a LH_2 target. While for recoiling, long-lived mesons (π^0, η and η'), which decay outside of the nucleus, a difference in the line shape for the two data samples is not observed. They find a significant enhancement towards lower masses for ω mesons produced on the Nb target (see the right plot in the Figure 1.11). For momenta less than 500 MeV/c an in-medium ω meson mass of $M_{\text{medium}} = [772_{-4}^{+4}(\text{stat})_{35}^{+35}(\text{syst})]$ MeV/c² has been deduced at an estimated average nuclear density of $0.6\rho_0$.

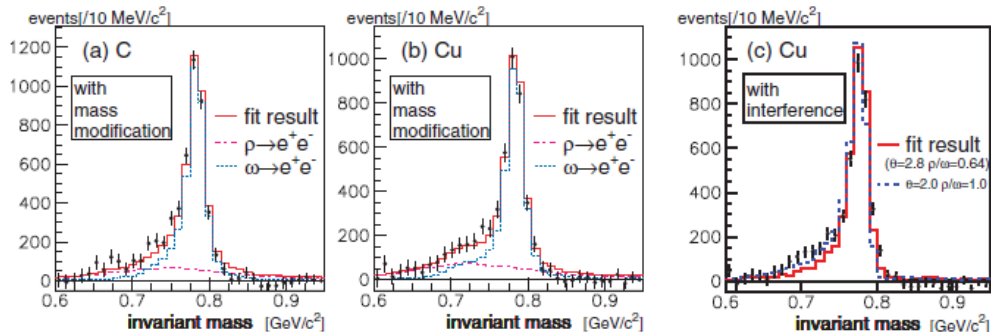


Figure 1.9: Invariant mass spectra of e^+e^- measured in KEK E-325 experiment[16]. The result of the model calculation considering the in-media modification for the (a)C and (b)Cu targets, together with (c) the fit result with the $\rho - \omega$ interference for the Cu target. In (a) and (b), the shapes of $\omega \rightarrow e^+e^-$ (dotted line) and $\rho \rightarrow e^+e^-$ (dash-dotted line) were modified according to the model using the formula $m(\rho)/m(0) = 1 - k(\rho/\rho_0)$ with $k = 0.092$.

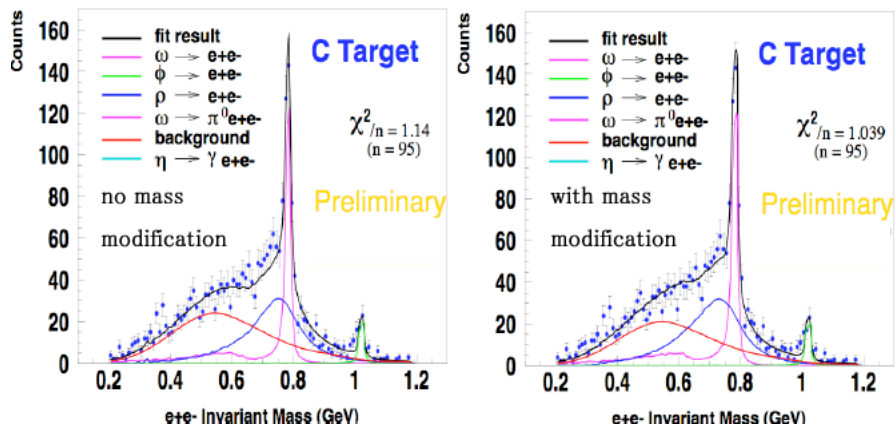


Figure 1.10: Invariant mass spectra of e^+e^- measured in Jlab[18] with a calculation plot of with and without modification. χ^2 fit are used to assess the mass shift.

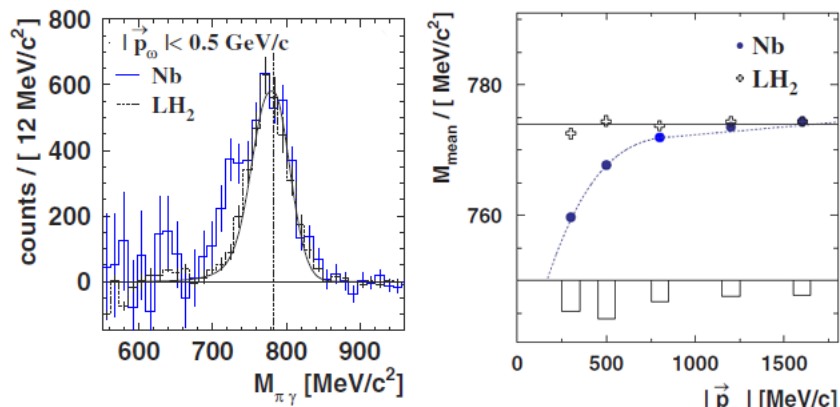


Figure 1.11: Left plot: $\pi^0\gamma$ invariant mass for the Nb data (solid histogram) and LH₂ data (dashed histogram) after background subtraction[19]. Right plot: Mean value of the $\pi^0\gamma$ invariant mass as a function of the ω momentum at an estimated average density of $0.6\rho_0$ for the Nb data (circles) and the LH₂ (crosses) along with a fit.

CERES

The measurement of e^+e^- pair production in central Pb-Au collisions at 158A GeV/c were produced in the CERN-Super-Proton-Synchrotron(SPS) by the CERES experiment[20]. A significant excess of the e^+e^- pair yield over the expectation from hadron decays is observed (the enhancement is pronounced in the mass region $0.2 < m_{ee} < 0.6$ GeV/c² in the Figure 1.12). The data clearly favor a substantial in-medium broadening of the ρ pole mass.

NA60

Low-mass muon pairs in 158A GeV indium-indium collisions were measured at the CERN SPS[21]. A significant excess of pairs is observed above the yield expected from neutral meson decays (see the Figure 1.13). The unprecedented sample size of 360'000 dimuons and the good mass resolution of about 2% could isolate the excess by subtraction of the decay sources. The shape of the resulting mass spectrum is consistent with a dominant contribution from $\pi^+\pi^- \rightarrow \rho \rightarrow \mu^+\mu^-$ annihilation. The associated space-time averaged ρ spectral function shows a strong broadening, but essentially no shift in mass.

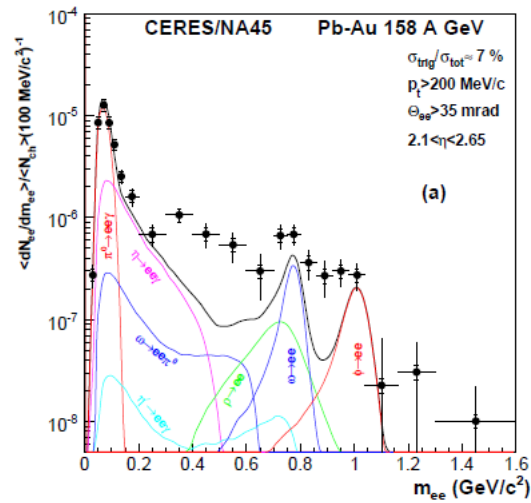


Figure 1.12: Invariant e^+e^- mass spectrum compared to the expectation from hadronic decays at the CERES experiment[20].

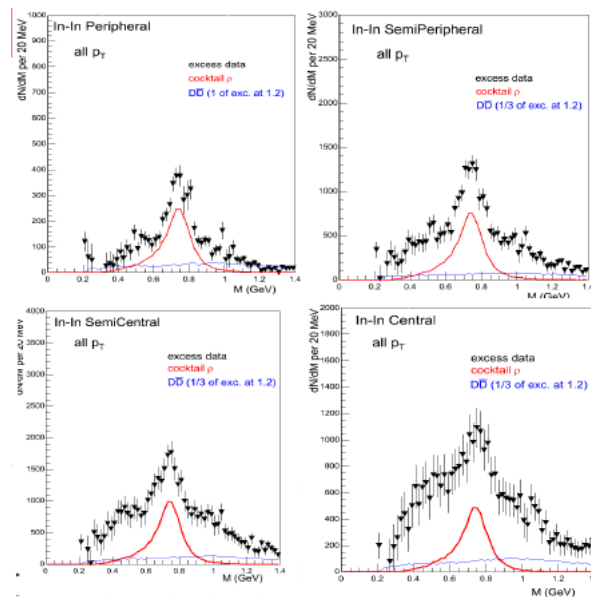


Figure 1.13: Excess mass spectra of dimuons at the NA60 experiment[21]. The cocktail ρ (red lines) and the level of uncorrelated charm decays (dashed lines) are shown for comparison.

Despite of enormous progress in the experiments, there is no fully consistent picture as yet. It is needless to say that further experiments and analysis are in demand. For now on, HADES at GSI in German and RHIC at BNL (Here, we are involved. The detail will be described in the next chapter.) are still working and lots of analysis are good in advance. In the future, the Large Hadron Collider (LHC) at CERN in Geneva is planned for the heavy ion collisions and Compressed Baryonic Matter (CBM) at GSI is planned for the elementary reaction using heavy ion beams. We put those major experiments according to the time scale and the energy scale in the Figure 1.14. Presently, RHIC is positioned at the highest energy experiment and producing intriguing results of vector meson's analysis.

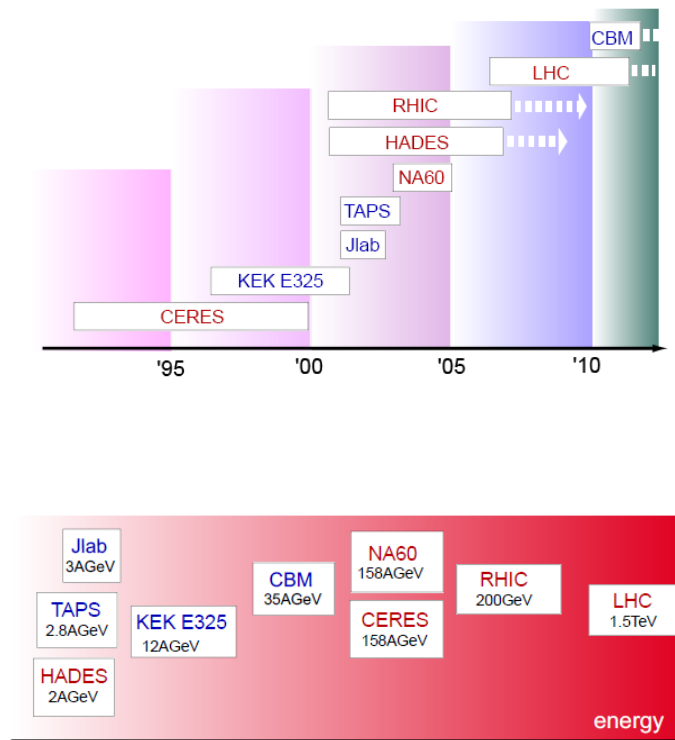


Figure 1.14: Major experiments in the time scale (upper) and the energy scale (lower). Red letter represents the heavy ion collisions and blue letter represents the elementary reactions.

1.3 Motivation

The modification of experimentally observable properties of vector mesons such as mass and width, when embedded in a hot and dense medium, is one of the most fundamental research issues in hadron physics. It could be linked to the Chiral Symmetry Restoration associated with the source of hadron masses. We pick ω mesons since they have relatively short life times, 23 fm/c (a half of ϕ mesons', 46 fm/c) leading to the high possibility of decaying in the medium. The Table 1.1 shows the details of the ω mesons' status.

ω (782) mesons	
Mass	$m = 782.65 \pm 0.12\text{MeV}$
Full width	$\Gamma = 8.49 \pm 0.08\text{MeV}$
Decay modes	$\pi^+\pi^-\pi^0$ (BR: $89.1 \pm 0.7\%$)
	$\pi^0\gamma$ (BR: $8.90 \pm 0.27 - 0.23\%$)
	\vdots
	e^+e^- (BR: $7.18 \pm 0.12 \times 10^{-5}$)
	\vdots

Table 1.1: The status of ω mesons [5]

Lots of theories and simulations[22][23][24] pointed out that a promising approach to investigate in-medium modifications of the ω meson is to study the radiative decay mode, $\omega \rightarrow \pi^0\gamma$. We chose this decay mode being blessed with following essential advantages.

- clean way to investigate the properties (due to its electromagnetic coupling to the nucleons, the reaction probability of the photon is almost the same for all nucleons inside the nucleus)
- large branching ratio (about 3 orders of magnitude larger than e^+e^-)
- no ρ -contribution (since the $\rho \rightarrow \pi^0\gamma$ branching ratio(BR) is only 7×10^{-4} and therefore suppressed by 2 orders of magnitude relative to the ω BR into this channel)

The disadvantage of this decay mode is that there is possible π^0 -rescattering within the nuclear medium, which would distort the deduced ω invariant mass distribution. However, the distorted events are predicted to accumulate at ~ 500 MeV/ c^2 which is far below the nominal ω invariant mass. This leads to a small contributions of only about 3% in the mass range of interest, $0.6\text{GeV}/c^2 < M_{\pi^0\gamma} < 0.8\text{GeV}/c^2$ [22].

The mass modification should persist at RHIC's high energies and that PHENIX (the experiment we involved; explained in the next Chapter) with its excellent mass resolution has an unique opportunity to measure photons and reconstruct particles. In the collisions of d+Au and p+p at the PHENIX, ω mesons could be measured and the cross-section has shown[48]. However, the enough temperature for the phase transition leading to the mass modification would be occurred in the collisions of both heavy ions such as Au+Au. It is challenging to search specific particles in such collisions due to it's high multiplicity, but worth study to do it. That's why we started this analysis.

In this Chapter, we introduced the heavy ion physics, Chiral Symmetry Restoration, theoretical and experimental status of low mass vector mesons. In the Chapter 2, the accelerator facilities and the experimental setup of detectors are discussed. In the Chapter 3, the method for this analysis, simulation studies and data selections are shown. In the Chapter 4, we report our latest results. The plots of invariant mass are shown and we discuss the way to subtract the background. We give the conclusion in the Chapter 5.

Chapter 2

Experimental Setup

The Relativistic Heavy Ion Collider (RHIC) at Brookhaven National Laboratory is a world-class scientific research facility that began operation in 2000, following 10 years of development and construction[25].

2.1 RHIC

The process of accelerating an ion involves several accelerators that make up the RHIC complex. The Figure 2.1 shows the RHIC complex.

The ion beam starts its journey in the Tandem Van de Graaff. It consists of two electrostatic accelerators which is capable of producing voltage up to 15 million volts, sending them on their way towards the Booster. From the Tandem, the bunches of ions enter the Tandem-to-Booster beamline, which carries them through a vacuum via a magnetic field to the Booster. At this point, they're traveling at about 5% the speed of light. Then the ions are provided with more energy at the Booster Accelerator with electromagnetic waves and they reach a speed of 37% that of light. As they whirl around the Alternating Gradient Synchrotron (AGS) and are accelerated as in the Booster, the ions get even more energy – until they are traveling at 99.7% the speed of light. When the ion beam is traveling at top speed in the AGS, it is taken down another beam line called the AGS-To-RHIC (ATR) transfer line. Once they reach the end of the ATR transfer line, the ions are divided into 2 bunches, traveling either clockwise or counterclockwise in the so-called *blue* and *yellow* lines. From here on, the counter-rotating beams are accelerated, as in the Booster and AGS, and then circulate in RHIC.

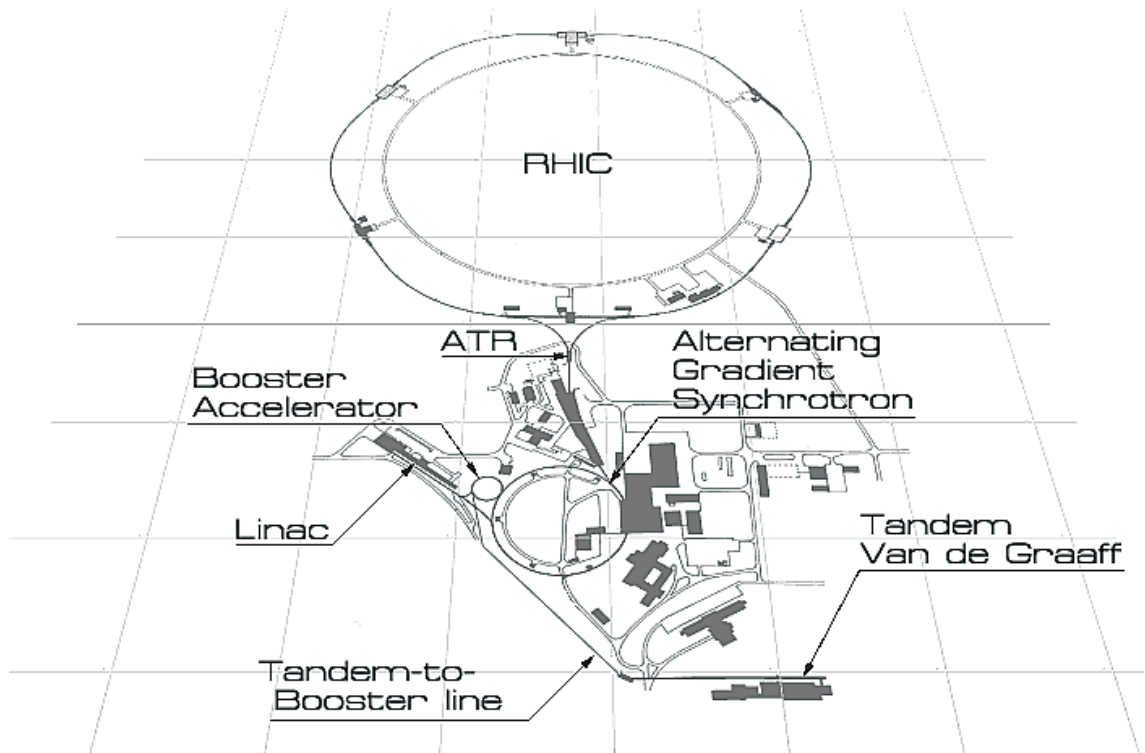


Figure 2.1: The RHIC complex

The RHIC ring has a circumference of 3.8km with the maximum bunch of 120 and the designed luminosity is $2 \times 10^{26} \text{cm}^{-2} \text{s}^{-2}$ for Au ion. The ring has six intersection points where its two rings of accelerating magnets cross, allowing the particle beams to collide. The Figure 2.2 shows its interaction points. If RHIC's ring is thought of a clock face, the four current experiments are at 6 o'clock (STAR), 8 o'clock (PHENIX), 10 o'clock (PHOBOS) and 2 o'clock (BREMS). There are two additional intersection points at 12 and 4 o'clock where future experiments may be placed.

PHENIX, the Pioneering High Energy Nuclear Interaction eXperiment, is the largest of the four experiments where our analysis data is taken. PHENIX is designed specifically to measure direct probes of the collisions such as electrons, muons, and photons by its multi purpose detectors. In the subsequent sections we describe the PHENIX detector and its various detector components.

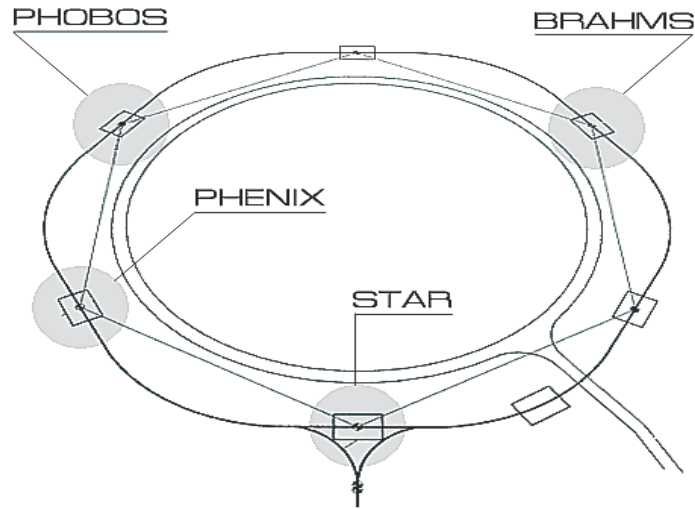


Figure 2.2: RHIC Beam Interaction Points.

2.2 PHENIX Detector

The PHENIX Experiment consists of a collection of detectors, each of which perform a specific role in the measurement of the results of a heavy ion collision. The setup of the PHENIX experiment[26][27] as shown in the Figure 4.12 can be grouped into three categories; *global detectors*[28] closed to the beam pipe and the four spectrometer arm, 2 *muon arms*[29] which has pseudo-rapidity(refer to the Introduction) coverage of $\pm(1.2-2.4)$, and 2 *central arms*[30] which has pseudo-rapidity coverage of ± 0.35 and 180azimuthal angle in total.

Two beams coming from the beam pipe will be made to collide at the center of the detector. Then *global detectors* measure the start time, vertex and multiplicity of the interactions. As shown in the name, *muon arms* focus on the measurement of muon particles. *Central arms* are capable of measuring a variety of particles including pions, protons, kaons, deuterons, electron and photons. *Electro Magnetic Calorimeter*, the one of a detector in the central arm which is the key for measuring photons, is explained in the last of this section separately since this analysis deeply depends on this detector.

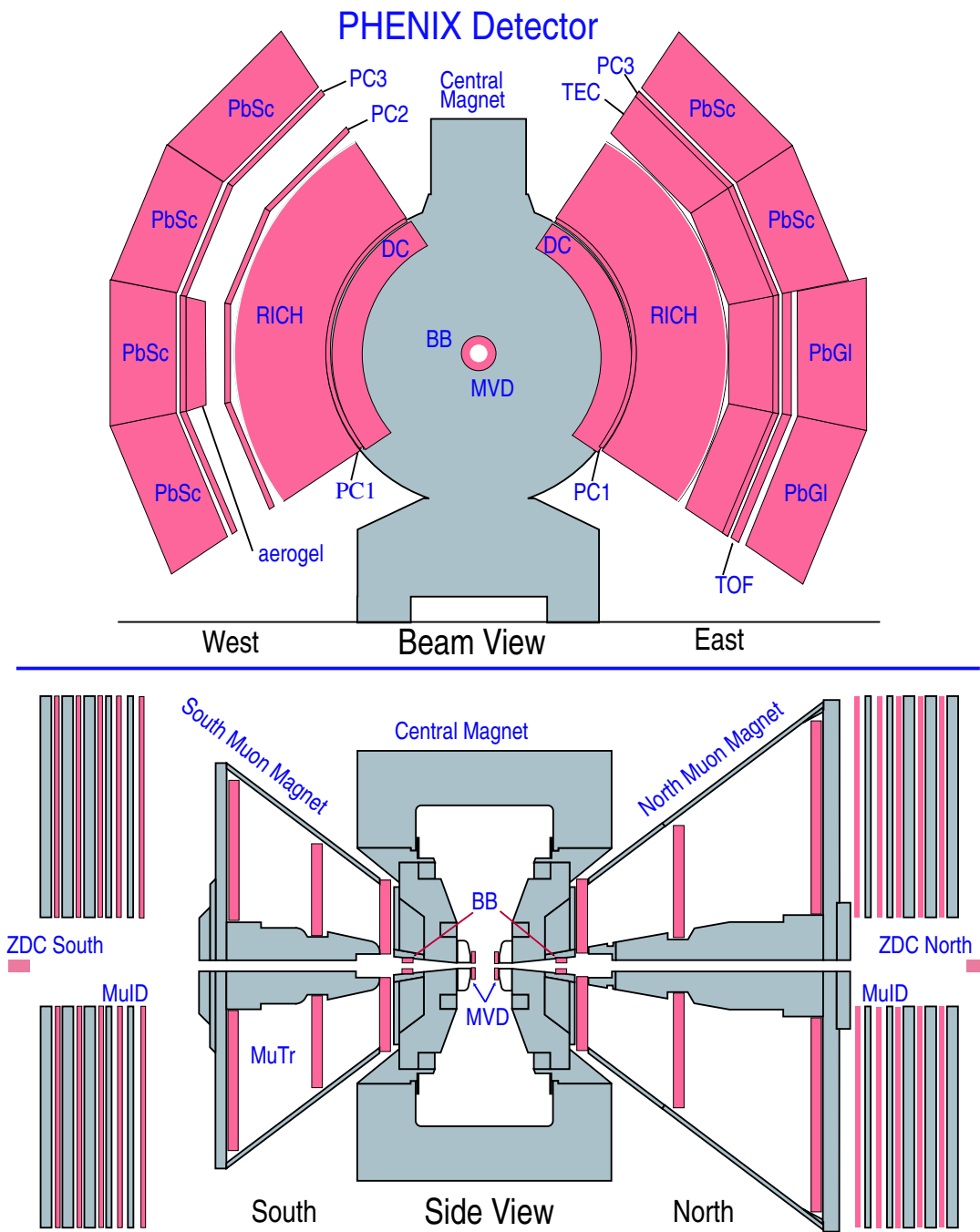


Figure 2.3: The PHENIX Detector configuration (2004)

2.2.1 Global Detectors

In order to characterize the nature of an event following a heavy ion collision, three global detectors[28] were employed. They consist of *Beam Beam Counters* (BBC), *Zero Degree Calorimeters* (ZDC) and *Multiplicity Vertex Detector* (MVD).

Beam Beam Counters (BBC)

Our analysis group contributes to this detector and has a responsibility for it every year. The Beam Beam Counters (BBC)[28][31] have four major tasks, to measure the collision vertex, to produce a signal for the PHENIX trigger and to determine three important variables ;the centrality, the time of beam-beam collisions for the TOF(will be explained later) measurements and the reaction plane. The determination of the centrality and the reaction plane are discussed in the Section 1.3.

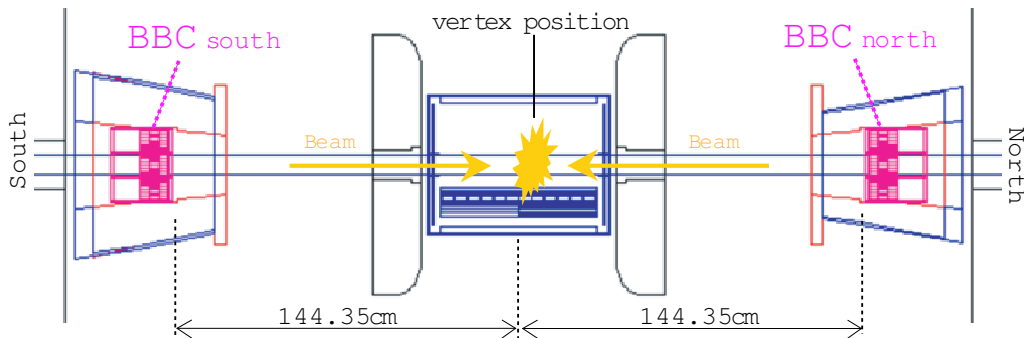


Figure 2.4: The position of BBC. The BBC's are placed 144 cm from the center of the interaction diamond and surround the beam pipe. Assume the arrival times of leading charged particles from beam collisions to each BBC south and north as T_S and T_N . So then the vertex position = $(T_S - T_N)/2 \times c$, the vertex time = $(T_S - T_N - 144.35 \times 2/c)/2$.

The BBC consists of two identical sets of counters installed on both sides of the collision point along the beam axis, one on the North side and the other on the South side of the PHENIX coordinate system. The Figure 2.4 shows the position of BBC and the way to measure the vertex position and the vertex time. The single BBC consisting of one-inch mesh dynode photomultiplier tubes mounted on a 3 cm quartz radiator. And it is comprising 64 BBC elements. The interaction position along the beam axis is calculated from individual time measurements of fast leading particles hitting BBC on the both sides of the interaction point. With an intrinsic timing resolution of 70 ps, BBC determines the interaction position with a precision of 0.6 cm.

Zero Degree Calorimeters (ZDC)

The Zero Degree Calorimeters (ZDC)[32] are hadron calorimeter standard to all four experiments at RHIC. The two ZDCs are located at 18m north and south from the nominal collision point. Since both north and south ZDC sit at just the upstream of the last bending magnet on the RHIC ring, most of the charged particles are swept out from the acceptance. So then the ZDC measures the beam energy neutrons emitted in the breakup of the nuclear remnant that misses the interaction zone. The calorimeters are also the principle device to monitor the beam luminosity during the run and serves as an event trigger for all four RHIC experiments.

Multiplicity Vertex Detector (MVD)

The Multiplicity Vertex Detector (MVD)[28] provides a more precise determination of event position and multiplicity and measures fluctuations of the charged particle distributions. It is composed of concentric barrels of silicon-strip detectors around the beampipe and two disk-shaped endcaps of silicon pad detectors at $z \cong \pm 35$ cm, where z refers to the beam axis. The length of the active part of the silicon strip barrels is approximately 64 cm. The design criteria included large rapidity and good azimuthal coverage and granularity while also minimizing costs and material in the electron arm acceptance.

2.2.2 Muon Arm Detectors

A pair of forward spectrometers were set for the purpose of measuring muons. Each muon spectrometer has a large geometric acceptance of about one steradian and excellent momentum resolution and muon identification.

Muon Tracker

The Muon Tracker (MuTr)[29] consists of three stations of multi-plane drift chambers that provide precision tracking. Each of the three stations of cathode strip chambers presented unique design requirements. All are in the shape of octants built with a 3.175 mm half gap, 5 mm cathode strips and with alternate strips readout. The above design specifications led to the relative mass resolution, approximately given by $\sigma(M)/M = 6\%/\sqrt{M}$, where M is in GeV. This mass resolution enables a clear separation of the ρ/ω peak from the ϕ , J/ψ and ψ' , with an acceptable separation of Υ and Υ' .

Muon Identifier

The Muon Identifier (MuID)[29] consists of alternating layers of steel absorbers and low resolution tracking layers of streamer tubes. There are six such panels per gap arranged around the square hole left for the beam pipe to pass through. The Figure 2.5 shows the panels as installed in the south arm of PHENIX. The MuID design and the algorithms are used to reject the large hadron background from muon. The design goal of a pion rejection rate is about 2.0×10^{-4} and it is consistent with the result from a simulation[29].



Figure 2.5: The south Muon Identifier

2.2.3 Central Arm Detectors

The central arm is equipped with detectors for electron, hadron and photon measurements. The separation of negative and positive tracks are done by applying a magnetic field from *Central Magnet*. The tracking system uses three sets of *Pad Chamber* to provide precise three-dimensional space points needed for pattern recognition. The precise projective tracking of *Drift Chamber* is the basis of the excellent momentum resolution. *Time Expansion Chamber* in the east arm provides additional tracking and particle identification. *Time-of-Flight* and *Ring Imaging Cherenkov* detectors also provide particle identification. *Aerogel Cherenkov Counter* was introduced in 2003 to enhance the particle identification capability. *Electro Magnetic Calorimeter* described in the subsequent section is the outermost subsystem on the central arms and provides measurements of both photons and energetic electrons.

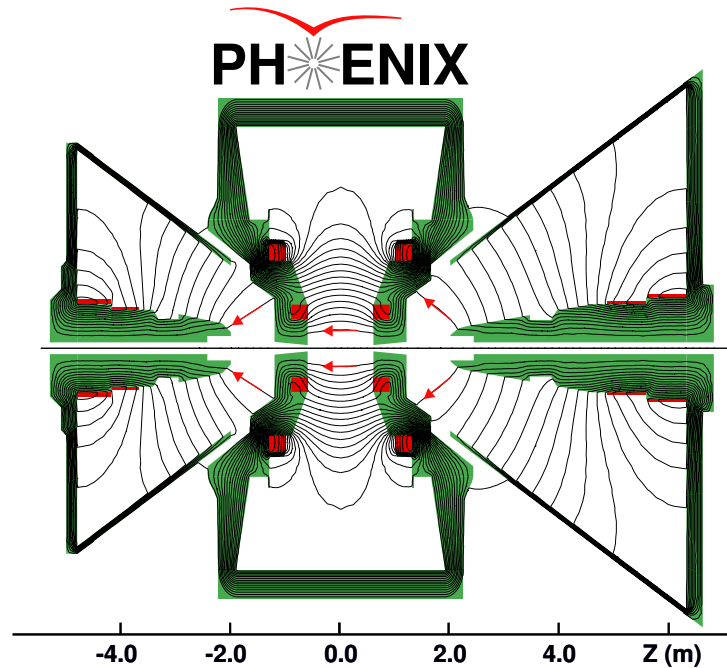
Central Magnet

The Central Magnet[33] is energized by two pairs of concentric coils, which can be run separately, together, or in opposition. The Figure 2.6 shows the field lines when both coils are turned on. It provides a field around the interaction vertex that is parallel to the beam. This allows momentum analysis of charged particles in the polar angle range from 70 to 110.

Pad Chamber

The Pad Chambers(PC)[34] are multiwire proportional chambers that form three separate layers of the PHENIX central tracking system. Each detector contains a single plane of wires inside a gas volume bounded by two cathode planes. One cathode is finely segmented into an array of pixels. The charge induced on a number of pixels when a charged particle starts an avalanche on an anode wire, is read out through specially designed readout electronics. There are three sets of Pad Chambers instrumented in PHENIX, called PC1, PC2 and PC3. The PC1 is located immediately behind the Drift Chambers(DC). The PC2 in the west arm is behind the Ring Imaging Cherenkov(RICH) and the PC3 in both arms are in front of the Electromagnetic Calorimeter(EMCal). The Figure 4.12 shows the location.

The PCs are the only non-projective detectors in the central tracking system and thus are critical elements of the pattern recognition. Its information is also essential for particle identification, particularly for critical



Magnetic field lines for the two Central Magnet coils in combined (++) mode

Figure 2.6: PHENIX Central Magnet Field Lines

electron identification which has to have a hadron rejection factor of 10^4 . The DC and PC1 information gives direction vectors through the RICH, while PC2 and PC3 are needed to resolve ambiguities in the outer detectors where about 30 % of the particle striking the EMCal are produced by either secondary interactions and particle decays outside the aperture of the DC.

Drift Chamber

The Drift Chambers (DC)[34] are cylindrically shaped and located in the region from 2 to 2.4m from the beam axis and 2m along the beam direction shown in the Figure 4.12. Each DC measures charged particle trajectories to determine p_T of each particle and ultimately, the invariant mass of particle pairs. The DC also participates in the pattern recognition at high particle track densities by providing position information that is used to link tracks through the various PHENIX detector sub-systems.

Time Expansion Chamber

The Time Expansion Chamber (TEC)[34] is composed of a set of 24 large multi-wire tracking chambers and it resides in the East arm. The TEC measures all charged particles passing through its active area, providing direction vectors that are matched to additional track information from the DC's and PC's. It also enhances the momentum resolution at $p_T \geq 4$ GeV/c by combining with the DC to provide a long lever arm for improved track-angle resolution.

Time-of-Flight

The Time-of-Flight (ToF)[35] system serves as a primary particle identification device for charged hadrons in PHENIX. It is designed to have about 100 ps timing resolution in order to achieve clear particle separation in the high momentum region, i.e. π /K separation up to 2.4 GeV/c and K/proton separation up to 4.0 GeV/c. The ToF detector is placed at a distance of 5.1 m from the collision vertex, in between the PC3 and the EMCal in the East arm. It consists of 10 panels of ToF walls. One ToF wall consists of 96 segments, each equipped with a plastic scintillator slat and photomultiplier tubes which are read out at both ends.

Ring Imaging Cherenkov

The Ring Imaging Cherenkov (RICH)[35](the photo shown in the Figure 2.7) is one of the primary devices for separation of electrons from the large num-



Figure 2.7: The Ring Imaging Cherenkov detector (before an installation)

bers of the more copiously produced pions, that provides e/π discrimination below the π Cherenkov threshold which is set at about 4 GeV/c. In combination with the EMCal in each arm and the TEC in one arm, the goal is to limit the false identification of hadrons as e^+ and e^- to less than 1 per 10^4 , for momenta below the Cherenkov threshold.

The RICH is located between the inner and outer tracking units. The location can be seen in the Figure 4.12. Each RICH detector has a volume of 40 m^3 and contains 48 composite mirror panels forming two intersecting spherical surfaces, with a total reflecting area of 20 m^2 . The spherical mirrors focus Cherenkov light onto two arrays of 1280 UV photomultiplier tubes.

Aerogel Cerenkov Counter

The Aerogel Cerenkov Counter (AEROGEL) [36] is the additional particle identification installed in 2003 since there were some gaps in the particle identification if it is only done by TOF and RICH. Thanks to that, hadron particle identification can be achieved seamlessly up to $p_T \sim 8\text{ GeV}/c$. Also, the AEROGEL system has excellent trigger capability for high p_T particles.

The detector is located between the PC2 and PC3 in the West arm (shown in the Figure 4.12). It consists of 160 boxes and each box has aerogel with a refractive index of $n = 1.0114$, the best index for a combination with RICH.

2.2.4 Electro Magnetic Calorimeter

The Electro Magnetic Calorimeter (EMCal)[37] is used to measure the spatial position and energy of electrons and photons produced in heavy ion collisions. It covers the full central spectrometer acceptance of $70 \leq \theta \leq 110$ with two walls, each subtending 90° in azimuth. One wall comprises four sectors of a *Lead Scintillator Calorimeter* (PbSc) and the other has two sectors of a *Lead Glass Calorimeter* (PbGl). The Figure 4.12 shows the location. Both detectors have very good energy, spatial and timing resolution, while the PbSc excels in timing and the PbGl in energy measurements. We will describe them separately since their design and the properties are quite different. After that, the *Cluster Algorithm* which is the key for the particle identification will be explained.

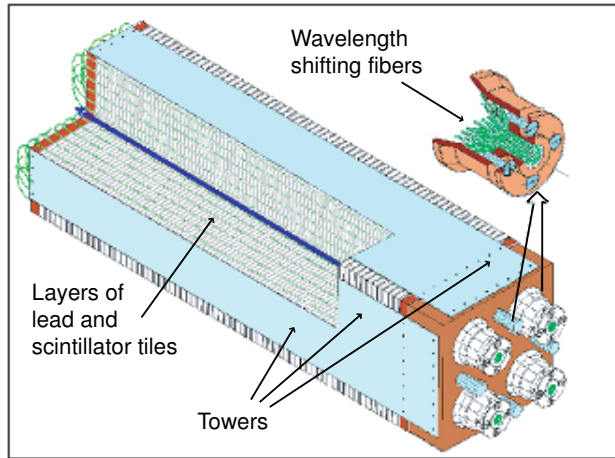


Figure 2.8: Interior view of PbSc module

Lead Scintillator Calorimeter (PbSc)

The Lead Scintillator Calorimeter (PbSc) is a shashlik type sampling calorimeter made of alternating tiles of Pb and scintillator consisting of 15552 individual towers and covering an area of approximately 48 m^2 . The basic building block is a module consisting of four (optically isolated) towers which are read out individually. Four towers are mechanically grouped together into a single structural entity called a "module" as shown in the Figure 2.8. 36 modules are attached to a backbone and held together by welded stainless steel skins on the outside to form a rigid structure called a "supermodule". 18 supermodules make a "sector", a $2 \times 4 \text{ m}^2$ plane with its own rigid steel frame.

The PbSc has a nominal energy resolution as,

$$\sigma_E/E = 2.1\% \oplus \frac{8.1\%}{\sqrt{E(\text{GeV})}},$$

where \oplus denotes a root of the quadratic sum, $\alpha \oplus \beta = \sqrt{\alpha^2 + \beta^2}$, and a position resolution as[38],

$$\sigma_x(E) = 1.4(\text{mm}) + \frac{5.9(\text{mm})}{\sqrt{E(\text{GeV})}}.$$

Intrinsic timing resolution is better than 200 ps for electromagnetic showers.

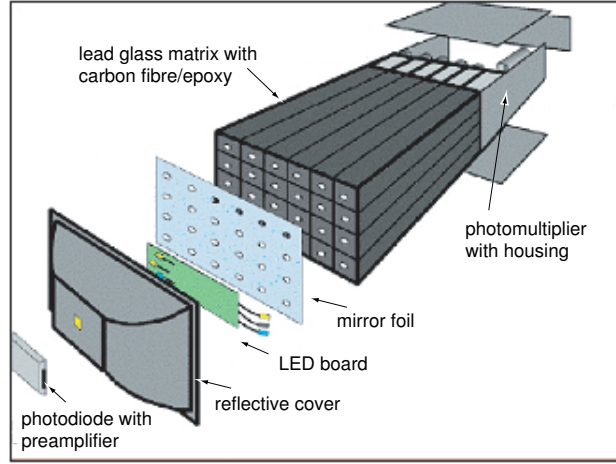


Figure 2.9: Exploded view of a PbGl supermodule(SM)

Lead Glass Calorimeter (PbGl)

The Lead Glass Calorimeter (PbGl) is a Cherenkov type calorimeter, which occupies the two lower sectors of the East arm. Each PbGl sector comprises 192 supermodules(SM) in an array of 16 Lead Glass SM wide by 12 SM high as shown in the Figure 2.9. Each PbGl SM comprises 24 PbGl modules in an array of 6 PbGl modules wide by 4 modules high. Modules within the SM are individually wrapped with aluminized mylar foil and shrink tube and isolated optically. Steel sheets of 0.5mm thickness are used to house the entire towers and phototubes.

The PbGl has a nominal energy resolution as,

$$\sigma_E/E = [0.8 \pm 0.1]\% \oplus \frac{[5.9 \pm 0.1]\%}{\sqrt{E(\text{GeV})}}.$$

The measured position resolution is,

$$\sigma_x(E) = [0.2 \pm 0.1](\text{mm}) \oplus \frac{[8.4 \pm 0.3](\text{mm})}{\sqrt{E(\text{GeV})}}.$$

Intrinsic timing resolution is better than 300 ps for electromagnetic showers above the minimum ionizing peak energy.

Cluster Algorithm

Since electromagnetic and hadronic particles produce quite different patterns of energy sharing between calorimeter towers, second moments of the measured showers are often used to differentiate between them. The first step in the calibration for the EMCal data is the conversion of the raw module information into energy and timing information, referred to as "calibrated towers". Because an electromagnetic shower usually spreads over more than one module, this calibrated towers are passed the *Cluster Algorithm*, which summarizes associated areas of towers into the so-called "clusters". The *Cluster Algorithm* can be divided into the following steps[39]:

- Find a cluster, which is a group of adjacent towers each with an energy above the noise threshold (see the Table 2.1).
- Find the local maxima of the cluster. A local maximum is a module above the peak threshold, given in the Table 2.1, with the maximum amplitude in the 3×3 region surrounding it.
- If more than one local maximum is found, split the cluster according to amplitude and positions of the maxima.
- Calculate the first and second moments of the clusters as the seed for the determination of the impact position.
- Compare the shape of the cluster with the expectation for an electromagnetic shower for particle identification (χ^2 method described next).
- Compute and correct the total energy for the cluster.

For each cluster the newly computed values such as corrected energy and position are stored in a list of clusters that can be used in the analysis.

	PbSc	PbGl
Minimum tower energy	10MeV	14MeV
Minimum cluster energy	15MeV	60MeV
Minimum peak energy	80MeV	80MeV

Table 2.1: The parameters of energy used by the Cluster Algorithm[39]

The one of the corrected energy, " E_{core} " are used for the photon analysis. Assume that there is a cluster from photon; it hit one tower, E5 and spread out 3×3 towers from E1 to E9 but mainly deposited energy at E2, E4, E5, E6 and E8 shown as the Figure 2.2.4.

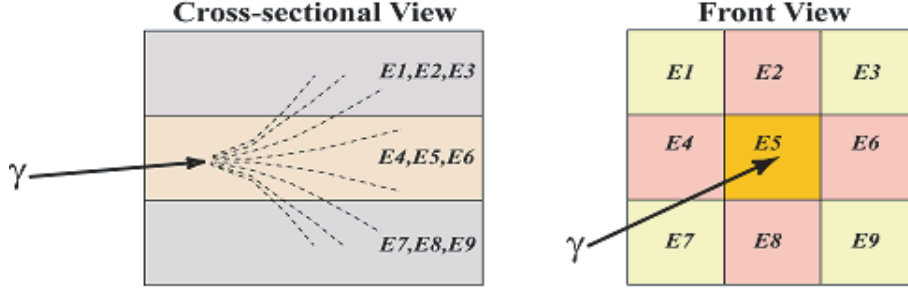


Figure 2.10: Image of a Cluster

The E_{core} energy is defined as[38],

$$E_{core} = \sum_i^{core} E_i^{meas},$$

where E_i^{meas} is the measured energy in i-th tower. \sum_i^{core} is defined as summing of the towers belonging to the "core" towers. The "core" towers are defined in the following condition:

$$\frac{E_i^{pred}}{E_{all}^{meas}} > 0.02, \quad E_{all}^{meas} = \sum_i^{all} E_i^{meas},$$

where E_{all}^{meas} is the sum of measured energy in all towers belonging to the "peak area" cluster E_i^{pred} is the predicted energy (using the parametrization and the actual measured impact point) for an electromagnetic particle of E_{all}^{meas} .

In above case, $E1+E2+\dots+E9$ corresponds to E_{all}^{meas} and if mainly deposited energy passed the "core" condition, E_{core} would be $E2 + E4 + E5 + E6 + E8$. So then E_{core} can chose the energy from highly identified as photon.

Not only for photons but also electrons to be identified, χ^2 method was introduced. that is,

$$\chi^2 = \sum_i \frac{(E_i^{pred} - E_i^{meas})^2}{\sigma_i^2}$$

where E_i^{meas} and E_i^{pred} are same value defined previously. The variance σ_i is given as,

$$\sigma_i^2 = q(E) + C \cdot E_i^{pred} \cdot \left(1 + a_1 \cdot \frac{E_i^{pred}}{E} + a_2 \cdot \left(\frac{E_i}{E} \right)^2 + f(E, \theta) \cdot \left(1 - \frac{E_i^{pred}}{E} \right) \right),$$

which provides the dependence of the fluctuations on the energy and angle of incidence, $f(E, \theta)$, and on losses to the total energy due to the thresholds used in the clustering, $q(E)$. This χ^2 value characterizes how "electromagnetic" a particular shower is and can be used to discriminate against hadrons. The important new feature of this model is that the fluctuations are also parameterized. Therefore, the resulting χ^2 distribution is close to the theoretical one and it is nearly independent of the energy or the impact angle of the electron. The χ^2 distributions for 2 GeV/c electrons and pions (with energy deposit above minimum ionization) are shown in the Figure 2.2.4. The arrow marks the χ^2 cut corresponding to 90 % electron efficiency[37].

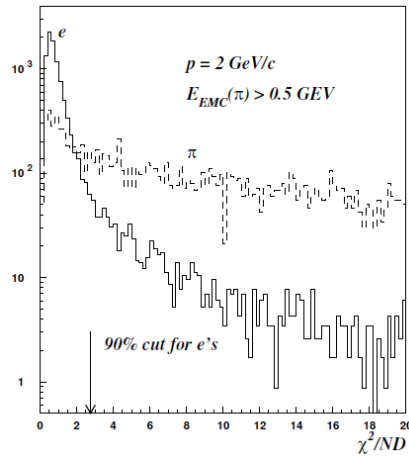


Figure 2.11: χ^2 distribution for showers induced by 2 GeV/c electrons and pions in the PbSc calorimeter [37]

2.3 Computing

One cannot collect all data at every crossing since there's too many empty crossings at the RHIC; collisions occur at about 10kHz for Au-Au, while the beam crossing rate occurs at 9.6MHz. These data need to be selected and archived in order to optimize the physics interest of PHENIX. In this section, we're going to overview the system of the PHENIX On-Line System[40] which was designed to seamlessly accommodate improvements in the design luminosity. Furthermore, the PHENIX's general Off-Line analysis system will be roughly described subsequently.

The On-Line system has two levels of triggering, denoted as Level-1 (LVL1) and Level-2 (LVL2). The LVL1 trigger operates in a synchronous pipelined mode, generates a decision every 106 ns and has an adjustable latency of some 40 beam crossings. It consists of two separate subsystems, the Local Level-1 (LL1) system which communicates directly with participating detector system such as BBC, MuID, ZDC, EMCal and RICH and the Global Level-1 (GL1) which receives and combines these data to provide a trigger decision. The LVL1 trigger and lower levels of the readout are clock-driven by bunch-crossing signals from the RHIC clock. The higher levels of readout and the LVL2 trigger are data-driven where the results of triggering and data processing propagate to the next higher level only after processing of a given event is completed.

The data collection and storage can be described in the Figure 2.3. Signals from the various PHENIX subsystems (e.g.the DC in the Figure 2.3) are processed by Front End Electronics which are fed into Front End Modules (FEM) for each subsystems, that convert detector signals into digital event fragments. This involves analog signal processing with amplification and shaping to extract the optimum time and/or amplitude information, development of trigger input data and buffering to allow time for data processing by the LVL1 trigger and digitization. This is carried out for all detector elements at every beam crossing synchronously with the RHIC beam clock. The timing signal is a harmonic of the RHIC beam clock and is distributed to the FEM's by the PHENIX Master Timing System which are fed into the Master Timing Modules (MTM). The LVL1 trigger provides a fast filter for discarding empty beam crossings and uninteresting events before the data is fully digitized. If the LVL1 trigger accepts an event, a signal is transmitted to the Granule Timing Module (GTM) which generates an accept signal that is transmitted to the detector FEM's in the Interaction Region (IR).

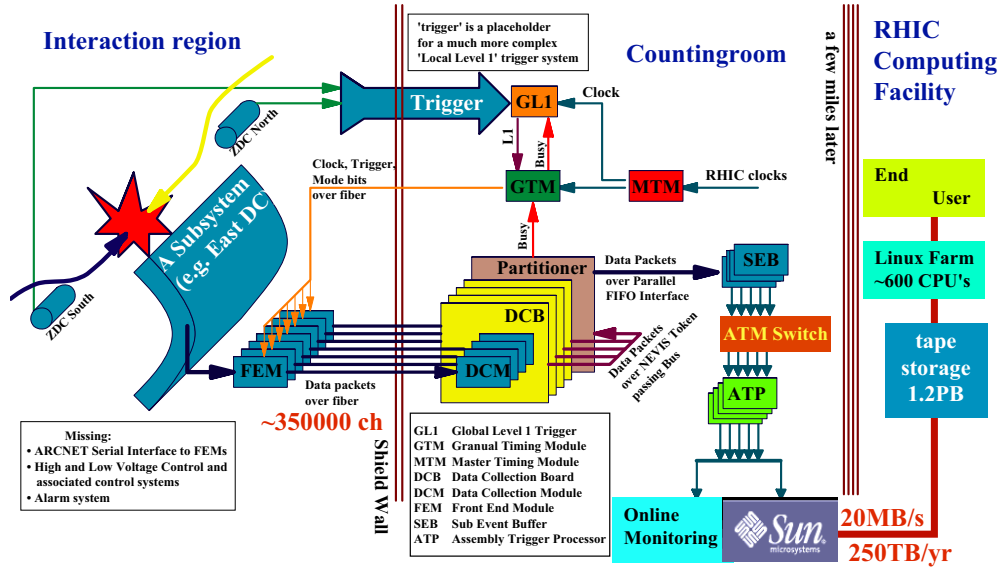


Figure 2.12: Schematic diagram of the PHENIX On-Line system

Once an event is accepted, the data fragments from the FEM's and primitives from the LVL1 trigger move in parallel to the Data Collection Modules (DCM). The PHENIX architecture was designed so that all detector-specific electronics end with the FEM's, so that there is a single set of DCM's that communicate with the rest of the DAQ system. The only connection between the Interaction Region (IR) where the FEM's are located and the Counting House (CH) where the DCM's are located is by fiber-optic cable. The DCM's perform zero suppression, error checking and data reformatting. Many parallel data streams from the DCM's are sent to the Event Builder (EvB). The EvB assembles a full event from the individual fragments of data from the DCM's. When the event is fully assembled and passed the LVL2 trigger, it is temporarily stored on a local disk. A fraction of the events are made available to processes on a farm of computer's running Linux for On-Line monitoring purposes. Long-term storage is provided by a High Performance Storage System (HPSS) type robot system operated by the RHIC Computing Facility (RCF). The average rate of transfer of data to HPSS is 20 Mbytes/s but for short time intervals rates as high as 60 Mbytes/s have been obtained.

All raws data coming from detectors have been assembled in the PHENIX Raw Data Format(PRDF). They are kept to less than 2 Gbytes in size, contain nearly 12 hours to reconstruct. Collections of events over a certain period of time represent the individual "runs". Runs are subdivided into segments to keep the size of the output files low, and to make parallel processing during the offline Data Summary Table (DST) production possible, where the raw data are converted into quantities with more physical meaning.

PHENIX reconstruction, analysis and simulation code consists of about 500,000 lines of codes written in the C++ language. All reconstructed data is kept in HPSS, however, copying groups of files from HPSS, running analysis code over them before deletion and subsequent copy of the next group is cumbersome process at best. More importantly, it is not simultaneously realizable by large groups of users on an individual basis. To solve this dilemma, an *Analysis Train* that registers individual users code and scans through a given dataset in an orderly and optimized fashion was introduced and has been operating from the data taken in 2003-2004. The *Analysis Train* uses the server called *Fun4AllServer*[41] which can keep multiple node trees and chose the data that all calibrations are final. ROOT, an object-oriented analysis framework developed at CERN is used for an output file to fill and visualize histograms. We got in the *Analysis Train* and could collect all statistical of the data without calibrations.

Chapter 3

Analysis

3.1 Quest for ω mesons

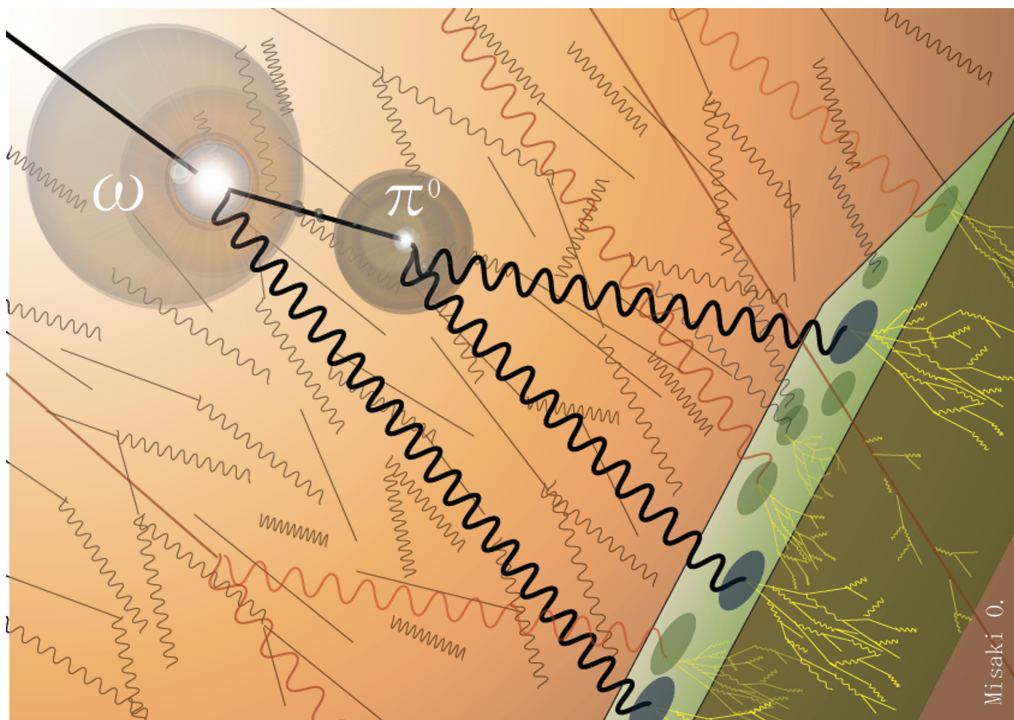


Figure 3.1: Image of the radiative decay mode of ω hitting to the EMCAL

The measurement of ω mesons in the heavy ion collisions is really the "Quest". About 9% of ω s are going to π^0 and γ , then 98.8% of those π^0 is going to 2γ . That is, we have to reconstruct 3γ from huge number of γ measured in EMCal ; approximately 300 γ are measured per one collisions.

The formula of the reconstructed ω mass is simple. After identifying γ , the energy, momentum and hit positions of γ can be measured. The invariant mass of π^0 is therefore,

$$M_{\pi^0}^2 = 2E_1E_2(1 - \cos\theta_{\gamma\gamma}), \quad (3.1)$$

where E_1 and E_2 are the measured energy of 2γ (suppose γ_1 and γ_2 arbitrarily) and $\theta_{\gamma\gamma}$ is the opening angle between 2γ calculated from the hit positions. First we reconstruct π^0 and select γ_1 and γ_2 as " π^0 from ω " candidate. Next we combine third γ (suppose γ_3) and reconstruct as,

$$M_{\pi^0\gamma}^2 = (E_1 + E_2 + E_3)^2 - p_x^2 - p_y^2 - p_z^2, \quad (3.2)$$

where,

$$\begin{aligned} p_x &= E_1 \cdot \frac{x_1}{\sqrt{x_1^2 + y_1^2 + z_1^2}} + E_2 \cdot \frac{x_2}{\sqrt{x_2^2 + y_2^2 + z_2^2}} + E_3 \cdot \frac{x_3}{\sqrt{x_3^2 + y_3^2 + z_3^2}}, \\ p_y &= E_1 \cdot \frac{y_1}{\sqrt{x_1^2 + y_1^2 + z_1^2}} + E_2 \cdot \frac{y_2}{\sqrt{x_2^2 + y_2^2 + z_2^2}} + E_3 \cdot \frac{y_3}{\sqrt{x_3^2 + y_3^2 + z_3^2}}, \\ p_z &= E_1 \cdot \frac{z_1}{\sqrt{x_1^2 + y_1^2 + z_1^2}} + E_2 \cdot \frac{z_2}{\sqrt{x_2^2 + y_2^2 + z_2^2}} + E_3 \cdot \frac{z_3}{\sqrt{x_3^2 + y_3^2 + z_3^2}}, \end{aligned}$$

(the coordinates of x, y and z are defined in the *Appendix*).

The question is, "does it really possible to search out ω mesons in the high multiple collisions that produce huge combinatorial background?" To find the feasibility, we execute the simulation in advance then calculate an acceptance and a multiplicity dependence. Furthermore, we search the best parameters such as momentum and energy for selecting π^0 and γ using both simulation and real data. In the last section of this chapter, we describe the selection values for the real data analysis.

3.2 Data Set

The data-set is Au+Au collisions at C.M.S. collision energy per nucleon pairs of 200GeV taken at the PHENIX from the year of 2003 to 2004; this period is called, "Run4". The Figure 3.2 shows the integrated luminosity delivered by RHIC during Run4, as well as other Runs. Run4 has consistently higher bunch intensities (up to 10^9 for Au+Au) delivered by injectors than other previous runs. The integrated luminosity is up to $1368 \mu b^{-1}$ for PHENIX. The number of events we used from the data is $N_{evt} = 1.06 \times 10^9$ (full statistics).

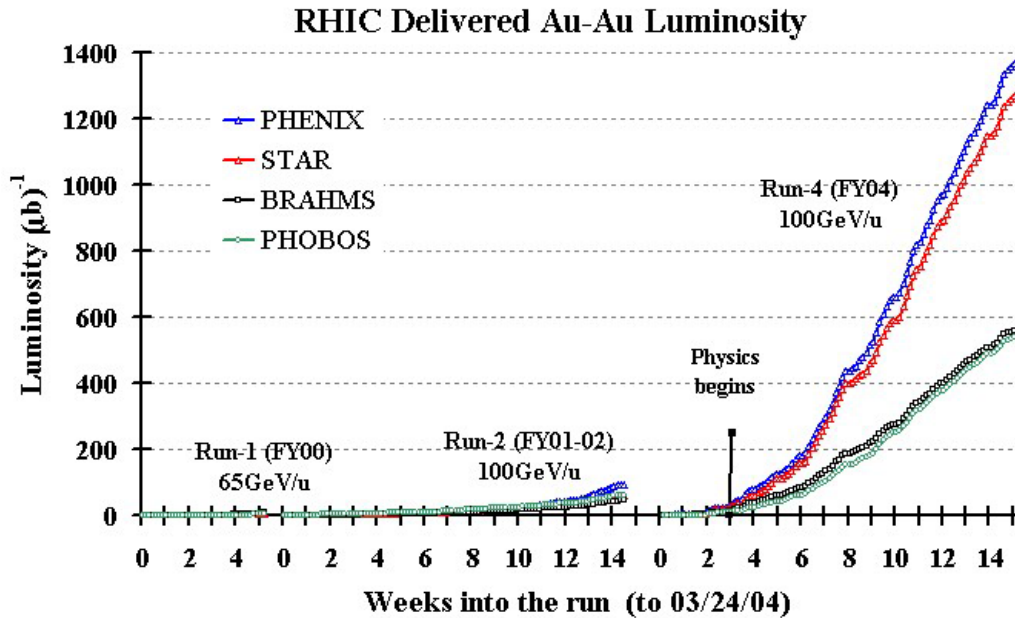


Figure 3.2: The Integrated Luminosity vs Weeks into the Run

3.3 Simulation

3.3.1 Event Generator

The two ion beams accelerated by RHIC will collide and interact. A single interaction is called an "event". An event is fully specified by the position coordinate of the interaction point called the "vertex", or more specifically the "primary vertex". For purposes of the simulation program, an event is viewed as a list of the particles with their type, energies, momenta, the point of production and the time of production which can be conveniently chosen to be the zero of the time. Naturally, the characteristics of the real events will be known only after the actual experiments begin taking data. Until then we must rely on various event generators which attempt to simulate the experimental events by making certain model assumptions. These event generators are detailed Monte Carlo codes. We used the one of such event generators called as "EXODUS", the package of which was created in 1998.

We generated 1.5 M events, one ω meson per event for following status,

- $1.0 < p_T < 14.0$ [GeV/c], enhanced at low pT (the Figure 3.3 shows the pT histogram)
- $-0.5 < y < 0.5$
- $0.0 < \phi < 2\pi$ (refer the Appendix A *Kinematics* for each parameter).

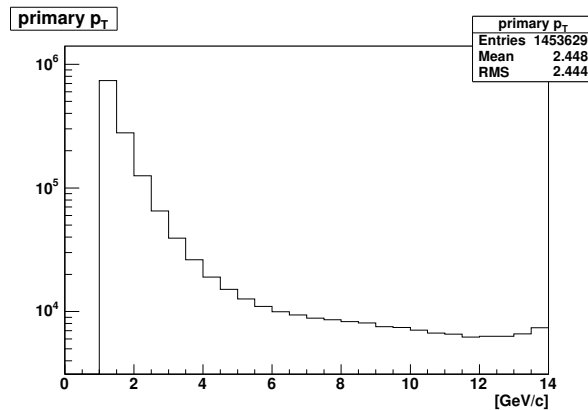


Figure 3.3: The histogram of primary p_T

3.3.2 Detector Simulation

The PHENIX detector is very complex in character with a large variety of detector types and materials inside it. To simulate such PHENIX detector, "PISA", PHENIX Integrates Simulation Application[44] was introduced. The PISA code is based heavily on the CERN software libraries[45]. Specifically, PISA is the PHENIX implementation of the GEANT geometry and event particle tracking software system. Using PISA, a PHENIX simulator can pick which (or all) aspects of the whole PHENIX detector geometry to introduce into an event simulation.

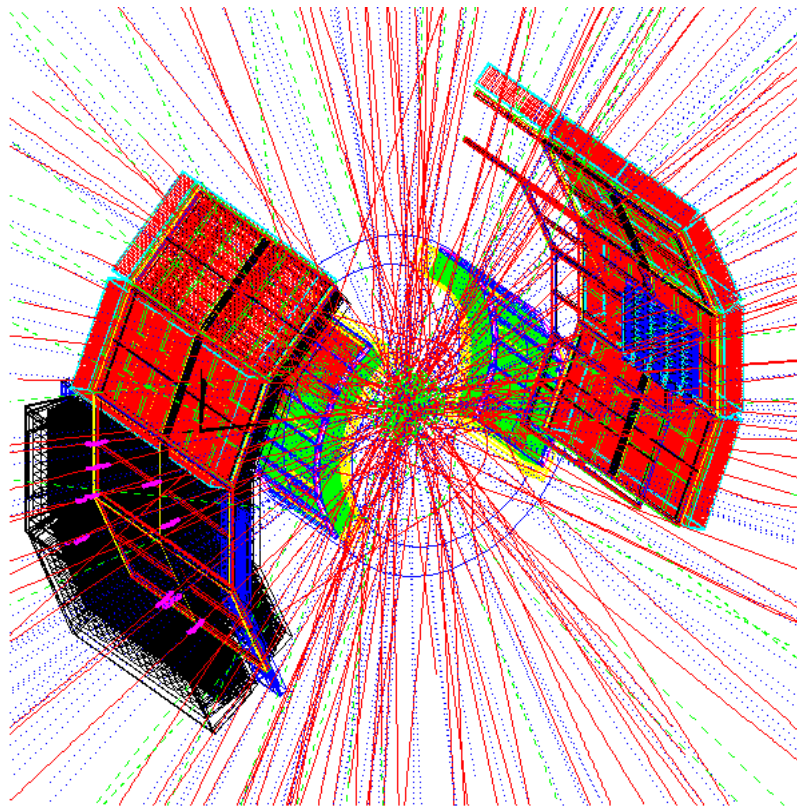


Figure 3.4: Demonstration of simulated 100 ω mesons' tracks (red lines denote electron and positron, blue dotted lines denote photons and green dotted lines denote muons). EMCal, PC1/PC2/PC3, and DC are drawn (see the Chapter 2, *Experimental setup*).

If we input the information of particles that generated by the event generator, PISA will make them decay according to their branching ratio and lifetimes. The Figure 3.4 shows a demonstration of 100 ω going to various decay modes and hitting to (or straying from) the EMCal. We reconstruct ω mesons by calculating the Formula 3.2 after inputting about 7.5 million ω into PISA. The Figure 3.5 is an example plot of reconstructed invariant mass of ω . There is a slight tail at lower region than ω mass (782 MeV/c²) since some photons convert to electrons due to detectors located in front of EMCal and deposit lower energies.

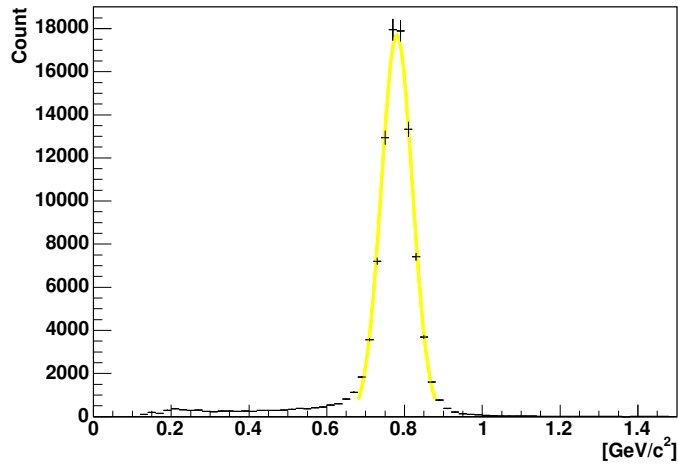


Figure 3.5: Invariant mass spectrum of single ω event for all p_T .

The geometrical acceptance can be measured from this simulation by looking at,

$$\epsilon_{geo} = \frac{dN_{\omega}/dp_T|_{reconstructed}}{dN_{\omega}/dp_T|_{input}}, \quad (3.3)$$

where $dN_{\omega}/dp_T|_{reconstructed}$ and $dN_{\omega}/dp_T|_{input}$ denote the number of reconstructed ω mesons and input ω mesons for each p_T within the 2 sigmas of ω mass, respectively. The calculated acceptance is shown in the Figure 3.12 together with efficiencies of Multiple Dependence Correction (explained in the next section).

3.3.3 Multiplicity Dependence

In the previous section, we calculate the acceptance using single event simulation, that is the so-called "single function (SPC)" which represents correction due to geometrical acceptance, decay in flight, reconstruction efficiency and momentum resolution etc. In addition to this correction function, we have to take it into account the multiplicity dependence as long as dealing with multiple collisions such as Au+Au collisions for this analysis. This is the so called "multiplicity dependence correction function (MDC)". Since the material for this analysis is γ , we discuss only the EMCal's MDC. Multiple collisions generate huge backgrounds to the EMCal and no wonder those backgrounds interfere cluster algorithm. We consider two effects, the one is "cluster merging" and the other is "cluster splitting". As shown those images in the Figure 3.6, backgrounds attached to the true clusters coming from ω cause to merge a cluster or split a cluster.

To evaluate such MDC, we use the technique called "embedding" [46]; embedding of the simulated particles into a real event. The Figure 3.7 shows the main flow of the embedding program [39]. A DST (See the Chapter 2 *Computing*) containing real event is read in together with simulated DST that generated in previous. For each selected real event, the tower information is extracted from the DST and merged with the tower data from on simulated event. The merging basically involves the addition of the energies as illustrated in the Figure 3.7. The list of merged towers is now the basis for a new clustering. Due to the added information from the simulated event, the resulting list of merged clusters is different from the list of clusters from the real event. A comparison yields the modified or new clusters in the merged event and the lost clusters from the real event.

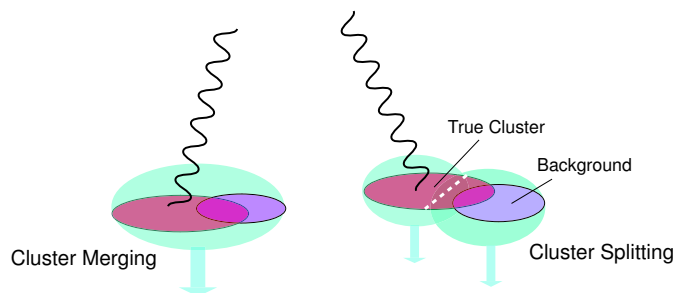


Figure 3.6: The effect of multiplicity on Cluster Algorithm

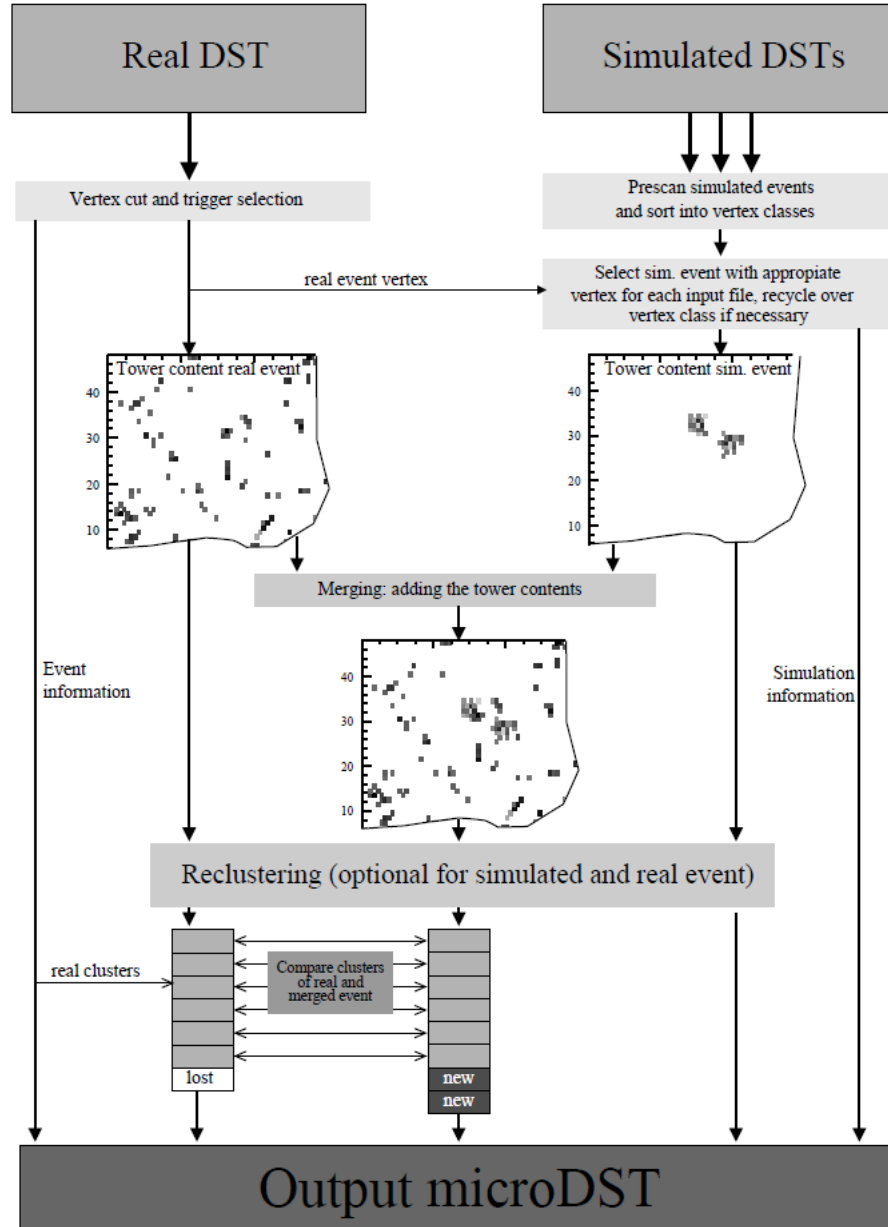


Figure 3.7: Embedding algorithm [39]

We input about 1 million single ω to 1.2 million events of real data, and reconstruct the invariant mass using the Formula 3.2 (the Figure 3.8 is an example). It can be seen that ω mesons merging to the backgrounds.

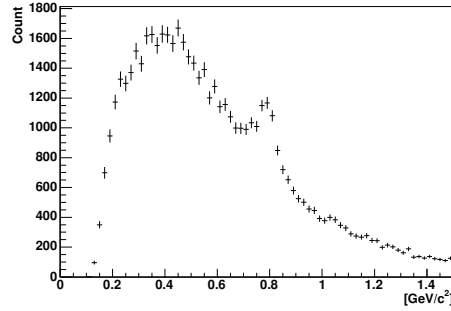


Figure 3.8: Invariant mass spectrum of simulated ω embedding to the real data

To extract the clear peak position and width of ω mass from the results, we choose only true clusters that are from the simulated DST and subtract the background (note that it is possible because we know the input data of simulation). After fitting the gaussian, we get the parameters of ω mass (see the Figure 3.9). The results are shown in the Figure 3.10 and the Figure 3.11. Here, "0-20% cent", "60-92% cent" and "MinBias" mean the high multiplicity, low multiplicity and no selection of multiplicity respectively (the details are explained in the Section of *Data and Signal Selection*).

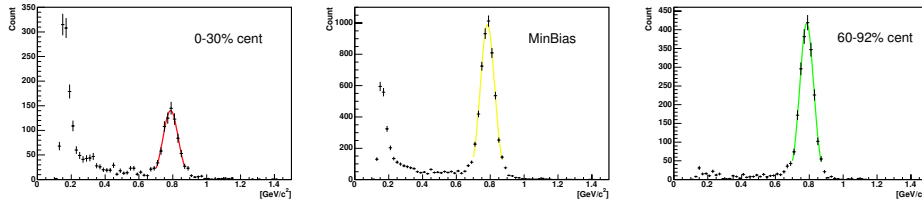


Figure 3.9: Invariant mass spectrum reconstructed by the true clusters. A peak around $0.1-0.2(\text{GeV}/c^2)$ is due to the cluster splitting causing the measured energy lower than true energy (the more we go to the high multiplicity, the more peaks arise).

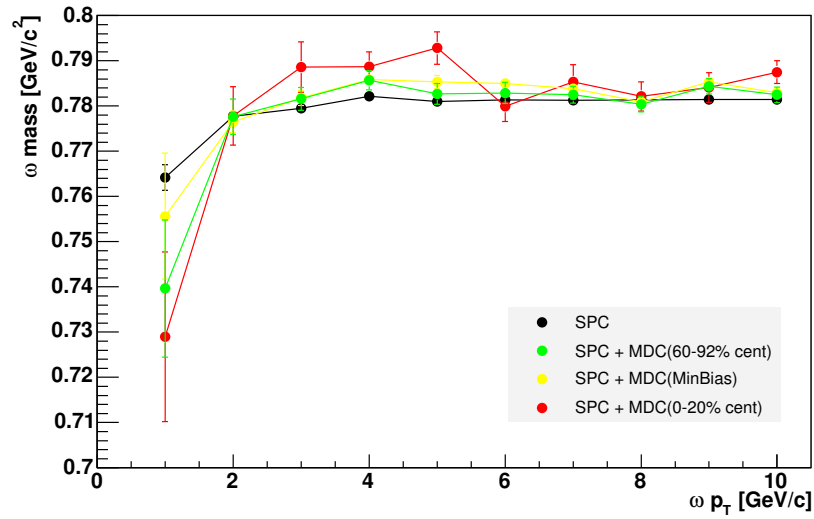


Figure 3.10: Peak position of ω mass. Black points are from the single ω simulation (considering only SPC) and the others are from the embedding.

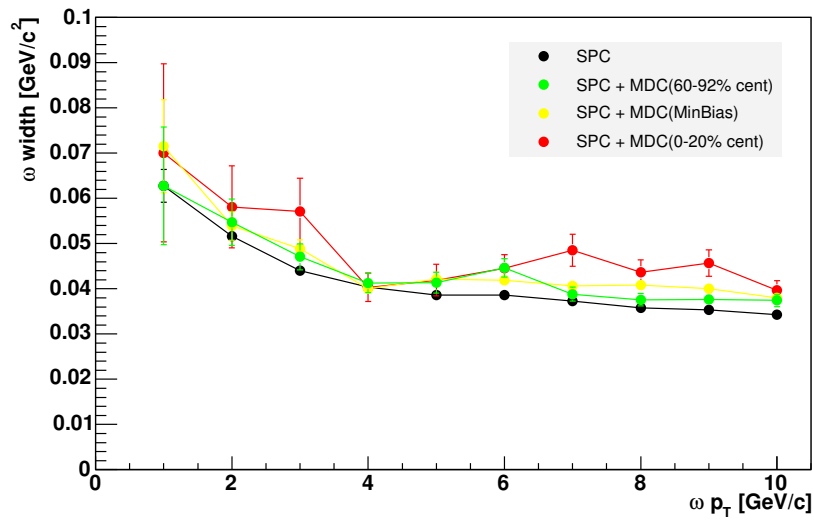


Figure 3.11: Width of ω mass. Black points are from the single ω simulation (considering only SPC) and the others are from the embedding.

It can be seen that the peak position gets higher and the width gets wider if we go to the higher multiplicity. Needless to say that those corrections are indispensable to the study of the mass modification.

We also calculate the efficiency of MDC together with SPC using the Formula 3.3. The Figure 3.12 shows the result. Here, note that we don't input the kinematics cuts for reconstructing ω mesons since we just see the MDC effect. The total efficiency will be calculated later after inputting the appropriate cuts for ω reconstruction.

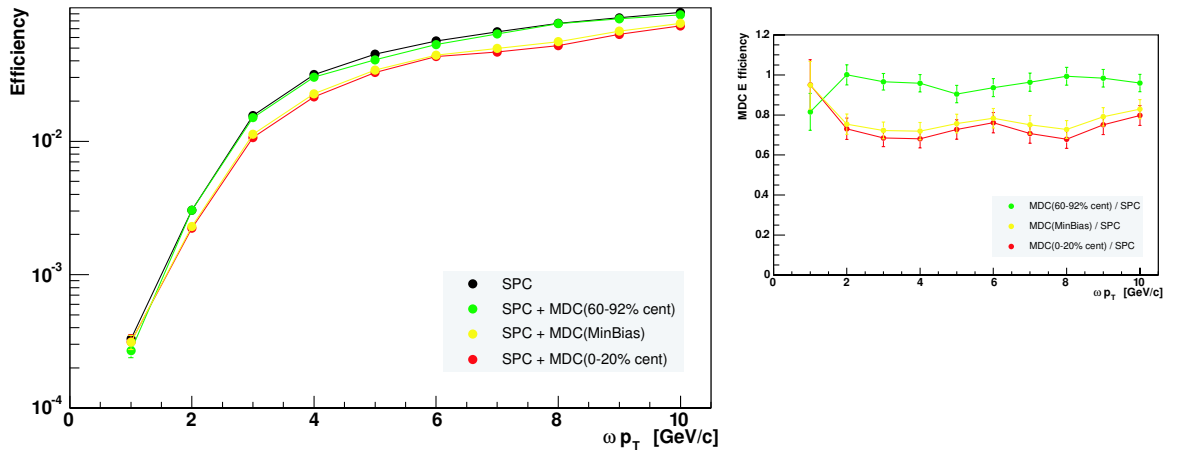


Figure 3.12: Efficiency of SPC and SPC+MDC(left) with the ratio of the efficiency of MDC/SPC for each multiplicity(right).

3.3.4 Cut Optimization

The main issue of this analysis is the huge combinatorial background inevitable for reconstructing particles from the three-body decay mode, i.e. $\omega \rightarrow \pi^0 \gamma$ where $\pi^0 \rightarrow 2\gamma$. If there's no specific cuts for reconstructing ω , Signal to Background (include signal) ratio, $S/(B+S) \simeq S/B$ is less than 10^3 for all statistics of data (see the Figure 3.23) and that makes extremely hard to identify ω mesons. So then an improvement of S/B or the peak significance, S/\sqrt{B} has a vital importance. Here, we consider following parameters that should have a great influence on the peak significance.

- Transverse Momentum Cut (p_T) of π^0
- Photon Energy Cut (except photons from π^0 candidate)
- Width of π^0 Invariant Mass

We investigate those cuts by calculating S/\sqrt{B} according to transverse momentum of ω . The Figure 3.13 shows a roughly method. The simulation data is used for calculating the number of signals and some real data are used for calculating backgrounds (it might be include very few signals but ignorable).

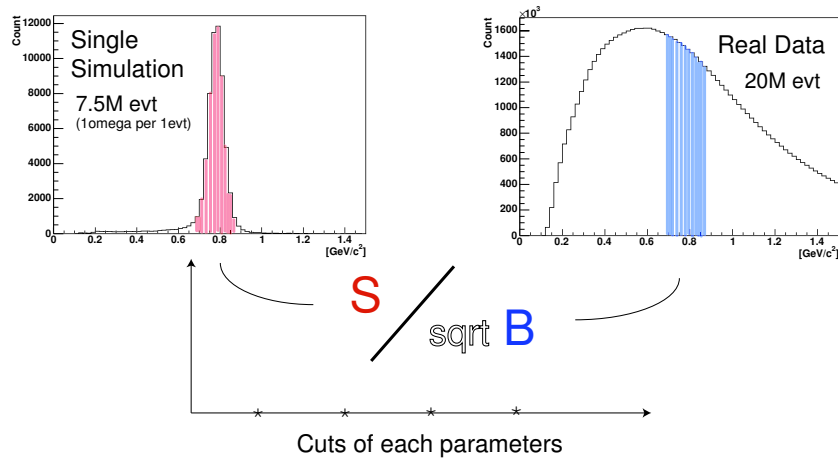


Figure 3.13: Method of Cut Optimization

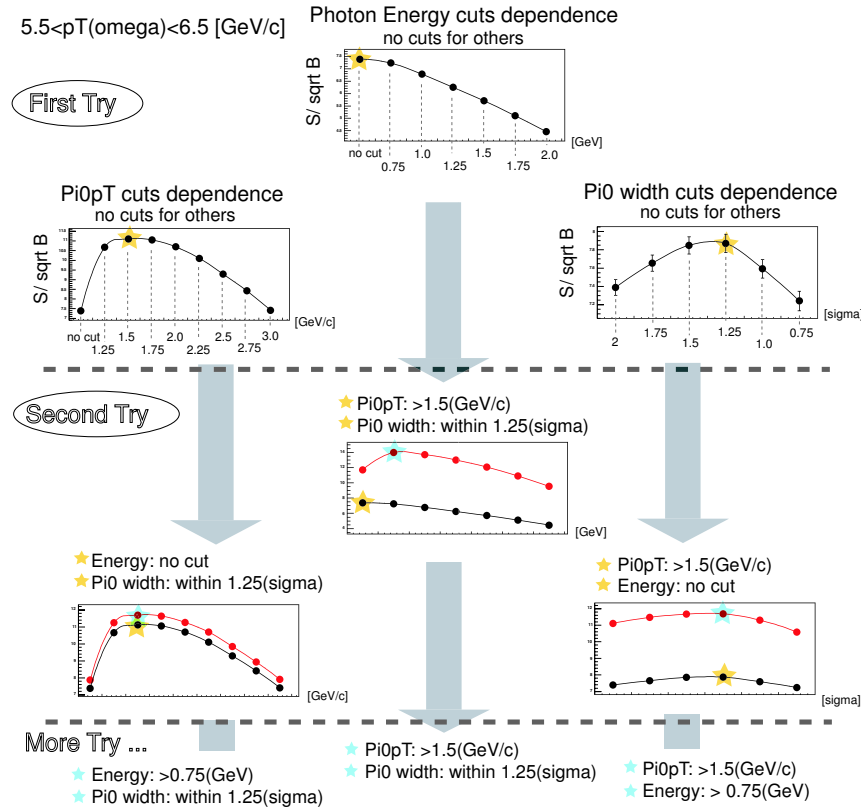


Figure 3.14: Flow chart of Cut Optimization

If calculated S/\sqrt{B} has a peak, so then the cut value which makes the peak is the best cut. However, the best cut cannot be determined by one trial since those cuts, mostly p_T cut and energy cut, are correlative. The Figure 3.14 shows a flow chart of this study (e.x. $5.5 < p_T(\omega) < 6.5$). First, we calculate S/\sqrt{B} with no cuts for each value and find the point that makes the peak (yellow stars in the Figure 3.14). Next, we again calculate S/\sqrt{B} after applying cuts that make the peak before. The trial is continued until best cuts do not change anymore. The results are shown in the Figure 3.15, 3.16 and 3.17. Cuts are determined four times showing in the succeeding Tables. Note that calculated S/\sqrt{B} is relative value since we put single ω much more than estimated number of ω from the collisions. Therefore, absolute S/\sqrt{B} will be calculated in the next section after estimating the number of ω and considering efficiency for all cuts.

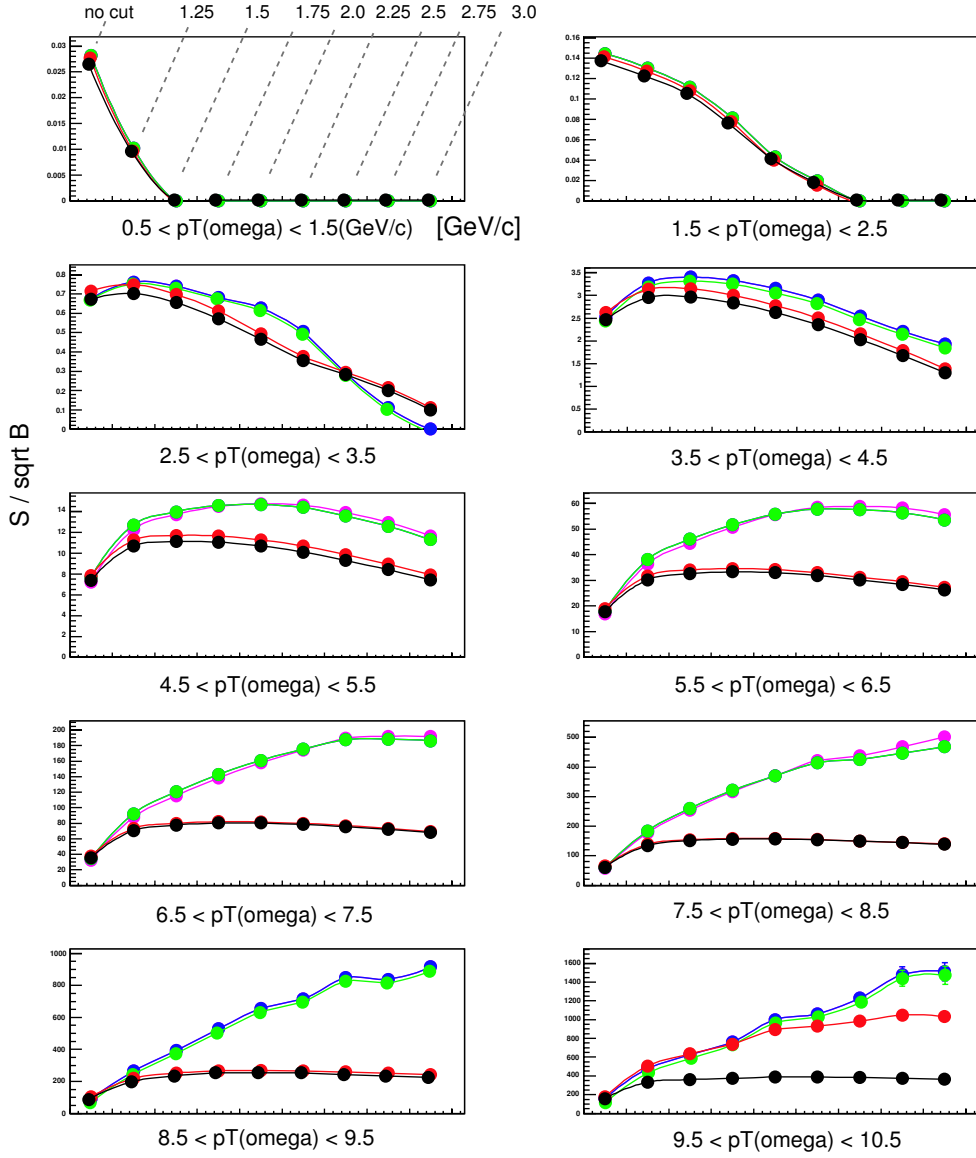


Figure 3.15: S/\sqrt{B} calculation for $\pi^0 p_T$. Black: First Trial(with no cut), Red: Second Trial(with Cut#1 except $\pi^0 p_T$ cut), Green: Third Trial(with Cut#2 except $\pi^0 p_T$ cut), Blue: Forth Trial (with Cut#3 except $\pi^0 p_T$ cut), Magenta: Fifth Trial(with Cut#4 except $\pi^0 p_T$ cut).

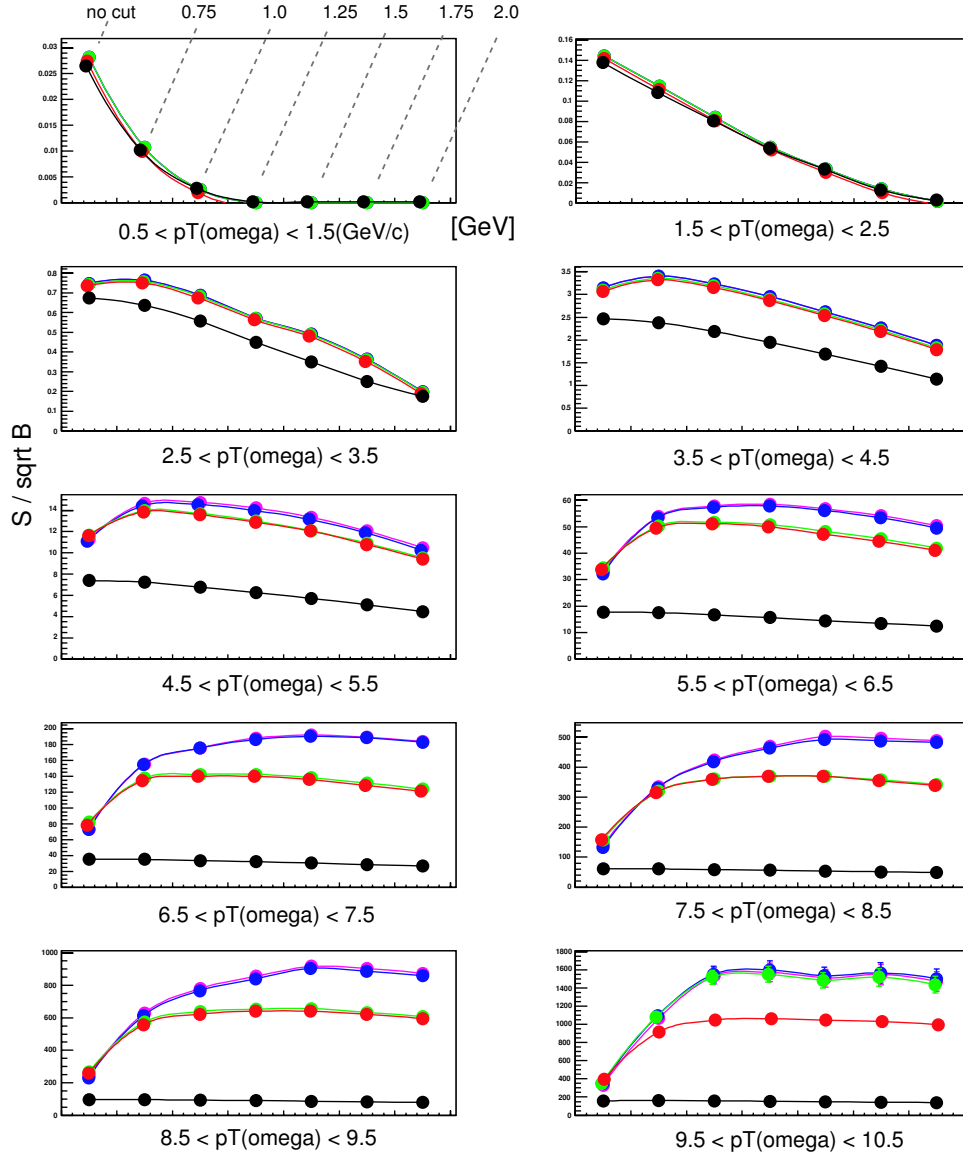


Figure 3.16: S/\sqrt{B} calculation for photon energy cut. Black: First Trial(with no cut), Red: Second Trial(with Cut#1 except γ energy cut), Green: Third Trial(with Cut#2 except γ energy cut), Blue: Forth Trial (with Cut#3 except γ energy cut), Magenta: Fifth Trial(with Cut#4 except γ energy cut).

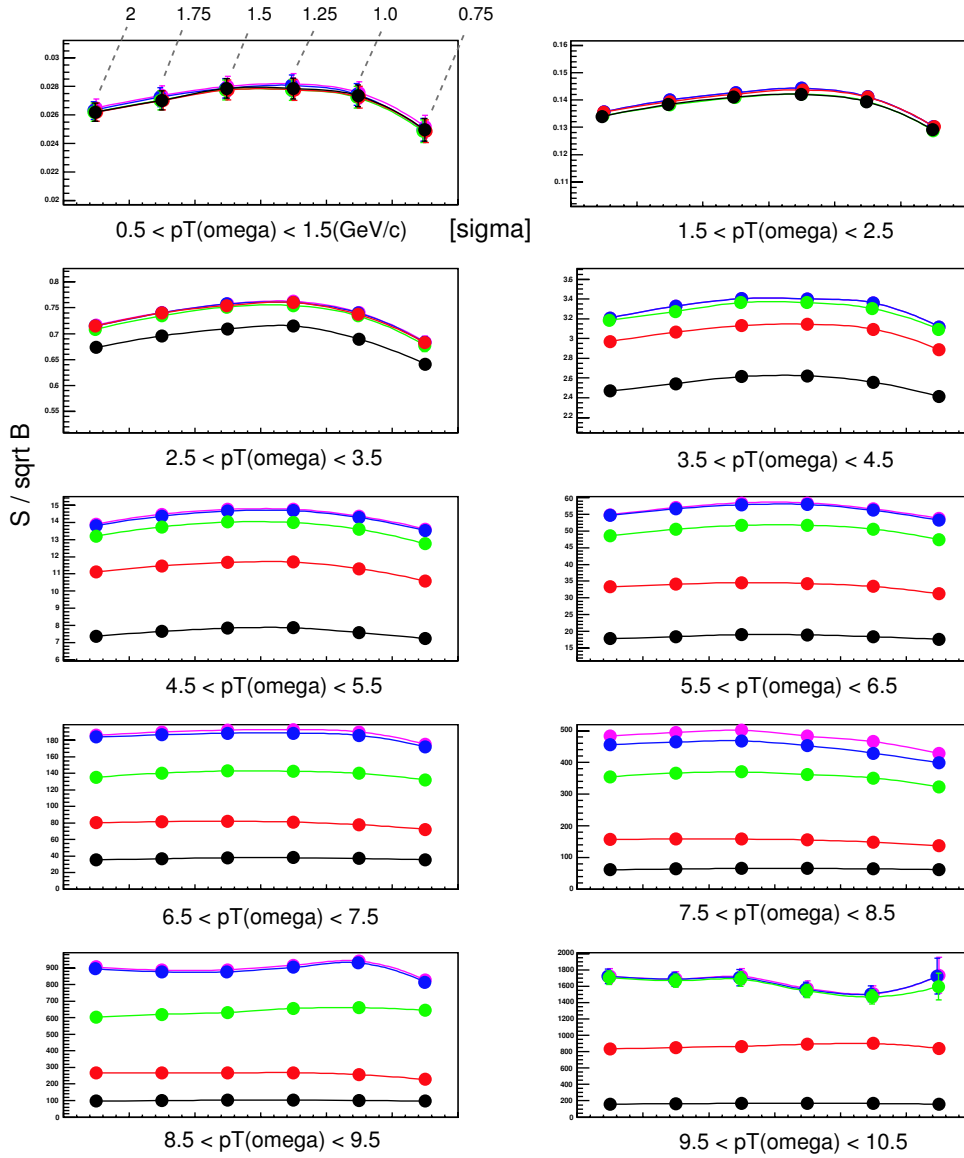


Figure 3.17: S/\sqrt{B} calculation for π^0 mass width. Black: First Trial(with no cut), Red: Second Trial(with Cut#1 except π^0 mass width cut), Green: Third Trial(with Cut#2 except π^0 mass width cut), Blue: Forth Trial (with Cut#3 except π^0 mass width cut), Magenta: Fifth Trial(with Cut#4 except π^0 mass width cut).

Cut #1

	$\pi^0 p_T$ Cut	γ energy Cut	π^0 mass width
$0.5 < p_T(\omega) < 1.5$	no cut	no cut	1.25σ
$1.5 < p_T(\omega) < 2.5$	no cut	no cut	1.25σ
$2.5 < p_T(\omega) < 3.5$	$1.25 <$	no cut	1.25σ
$3.5 < p_T(\omega) < 4.5$	$1.5 <$	no cut	1.25σ
$4.5 < p_T(\omega) < 5.5$	$1.5 <$	no cut	1.25σ
$5.5 < p_T(\omega) < 6.5$	$1.75 <$	no cut	1.5σ
$6.5 < p_T(\omega) < 7.5$	$1.75 <$	no cut	1.5σ
$7.5 < p_T(\omega) < 8.5$	$2.0 <$	no cut	1.5σ
$8.5 < p_T(\omega) < 9.5$	$2.0 <$	no cut	1.25σ
$9.5 < p_T(\omega) < 10.5$	$2.0 <$	$0.75 <$	1.25σ

Cut #2

	$\pi^0 p_T$ Cut	γ energy Cut	π^0 mass width
$0.5 < p_T(\omega) < 1.5$	no cut	no cut	1.25σ
$1.5 < p_T(\omega) < 2.5$	no cut	no cut	1.25σ
$2.5 < p_T(\omega) < 3.5$	$1.25 <$	$0.75 <$	1.25σ
$3.5 < p_T(\omega) < 4.5$	$1.5 <$	$0.75 <$	1.25σ
$4.5 < p_T(\omega) < 5.5$	$1.5 <$	$0.75 <$	1.25σ
$5.5 < p_T(\omega) < 6.5$	$1.75 <$	$1.0 <$	1.5σ
$6.5 < p_T(\omega) < 7.5$	$1.75 <$	$1.25 <$	1.5σ
$7.5 < p_T(\omega) < 8.5$	$2.0 <$	$1.25 <$	1.5σ
$8.5 < p_T(\omega) < 9.5$	$2.0 <$	$1.5 <$	1.25σ
$9.5 < p_T(\omega) < 10.5$	$2.75 <$	$1.5 <$	1.5σ

Cut #3

	$\pi^0 p_T$ Cut	γ energy Cut	π^0 mass width
$0.5 < p_T(\omega) < 1.5$	no cut	no cut	1.25σ
$1.5 < p_T(\omega) < 2.5$	no cut	no cut	1.25σ
$2.5 < p_T(\omega) < 3.5$	$1.25 <$	$0.75 <$	1.25σ
$3.5 < p_T(\omega) < 4.5$	$1.5 <$	$0.75 <$	1.25σ
$4.5 < p_T(\omega) < 5.5$	$2.0 <$	$0.75 <$	1.25σ
$5.5 < p_T(\omega) < 6.5$	$2.25 <$	$1.0 <$	1.5σ
$6.5 < p_T(\omega) < 7.5$	$2.75 <$	$1.25 <$	1.5σ
$7.5 < p_T(\omega) < 8.5$	$3.0 <$	$1.25 <$	1.5σ
$8.5 < p_T(\omega) < 9.5$	$3.0 <$	$1.5 <$	1.25σ
$9.5 < p_T(\omega) < 10.5$	$3.0 <$	$1.5 <$	1.5σ

Cut #4

	$\pi^0 p_T$ Cut	γ energy Cut	π^0 mass width
$0.5 < p_T(\omega) < 1.5$	no cut	no cut	1.25σ
$1.5 < p_T(\omega) < 2.5$	no cut	no cut	1.25σ
$2.5 < p_T(\omega) < 3.5$	$1.25 <$	$0.75 <$	1.25σ
$3.5 < p_T(\omega) < 4.5$	$1.5 <$	$0.75 <$	1.25σ
$4.5 < p_T(\omega) < 5.5$	$2.0 <$	$1.0 <$	1.25σ
$5.5 < p_T(\omega) < 6.5$	$2.25 <$	$1.25 <$	1.5σ
$6.5 < p_T(\omega) < 7.5$	$2.75 <$	$1.5 <$	1.5σ
$7.5 < p_T(\omega) < 8.5$	$3.0 <$	$1.5 <$	1.5σ
$8.5 < p_T(\omega) < 9.5$	$3.0 <$	$1.5 <$	1.25σ
$9.5 < p_T(\omega) < 10.5$	$3.0 <$	$1.5 <$	1.5σ

3.3.5 Feasibility

We evaluate the SPC and the MDC. Furthermore, we find the cuts that improve S/\sqrt{B} ratio. So then everyone would think that, "In the Real Data of Au+Au, can ω mesons (via radiative decay mode) be truly seen?". Here, we study its actual feasibility, that is, absolute S/\sqrt{B} value for full statistics.

First, let us estimate the number of measured ω coming from Au+Au collisions. We take advantage of the cross section of π^0 [47] and the ratio of ω/π^0 [48] that are already shown up for the PHENIX's results in p+p collisions (see the the Figure 3.18). The cross section of π^0 are fit to the

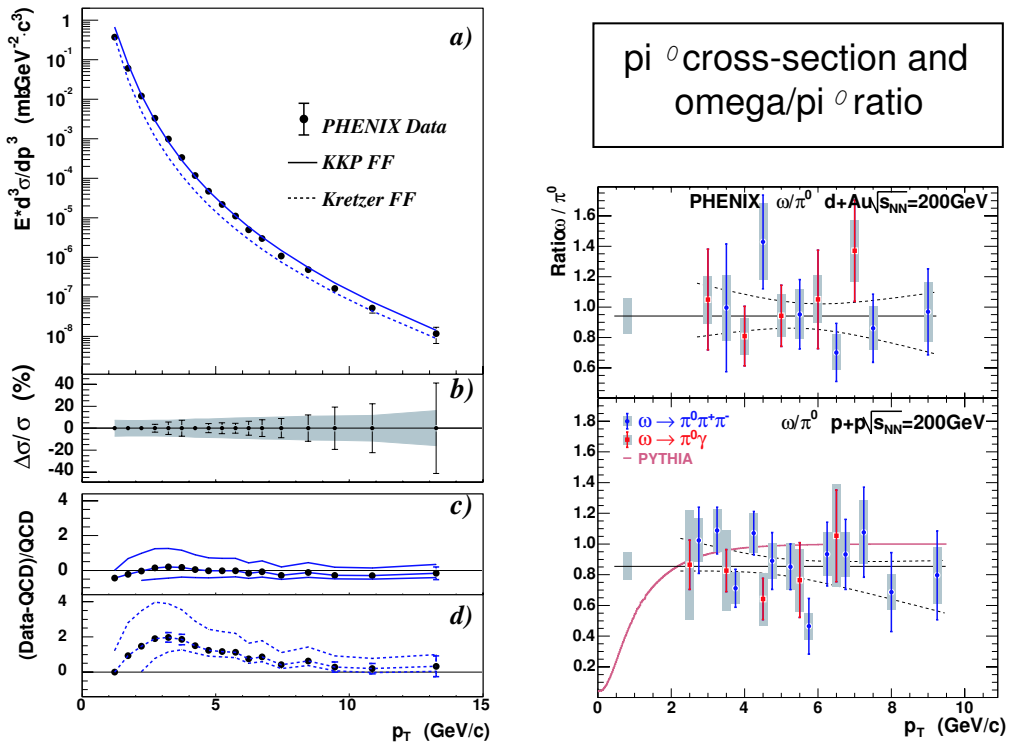


Figure 3.18: The invariant differential cross section for inclusive π^0 production and the results from NLO pQCD calculations with equal renormalization and factorization scales of p_T [47] (left). ω/π^0 in d+Au and p+p collisions at $\sqrt{s_{NN}} = 200\text{GeV}$ [48] (right).

following Hagedorn-type function [47] as,

$$E \cdot d^3\sigma/dp^3 = A \cdot (p_t^0)^n / (p_T + p_T^0)^n. \quad (3.4)$$

The fit parameters are $A=386\text{mb}\cdot\text{GeV}^{-2} \cdot c^3$, $p_0=1.219 \text{ GeV}/c$ and $n=9.99$ for both PbSc and PbGl. So then the estimated ω cross section in Au+Au collisions is,

$$(E \cdot d^3\sigma/dp^3)_\omega = (E \cdot d^3\sigma/dp^3)_{\pi^0} \cdot R_{\omega/\pi^0} / \sigma_{pp}, \quad (3.5)$$

where R_{ω/π^0} is the ω/π^0 ratios in p+p collisions, (supposed 0.85 as seen in the Figure 3.18), σ_{pp} is the total cross section of p+p at $\sqrt{s_{NN}} = 200\text{GeV}$ as 42.2 mb[5]. The Figure 3.19 shows the slope of the estimated cross section of ω . While the estimated number of measured ω is written as,

$$N_\omega^{raw} = 2\pi p_T \cdot (E \cdot d^3\sigma/dp^3)_\omega \cdot BR \cdot N_{evt} \cdot N_{coll} \cdot eff, \quad (3.6)$$

where BR is the branching ratio of $\omega \rightarrow \pi^0\gamma$ as 8.9%[5], N_{evt} is the number of events which can be evaluated from the real data analysis, N_{coll} is the number of binary collisions calculated from the Au+Au Glauber Monte Carlo[49], which is based on a simple geometrical picture of a nucleus-nucleus collision and eff is the total efficiency including all cuts.

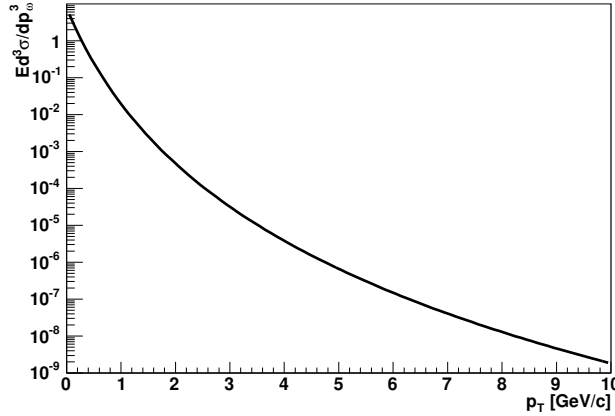


Figure 3.19: Estimated cross section of ω by the Formula 3.5 ignoring all errors.

So then we calculate the total efficiency for each cuts determined in previous. The Figure 3.20, 3.21 and 3.22 show the results for three multiplicity. Applying all values, we estimate the number of ω that could be measured in this analysis ignoring an effect of the matter that created in the heavy ion collisions. The number is tabulated in the Table 3.3.5. Using this number and scaling down the relative S/B and S/\sqrt{B} that we calculated for the cut optimization, finally we evaluate the absolute S/B and S/\sqrt{B} for the real data analysis (see the Figure 3.23 and 3.24). It shows that tighter cuts improve S/\sqrt{B} significantly at high p_T in MinBias and central events, at mid p_T in peripheral events. The value is up to 4, implying that it is possible to measure ω if we use the appropriate cuts and read full statistics.

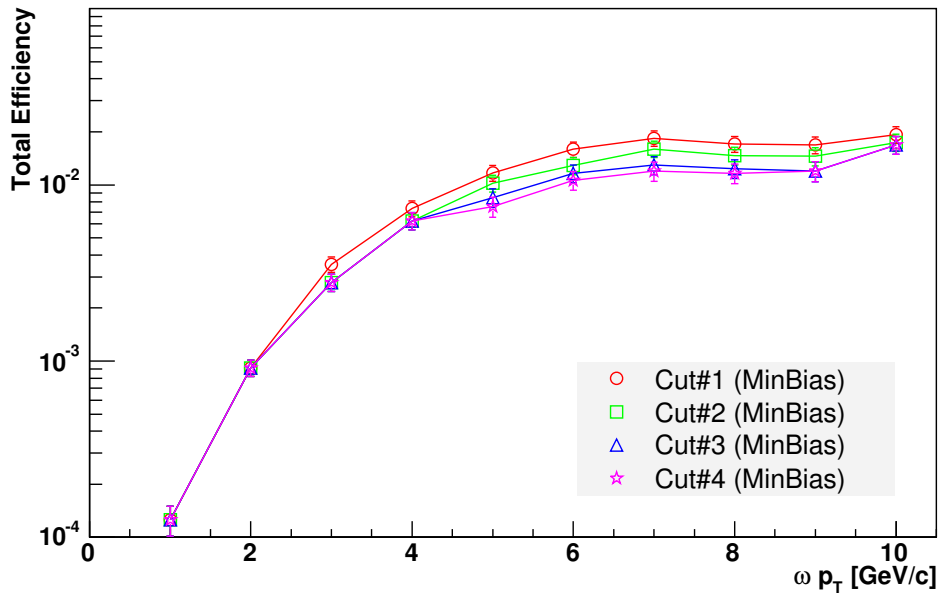


Figure 3.20: Total Efficiency for each Cuts (see the previous section) in the MinBias Event

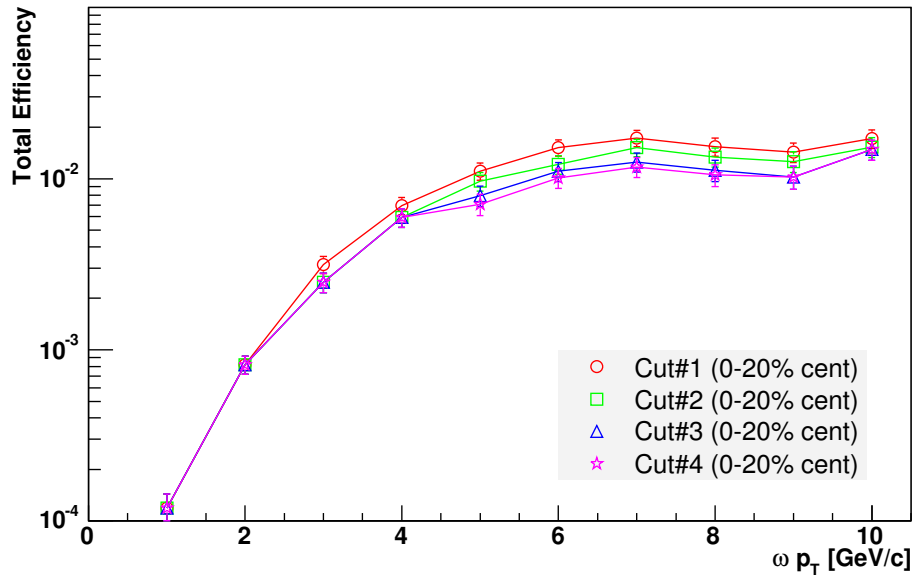


Figure 3.21: Total Efficiency for each Cuts in the 0-20% centrality event

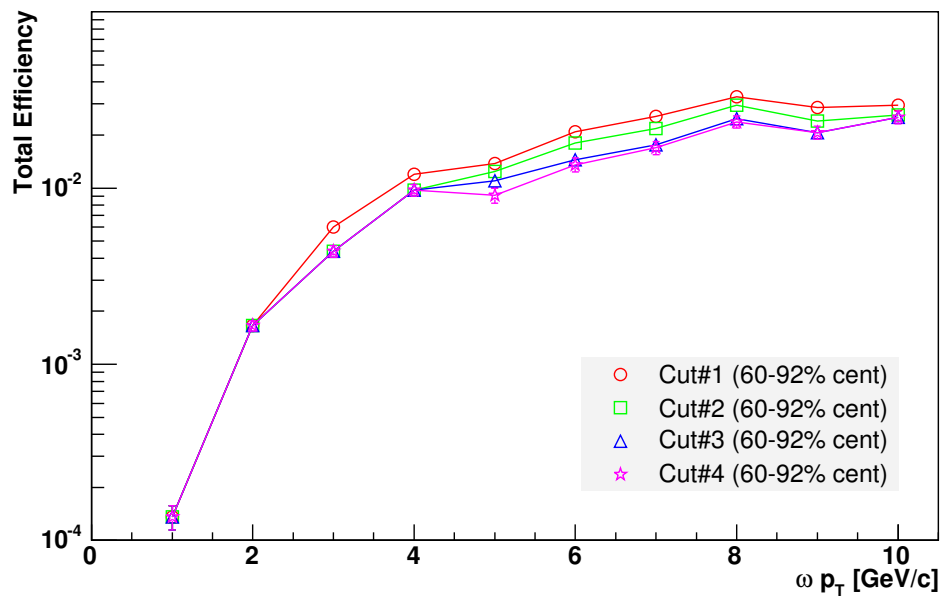


Figure 3.22: Total Efficiency for each Cuts in the 60-92% centrality event

	Cuts	$N_{\omega}^{est}(\text{MinBias})$	$N_{\omega}^{est}(0-20\%)$	$N_{\omega}^{est}(60-92\%)$
$0.5 < p_T(\omega) < 1.5$	#1	$7.70 \times 10^5 \pm 1.02 \times 10^5$	$3.92 \times 10^5 \pm 8.35 \times 10^4$	$1.34 \times 10^4 \pm 2.09 \times 10^3$
	#2	$7.70 \times 10^5 \pm 1.02 \times 10^5$	$3.92 \times 10^5 \pm 8.35 \times 10^4$	$1.34 \times 10^4 \pm 2.09 \times 10^3$
	#3	$7.70 \times 10^5 \pm 1.02 \times 10^5$	$3.92 \times 10^5 \pm 8.35 \times 10^4$	$1.34 \times 10^4 \pm 2.09 \times 10^3$
	#4	$7.70 \times 10^5 \pm 1.02 \times 10^5$	$3.92 \times 10^5 \pm 8.35 \times 10^4$	$1.34 \times 10^4 \pm 2.09 \times 10^3$
$1.5 < p_T(\omega) < 2.5$	#1	$2.46 \times 10^5 \pm 1.68 \times 10^4$	$1.06 \times 10^5 \pm 1.27 \times 10^4$	$6.39 \times 10^3 \pm 4.22 \times 10^2$
	#2	$2.46 \times 10^5 \pm 1.68 \times 10^4$	$1.06 \times 10^5 \pm 1.27 \times 10^4$	$6.39 \times 10^3 \pm 4.22 \times 10^2$
	#3	$2.46 \times 10^5 \pm 1.68 \times 10^4$	$1.06 \times 10^5 \pm 1.27 \times 10^4$	$6.39 \times 10^3 \pm 4.22 \times 10^2$
	#4	$2.46 \times 10^5 \pm 1.68 \times 10^4$	$1.06 \times 10^5 \pm 1.27 \times 10^4$	$6.39 \times 10^3 \pm 4.22 \times 10^2$
$2.5 < p_T(\omega) < 3.5$	#1	$8.71 \times 10^4 \pm 5.89 \times 10^3$	$3.66 \times 10^4 \pm 4.23 \times 10^3$	$2.08 \times 10^3 \pm 1.37 \times 10^2$
	#2	$6.93 \times 10^4 \pm 5.08 \times 10^3$	$2.88 \times 10^4 \pm 3.75 \times 10^3$	$1.51 \times 10^3 \pm 1.16 \times 10^2$
	#3	$6.93 \times 10^4 \pm 5.08 \times 10^3$	$2.88 \times 10^4 \pm 3.75 \times 10^3$	$1.51 \times 10^3 \pm 1.16 \times 10^2$
	#4	$6.93 \times 10^4 \pm 5.08 \times 10^3$	$2.88 \times 10^4 \pm 3.75 \times 10^3$	$1.51 \times 10^3 \pm 1.16 \times 10^2$
$3.5 < p_T(\omega) < 4.5$	#1	$2.29 \times 10^4 \pm 1.67 \times 10^3$	$1.21 \times 10^4 \pm 1.39 \times 10^3$	$6.19 \times 10^2 \pm 4.27 \times 10$
	#2	$1.92 \times 10^4 \pm 1.53 \times 10^3$	$1.03 \times 10^4 \pm 1.28 \times 10^3$	$5.03 \times 10^2 \pm 3.84 \times 10$
	#3	$1.92 \times 10^4 \pm 1.53 \times 10^3$	$1.03 \times 10^4 \pm 1.28 \times 10^3$	$5.03 \times 10^2 \pm 3.84 \times 10$
	#4	$1.92 \times 10^4 \pm 1.53 \times 10^3$	$1.03 \times 10^4 \pm 1.28 \times 10^3$	$5.03 \times 10^2 \pm 3.84 \times 10$
$4.5 < p_T(\omega) < 5.5$	#1	$7.72 \times 10^3 \pm 5.54 \times 10^2$	$4.03 \times 10^3 \pm 4.59 \times 10^2$	$1.49 \times 10^2 \pm 1.20 \times 10$
	#2	$6.82 \times 10^3 \pm 5.2 \times 10^2$	$3.51 \times 10^3 \pm 4.28 \times 10^2$	$1.34 \times 10^2 \pm 1.13 \times 10$
	#3	$5.72 \times 10^3 \pm 4.76 \times 10^2$	$2.89 \times 10^3 \pm 3.88 \times 10^2$	$1.19 \times 10^2 \pm 1.07 \times 10$
	#4	$5.06 \times 10^3 \pm 4.47 \times 10^2$	$2.58 \times 10^3 \pm 3.66 \times 10^2$	$9.83 \times 10 \pm 9.69$
$5.5 < p_T(\omega) < 6.5$	#1	$2.71 \times 10^3 \pm 1.91 \times 10^2$	$1.46 \times 10^3 \pm 1.61 \times 10^2$	$5.99 \times 10 \pm 4.41$
	#2	$2.27 \times 10^3 \pm 1.74 \times 10^2$	$1.16 \times 10^3 \pm 1.43 \times 10^2$	$5.16 \times 10 \pm 4.08$
	#3	$2.02 \times 10^3 \pm 1.64 \times 10^2$	$1.06 \times 10^3 \pm 1.37 \times 10^2$	$4.14 \times 10 \pm 3.66$
	#4	$1.81 \times 10^3 \pm 1.55 \times 10^2$	$9.73 \times 10^2 \pm 1.31 \times 10^2$	$3.88 \times 10 \pm 3.54$
$6.5 < p_T(\omega) < 7.5$	#1	$1.03 \times 10^3 \pm 7.04 \times 10$	$5.22 \times 10^2 \pm 5.74 \times 10$	$2.39 \times 10 \pm 1.64$
	#2	$8.54 \times 10^2 \pm 6.40 \times 10$	$4.67 \times 10^2 \pm 5.38 \times 10$	$1.96 \times 10 \pm 1.51$
	#3	$6.56 \times 10^2 \pm 5.60 \times 10$	$3.79 \times 10^2 \pm 4.88 \times 10$	$1.58 \times 10 \pm 1.35$
	#4	$5.80 \times 10^2 \pm 5.26 \times 10$	$3.54 \times 10^2 \pm 4.72 \times 10$	$1.52 \times 10 \pm 1.33$
$7.5 < p_T(\omega) < 8.5$	#1	$3.73 \times 10^2 \pm 2.63 \times 10$	$1.67 \times 10^2 \pm 2.01 \times 10$	$1.07 \times 10 \pm 0.69$
	#2	$3.08 \times 10^2 \pm 2.38 \times 10$	$1.46 \times 10^2 \pm 1.88 \times 10$	9.52 ± 0.65
	#3	$2.66 \times 10^2 \pm 2.21 \times 10$	$1.22 \times 10^2 \pm 1.71 \times 10$	8.00 ± 0.60
	#4	$2.50 \times 10^2 \pm 2.14 \times 10$	$1.15 \times 10^2 \pm 1.66 \times 10$	7.69 ± 0.59
$8.5 < p_T(\omega) < 9.5$	#1	$1.72 \times 10^2 \pm 1.18 \times 10$	$6.19 \times 10 \pm 8.04$	3.70 ± 0.27
	#2	$1.43 \times 10^2 \pm 1.07 \times 10$	$5.46 \times 10 \pm 7.55$	3.10 ± 0.24
	#3	$1.20 \times 10^2 \pm 9.77$	$4.43 \times 10 \pm 6.79$	2.66 ± 0.23
	#4	$1.20 \times 10^2 \pm 9.77$	$4.43 \times 10 \pm 6.79$	2.66 ± 0.23
$9.5 < p_T(\omega) < 10.5$	#1	$7.76 \times 10 \pm 5.44$	$3.23 \times 10 \pm 4.01$	1.66 ± 0.12
	#2	$7.24 \times 10 \pm 5.25$	$2.88 \times 10 \pm 3.78$	1.46 ± 0.12
	#3	$6.98 \times 10 \pm 5.15$	$2.79 \times 10 \pm 3.72$	1.41 ± 0.11
	#4	$6.98 \times 10 \pm 5.15$	$2.79 \times 10 \pm 3.72$	1.41 ± 0.11

Table 3.1: Estimated number of measured ω at $N_{evt} = 1.06 \times 10^9$. Only the error of efficiency is considered.

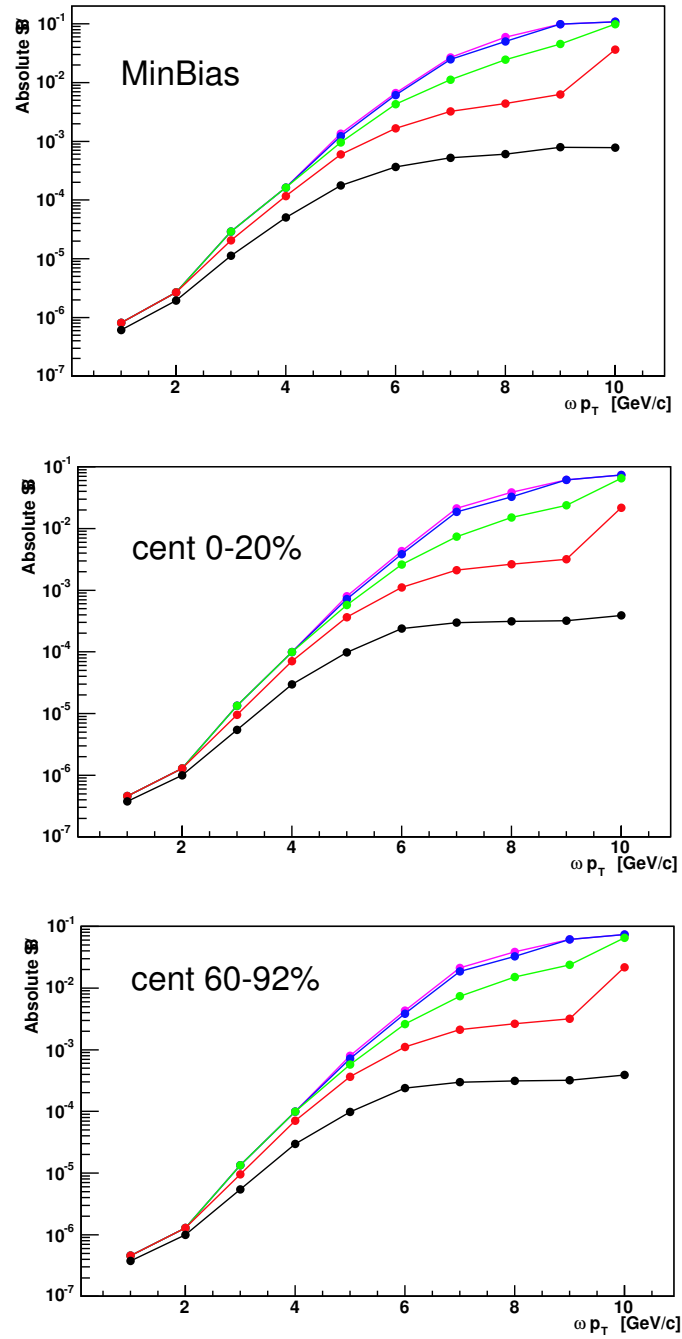


Figure 3.23: Absolute S/B for MinBias($N_{evt} = 1,057,22,600.$) ,0-20% and 60-92% central. Black: no cut, Red: with Cut#1, Green: with Cut#2, Blue: with Cut#3, Magenta: with Cut#4)

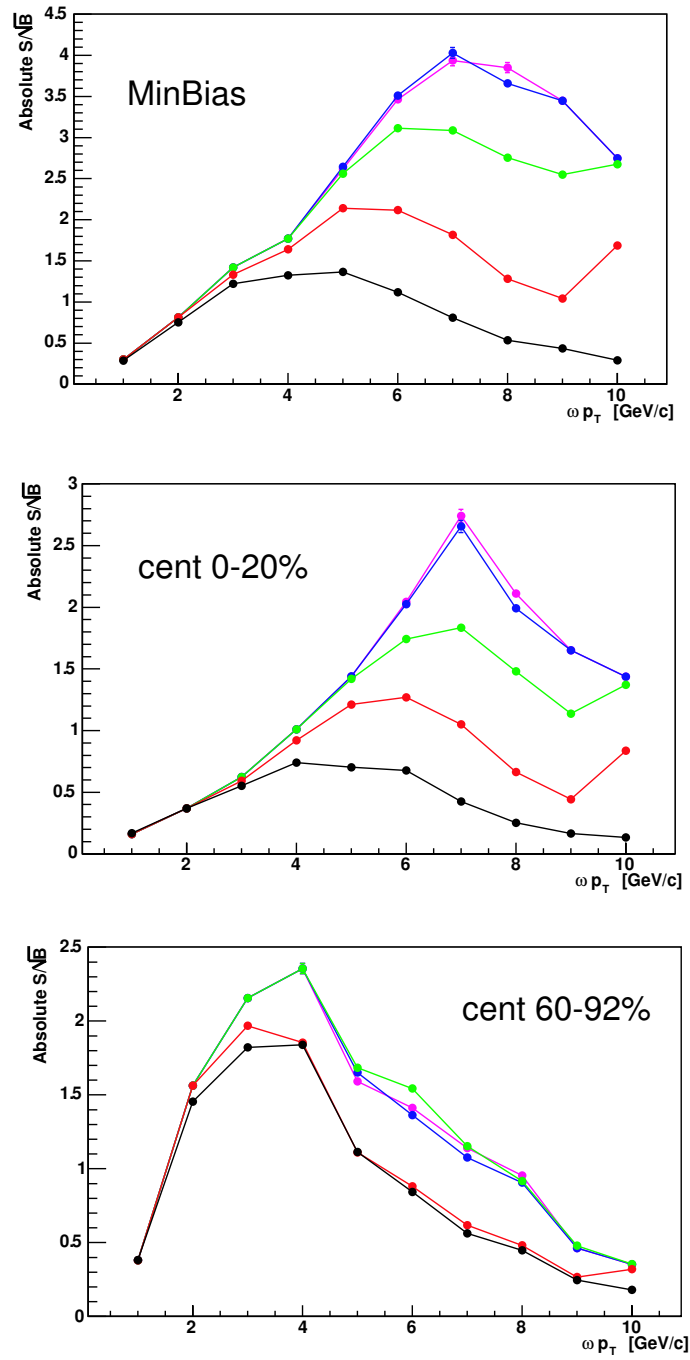


Figure 3.24: Absolute S/\sqrt{B} for MinBias($N_{evt} = 1,057,22,600.$) ,0-20% and 60-92% central. Black: no cut, Red: with Cut#1, Green: with Cut#2, Blue: with Cut#3, Magenta: with Cut#4)

3.4 Signal Selection

We now discuss in detail of the real data analysis step by step. First, we chose the *Trigger* and put cuts for the *Photon Identification* in EMCal. Next, we reconstruct π^0 from 2γ . *Distribution of π^0 Invariant Mass* shows that π^0 's mean and width depend on transverse momentum of π^0 . And because of that, we have to carefully chose π^0 's for reconstructing ω . In the end, we put *Best Cuts for Reconstructing ω* done by the feasibility study in the previous section.

3.4.1 Trigger

Minimum Bias Trigger

The condition for accepting an inelastic Au+Au reaction is given by the BBC and the ZDC. The collision has to trigger at least two photomultipliers at a time in both BBCs and cause a signal in both ZDCs. The Minimum Bias Trigger is as the logical AND(&&) of a coincidence between the north and south BBC, as well as the north and south ZDC. This trigger accepts 92% of the geometrical cross section for Au+Au collisions.

BBC Vertex Cuts

We require that the z vertex (determined by BBC) of a given event lies within the range as,

$$\sqrt{|z|} < 30 \text{ cm},$$

in order to exclude regions that are shadowed by the pole tips of the central magnet and to minimize the background of scattered particles.

Event Centrality

The "centrality", the value to characterize the heavy ion collisions is determined via the correlation between the energy deposit in the ZDC and the charge deposit in the BBC (see the Figure 3.26). A brief explanation is shown in the Figure 3.25. For this analysis, we consider 3 parts of centrality, 0-20% cent 60-92% and MinBias.

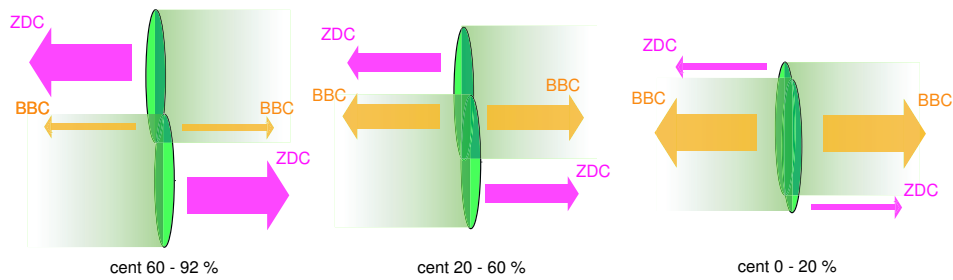


Figure 3.25: The more the collisions is central, the more BBC collects the participants of the collisions and the less ZDC collects the spectators.

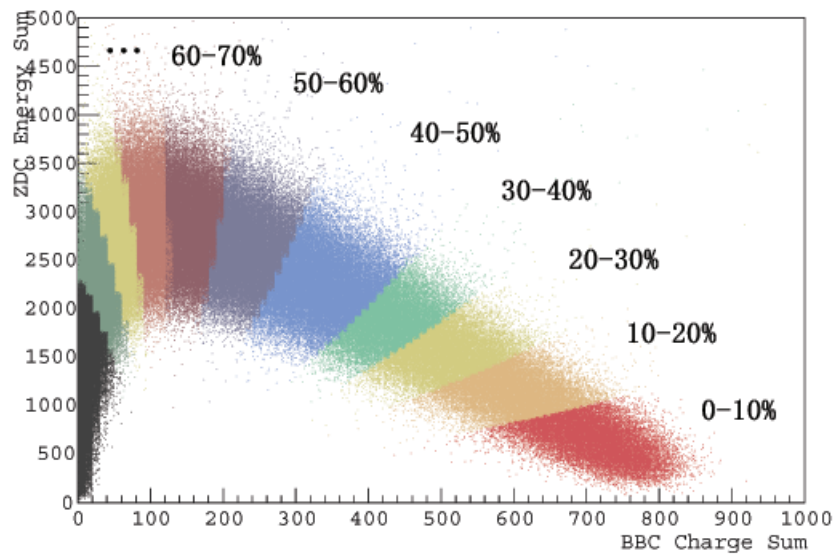


Figure 3.26: Correlation of BBC and ZDC

3.4.2 Photon Identification

Excluded Modules

We use both PbSc and PbG1 for measuring photons. Since there're some bad modules in the EMCal that distort the energy measurement of a hit, we have to apply quality criteria to the clusters. Modules without any energy signal mostly due to faulty photomultipliers are denoted as "dead". It is also critical to exclude modules that only sporadically contribute in a wrong way to the signal. Those are denoted as "warn" determined by suspicious energy spectra. Additionally, the edge modules of the detector are considered to have a dead neighbor to exclude clusters that suffer from leakage at the calorimeter edge. So then we cut those modules, too.

✓ *deadmap* and *warnmap* cut

A map of the excluded area in each detector is shown in the Figure 3.27. White area considered as dead and warn is all excluded during this analysis.

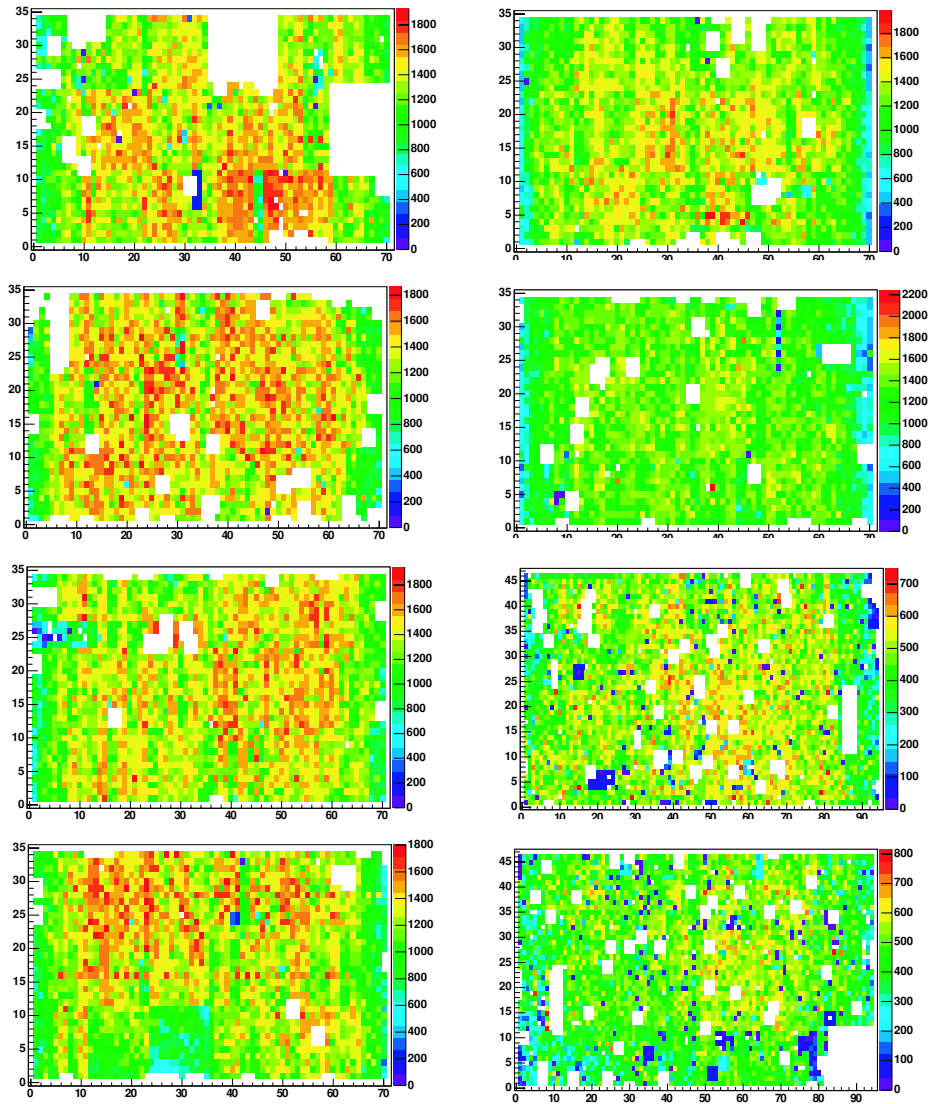


Figure 3.27: Excluded Modules in the EMCAL. Maps on the left side are in the west arm and maps on the right side are in the east arm. Lower two maps on the right side are PbGl and the others are PbSc.

Corrected Energy

To facilitate the measurement of photons in the EMCal, certain valuables for their identification are introduced. First of all, we put raw energy cut as,

$$\sqrt{\text{Raw Energy Cut, } E > 0.2 \text{ (GeV),}}$$

since there's a lot of background from hadrons in low energy region. Furthermore, a cut on the shower shape is more effective to subtract hadrons because an hadronic shower usually spreads over more modules than an electromagnetic shower. We select the corrected energy and apply χ^2 as,

$$\sqrt{E_{core} (\text{prob} > 0.02)), \chi^2 < 3}$$

Definitions of E_{core} and χ^2 are described in the Section 2.2.4.

TOF Cut

In addition to the energy cut, a Time-Of-Flight cut can also reject hadrons since hadrons have heavier mass. We put following cut from the width of the TOF distribution (see the Figure 3.28),

$$\sqrt{|TOF - bbct0| < 2.0(ns)}$$

, where $bbct0$ denotes a time of collisions measured by BBC.

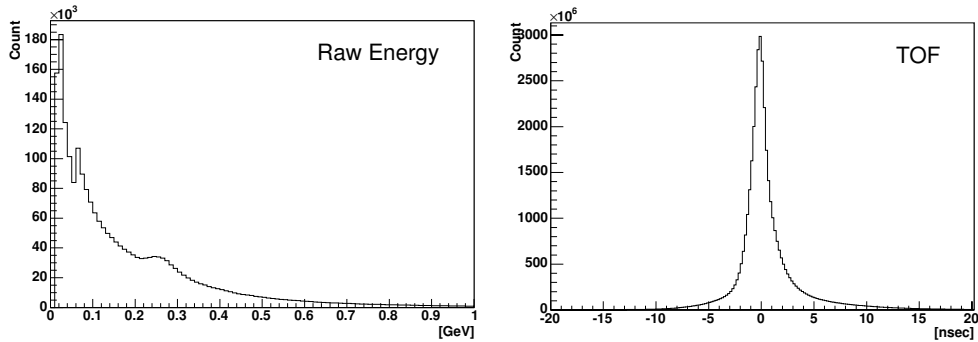


Figure 3.28: The distributions of Energy (left) and TOF(right). A plateau seen in the energy distribution is generated by Minimum Ionizing Particles.

3.4.3 Distribution of π^0 Invariant Mass

Before going to reconstruct ω mesons, π^0 going to 2γ is needed to reconstruct, first. We put following selections for choosing π^0 .

π^0 Legs Selection

- ✓ Both photons in the same EMCal Sector
- ✓ Energy Assymetry Cut $|E_1 - E_2|/|E_1 + E_2| < 0.8$

We require above conditions to cut some asymmetric pairs.

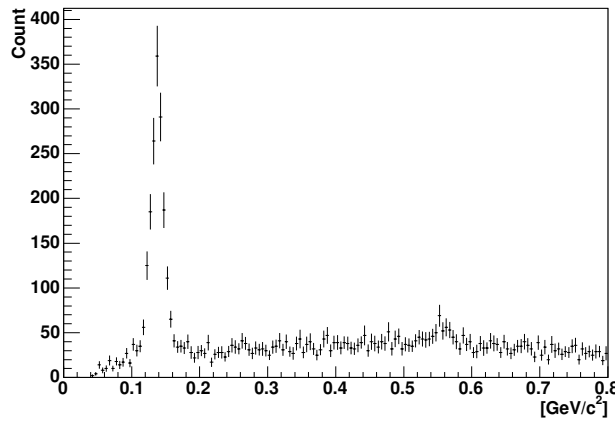


Figure 3.29: Example of Invariant Mass reconstructed from 2 photons

As seen in the Figure 3.29, an example spectrum, π^0 around $0.135 \text{ GeV}/c^2$ clearly can be identified(also, η can be seen around $0.56 \text{ GeV}/c^2$).

Dependence on $\pi^0 p_T$

The position of π^0 mass and the width have a dependence on $\pi^0 p_T$ as seen in the Figure 3.30 and 3.31. Observed position shift upward due to the effect of photon conversion before arriving to EMCal and due to the p_T smearing caused from the steep p_T distribution of π^0 . Also, the multiplicity affects those value. We consider this shift parameter according to the $\pi^0 p_T$ and the centrality when reconstructing ω .

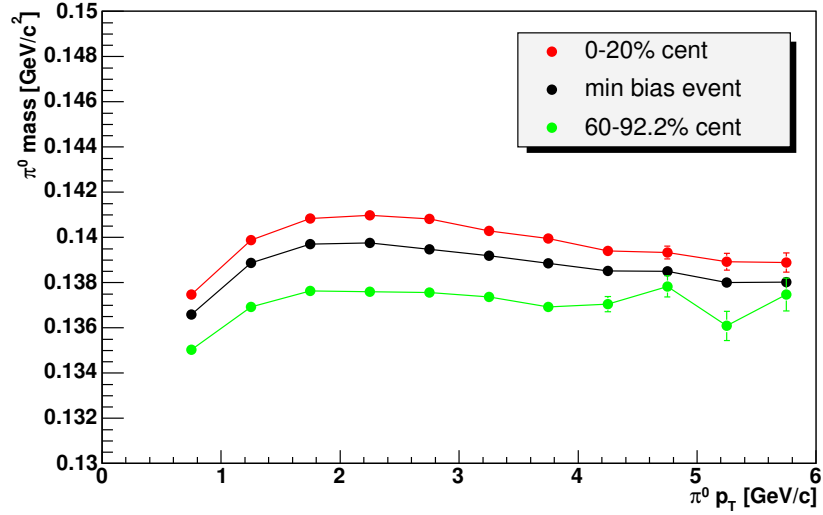


Figure 3.30: Position of π^0 peak as a function of $\pi^0 p_T$

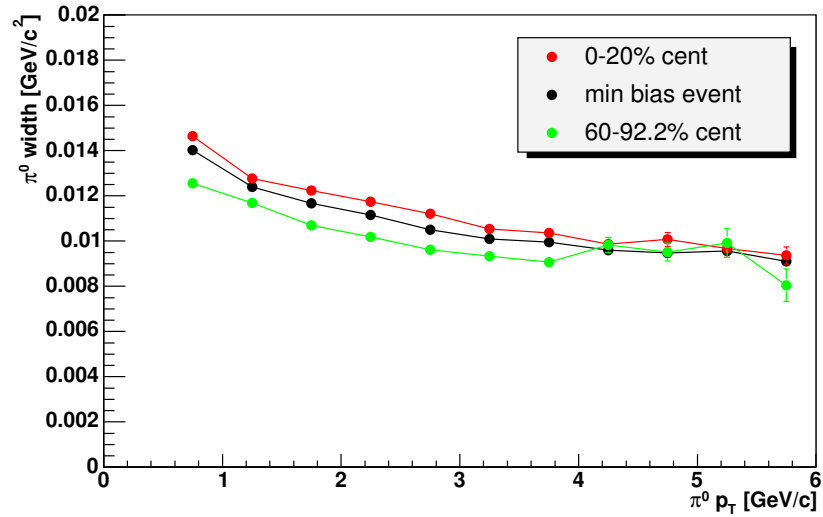


Figure 3.31: Width of π^0 mass as a function of $\pi^0 p_T$

3.4.4 Best Cuts for Reconstructing ω

Thanks to the cut optimization study in advance, we know the other parameters that improve expected S/\sqrt{B} most. We consider following values and apply the Cut # 4 tabulated in the Table 3.4.4

- ✓ Transverse Momentum Cut of π^0
- ✓ Photon Energy Cut except π^0 candidate
- ✓ Width of π^0 Invariant Mass

	$\pi^0 p_T$ Cut	γ energy Cut	π^0 mass width
$0.5 < p_T(\omega) < 1.5$	no cut	no cut	1.25σ
$1.5 < p_T(\omega) < 2.5$	no cut	no cut	1.25σ
$2.5 < p_T(\omega) < 3.5$	$1.25<$	$0.75<$	1.25σ
$3.5 < p_T(\omega) < 4.5$	$1.5<$	$0.75<$	1.25σ
$4.5 < p_T(\omega) < 5.5$	$2.0<$	$1.0<$	1.25σ
$5.5 < p_T(\omega) < 6.5$	$2.25<$	$1.25<$	1.5σ
$6.5 < p_T(\omega) < 7.5$	$2.75<$	$1.5<$	1.5σ
$7.5 < p_T(\omega) < 8.5$	$3.0<$	$1.5<$	1.5σ
$8.5 < p_T(\omega) < 9.5$	$3.0<$	$1.5<$	1.25σ
$9.5 < p_T(\omega) < 10.5$	$3.0<$	$1.5<$	1.5σ

Table 3.2: Cut #4 values

Chapter 4

Results and Discussion

Here, we show the results after analyzing $N_{evt} = 1.06 \times 10^9$ Minimum Bias events(full statistics). Invariant mass spectra are shown first and we consider the background from that. Next, an innovative way for the background subtraction is applied and we look ω mass with simulated results. The outlook for the further analysis is discussed in the end.

4.1 Invariant Mass Spectra

The invariant mass spectra according to ωp_T are shown in the Figure 4.1,4.3 and 4.3, according to three centrality, MinBias, 0-20% and 60-92.2%. ω , around $0.78(\text{GeV}/c^2)$, is getting to appear in high p_T region. The background around $0.6-0.7(\text{GeV}/c^2)$ (will be discussed in the next) is an obstruction on the signal of ω .

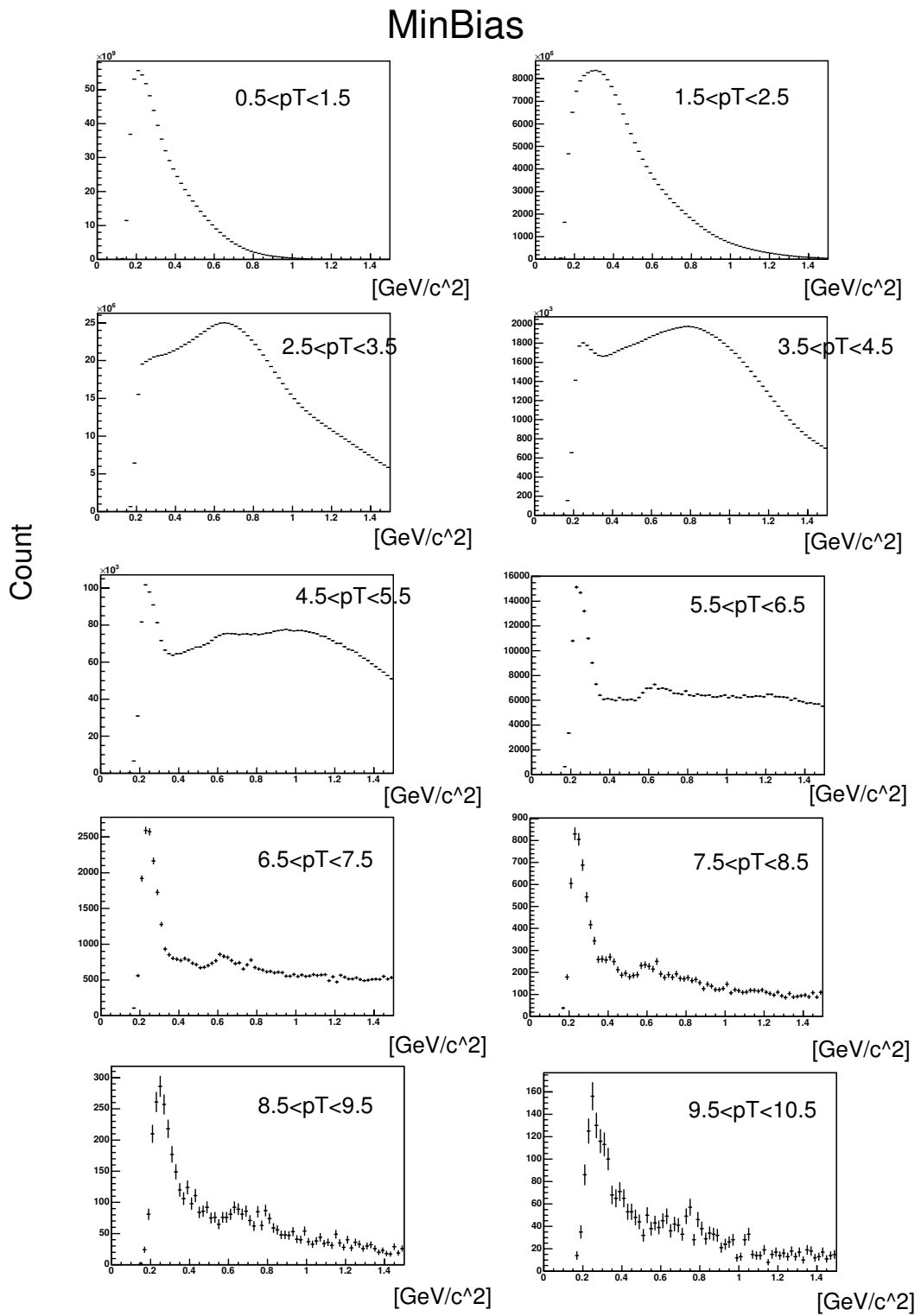


Figure 4.1: The Invariant Mass Spectra at MinimumBias

cent 0-20%

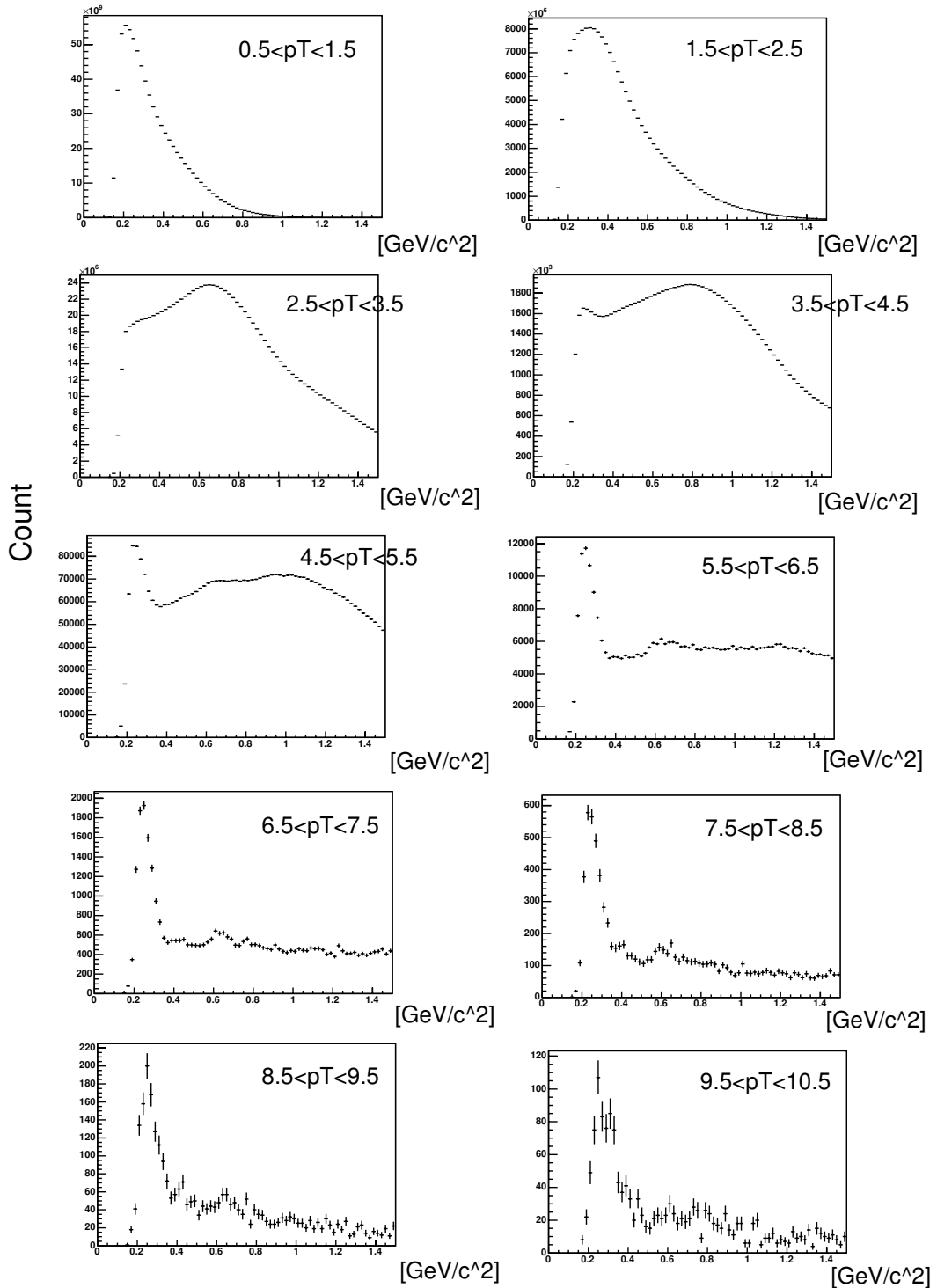


Figure 4.2: The Invariant Mass Spectra at 0-20% central

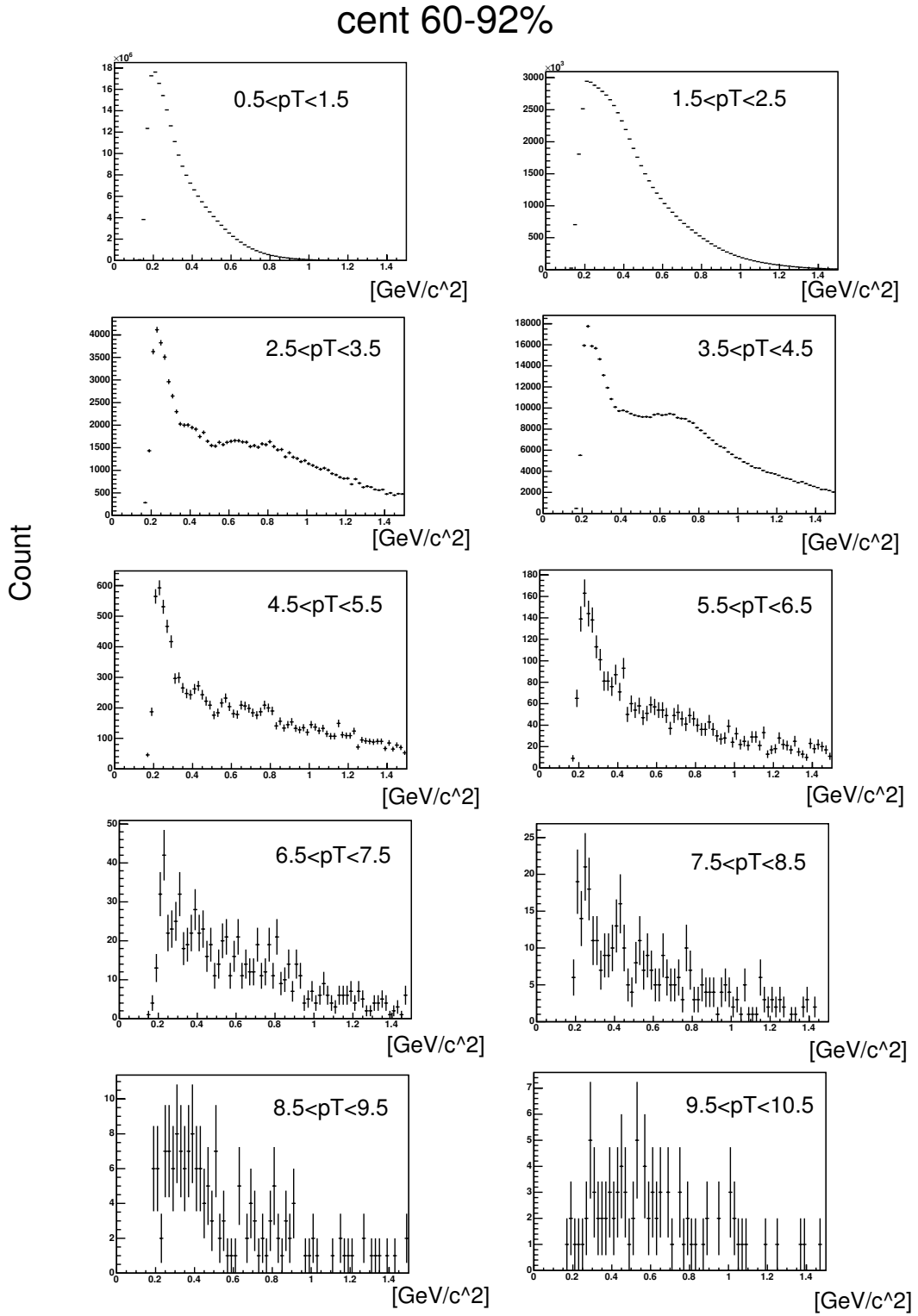


Figure 4.3: The Invariant Mass Spectra at 60-92.2% central

4.2 Background Consideration

4.2.1 Combinatorial Background

We reconstruct ω via radiative decay mode, 3γ . It leads to produce huge background due to their multiple combinations. Such conceivable combinations are lined in the Figure 4.5. We first reconstruct 2γ and set as " π^0 candidate" by selecting the invariant mass within 1.25σ or 1.5σ (see the table of Cut#4), but there's a probability that the uncorrelated 2γ satisfies the criteria of π^0 candidate. The shape of reconstructed invariant mass shows the behavior of such combination (see the Figure 4.4). The high peak in the low mass region, around $0.2\sim 0.4(\text{GeV}/c^2)$ is due to the combination of $\pi^0\gamma(\pi^0 \rightarrow 2\gamma)$ failed to reconstruct ω ("Fail1" and "Fail2" in the Figure 4.12 correspond to it). And the another peak around $0.5\sim 0.7(\text{GeV}/c^2)$ is due to the combination of $\eta\gamma(\eta \rightarrow 2\gamma)$ ("Fail1" in the Figure 4.12). Those peaks are slightly above their mesons since the additional energy of photons (besides their decay photons) are used to reconstruct them.

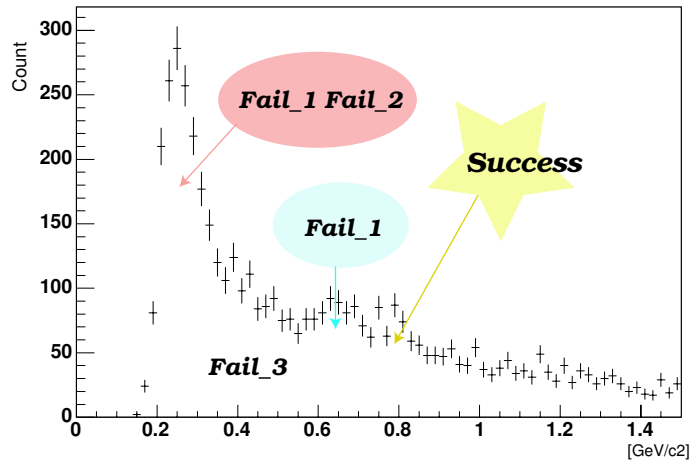


Figure 4.4: The combination behaviour in the invariant mass (picked the MinBias at $6.5 < p_T < 7.5$ for example).

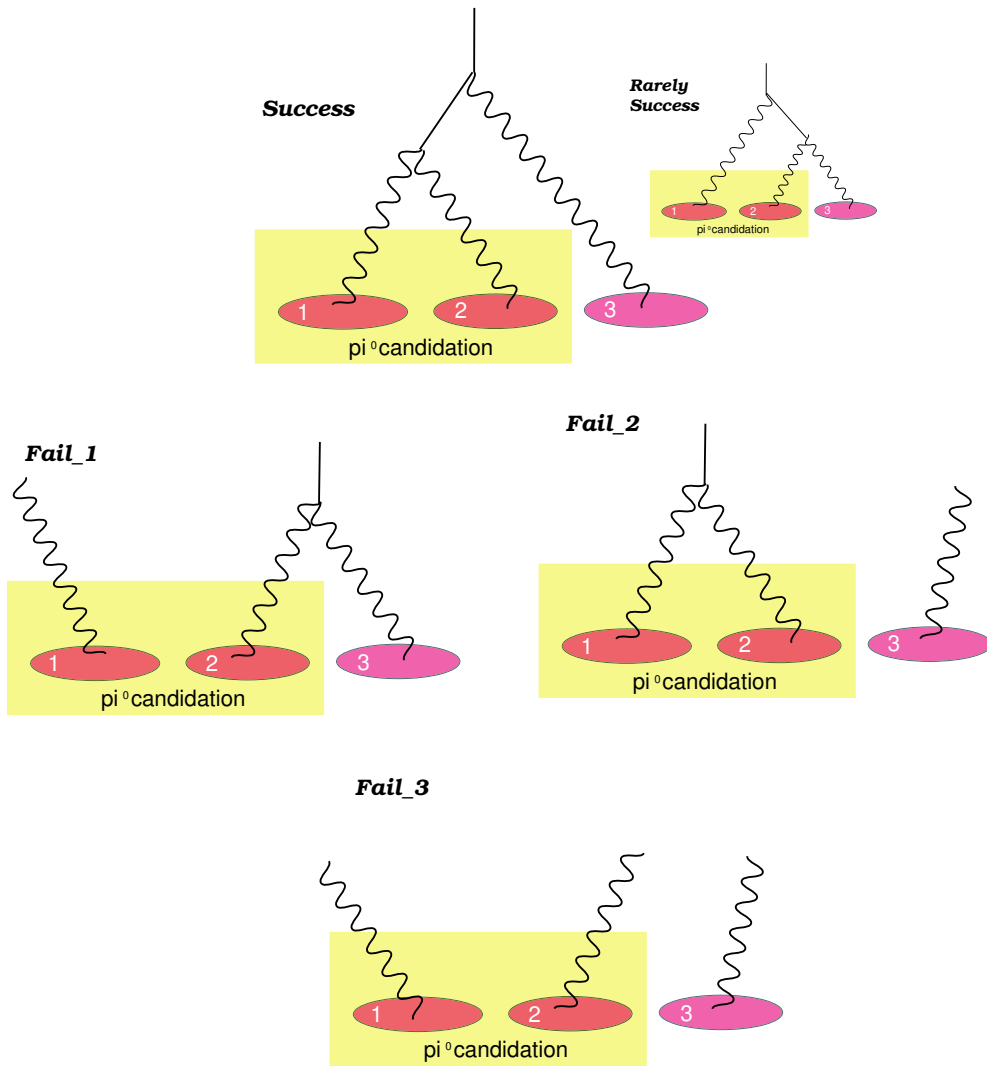


Figure 4.5: Conceivable combinations during 3γ reconstruction. Suppose γ_1 and γ_2 are the π^0 candidate (selected as π^0 mass) that we reconstruct first.

4.2.2 Mixed Events Trail

The *event mixing* method is a widely used technique to determine the combinatorial background. The Figure 4.6 shows a schematic of the *event mixing*. The basic idea is to compare the result obtained by combining particles within one event to the result for particle combinations from different events, which are a priori not correlated. It is usually used for two pair reconstruction, such as π^0 and η . Before going to ω reconstruction, We extract the mean and the width of π^0 by using this method. The Figure 4.7 shows the invariant mass spectra of π^0 for each $\pi^0 p_T$. The foreground (reconstructed with same event) and the background (reconstructed with mixed event) are drawn together on the left side for each p_T . Right side of the plot is the spectra after subtraction of the background. Obviously, π^0 stands out after subtraction of the *event mixing*. Although it is not simple in the case of multiple decay mode, we consider this method for this analysis since ω can't be seen so clearly due to combinatorics.

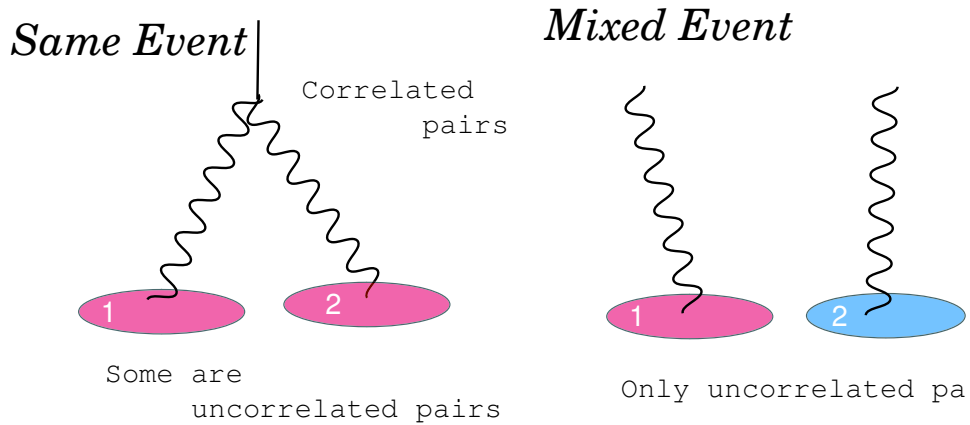


Figure 4.6: A schematic of Event mixing. Red and Blue γ image is coming from different events.

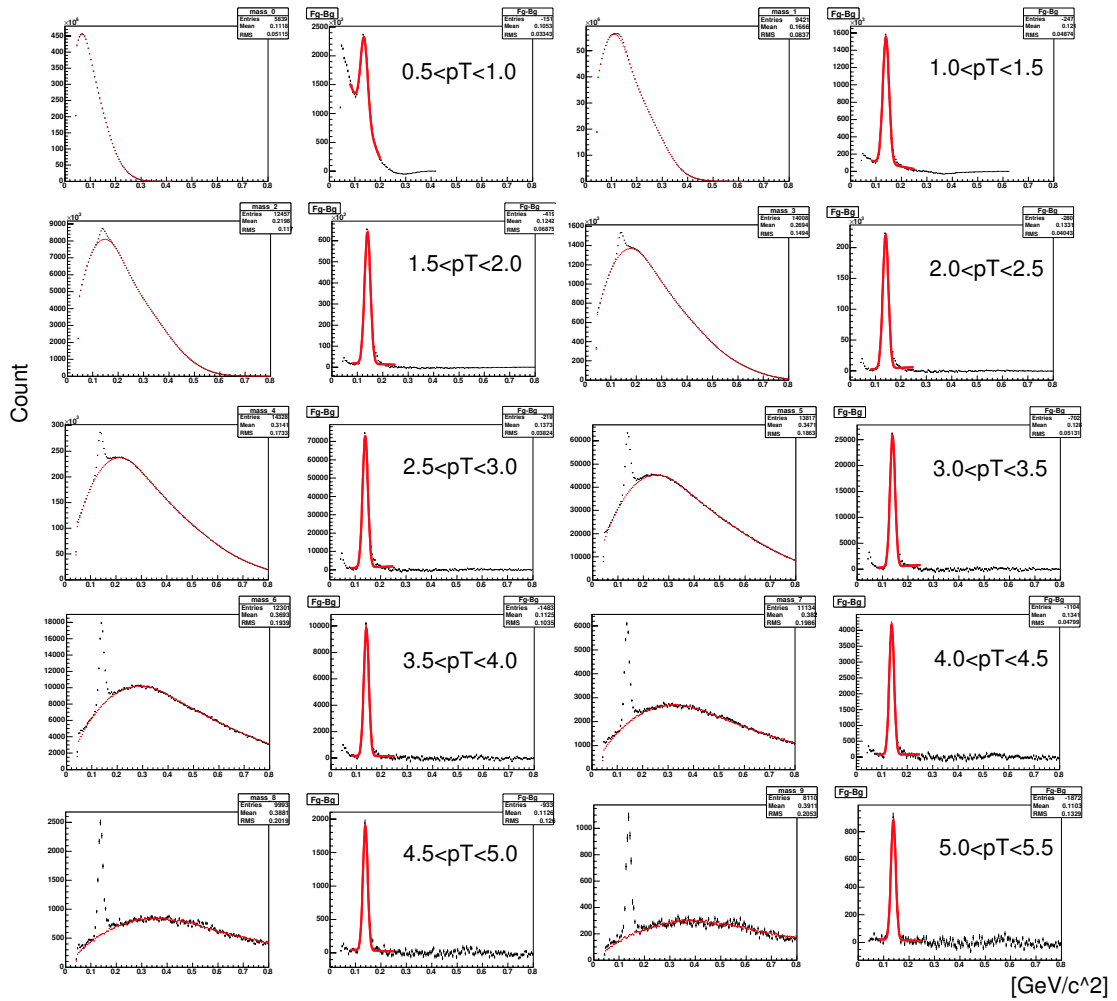


Figure 4.7: Invariant Mass Spectra of π^0 .

There are 3 ways to mix events in the 3 decay mode as shown in the Figure 4.8; I. π^0 candidate is selected from the same event (having a correlation) and chose a different event for third photon, II. π^0 candidate is selected from different events (having no correlation) and chose third photon as the same event with one of the candidate. III. All 3 photons are different events. First we try Method I., however, the event mixing spectra seems too differ-

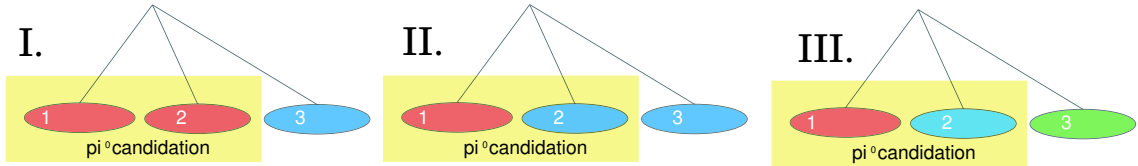


Figure 4.8: A schematic of Event mixing for 3 decay mode

ent from the foreground shape especially in the lough mass region (see the Figure 4.9) and can't be considered as "background". The main background

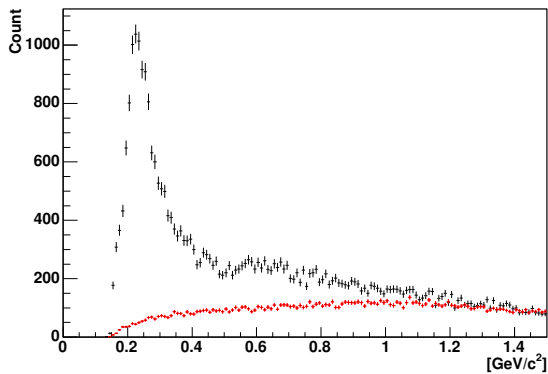


Figure 4.9: Example plot of the event mixing of Method I (red line) with the foreground plot (black line).

ω mass as green line in the subtracted mass spectra; the peak position and the width are coming from the embedding simulation and integrated number is coming from the N_ω estimation (see the Table 3.3.5).

we want to exclude is coming from the correlation between the one of π^0 candidate and third photon, i.e. "Fail1" in the Figure 4.5. It turns out that Method II. is including this correlation and create the " $\pi^0\gamma$ " and " $\eta\gamma$ " spectrum. We introduce this method and compare the results with foreground spectrum. Following figures shows the comparison between foreground and *mixing event* scaling down by the fit region of 1.2-1.4 (GeV/c^2). The results after subtraction of *mixing event* are shown on the right side. We also draw the simulated

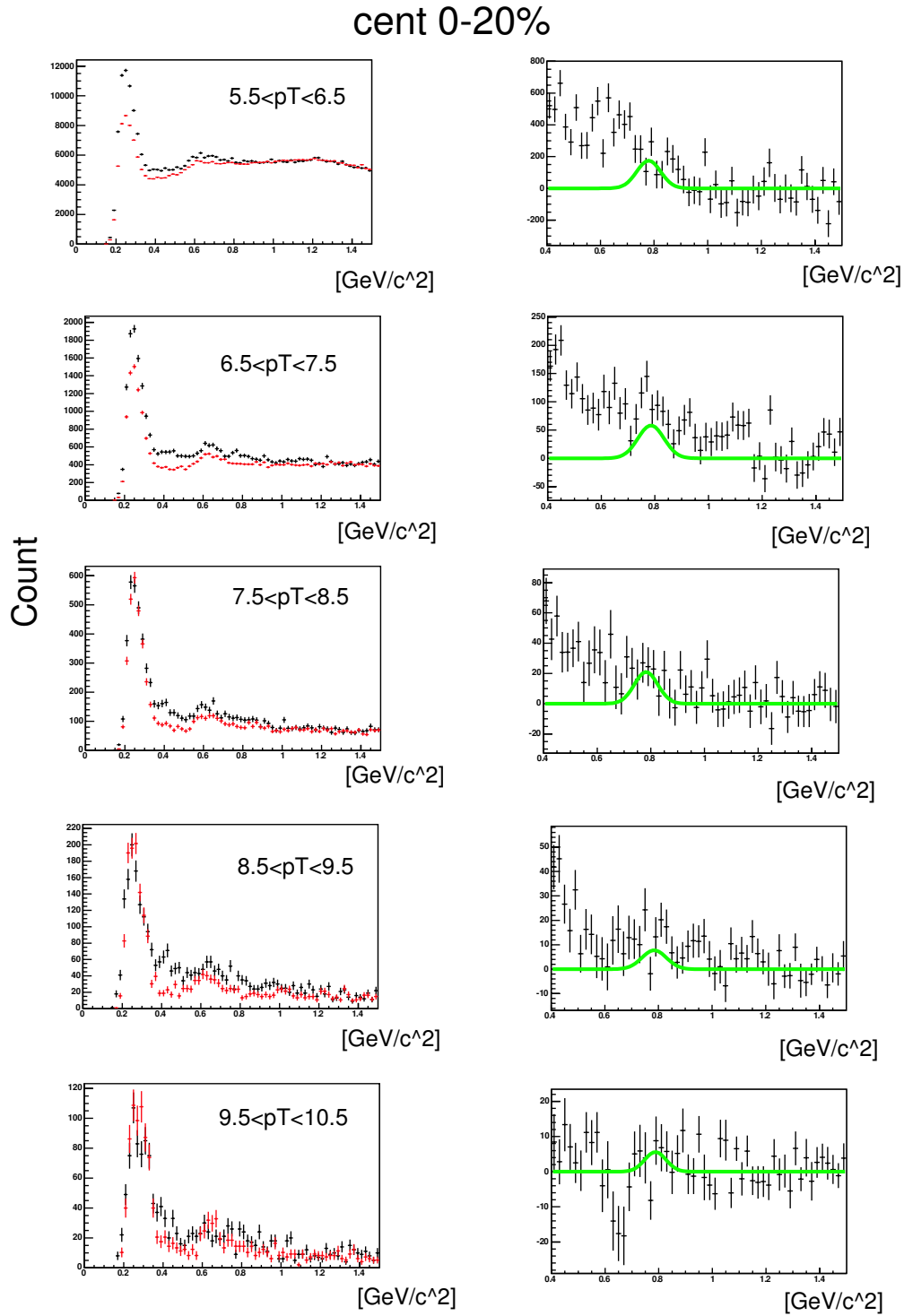


Figure 4.10: Comparison between the foreground(black lines) and background using Method II.(red lines) on the left, and the subtracted spectra on the right at 0-20 % centrality collisions. Green lines denote the expected ω mass calculated by simulation.

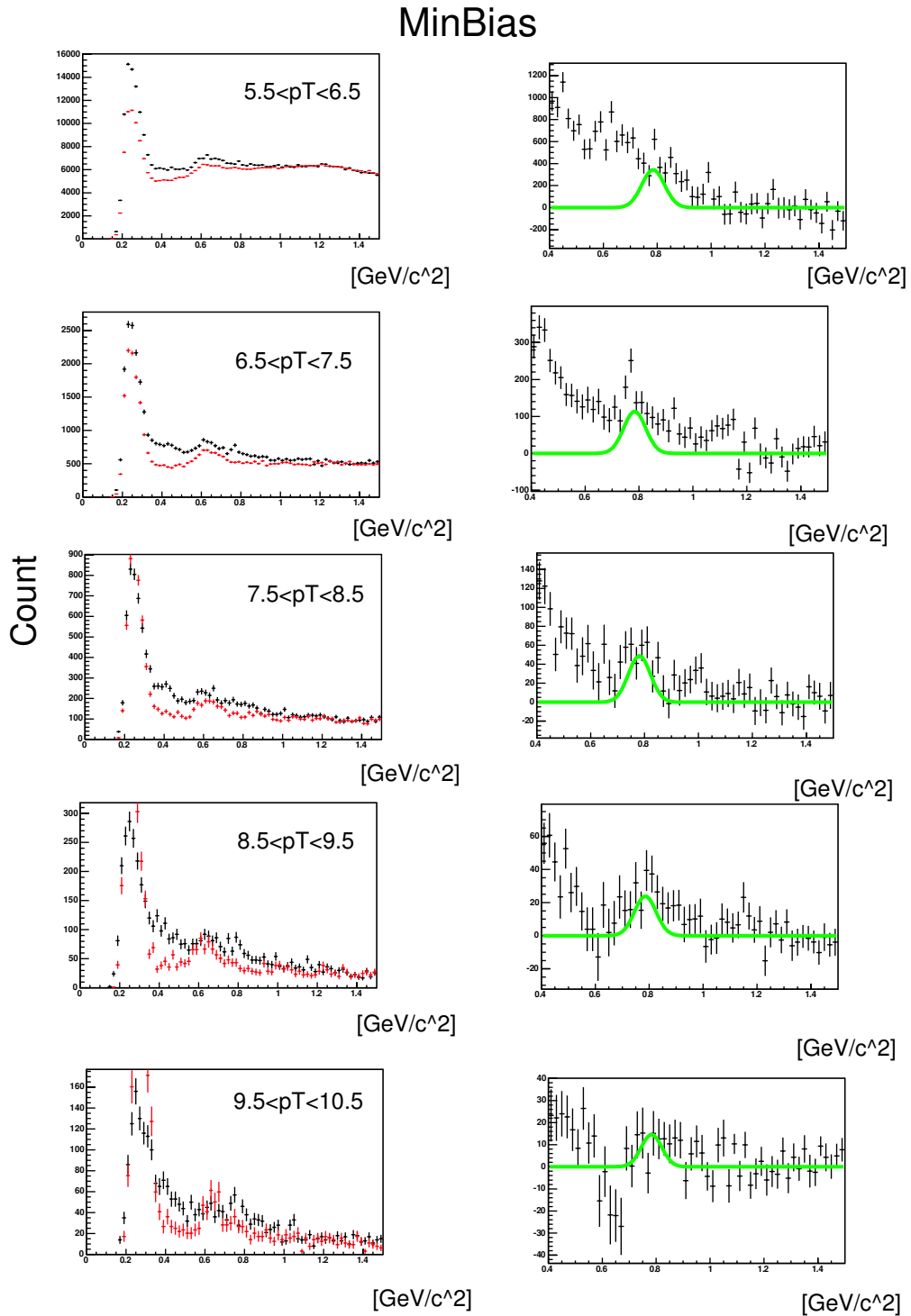


Figure 4.11: Comparison between the foreground (black lines) and background using Method II. (.) (red lines) on the left, and the subtracted spectra on the right at Minimum Bias collisions. Green lines denote the expected ω mass calculated by simulation.

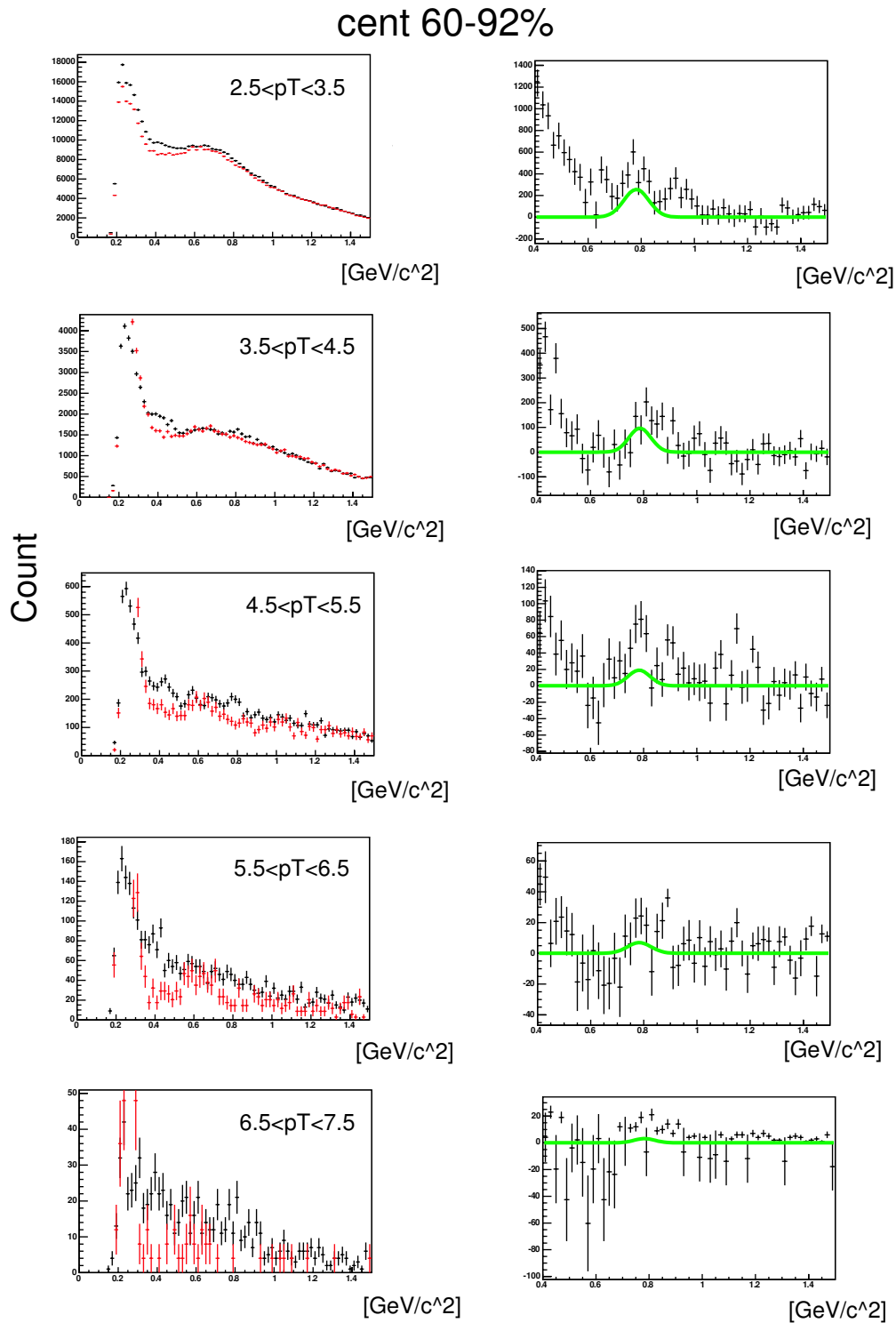


Figure 4.12: Comparison between the foreground(black lines) and background using Method II.(.) (red lines) on the left, and the subtracted spectra on the right at 60-92 % centrality collisions.

4.3 Outlook

From the results, we can see the conceivable ω mesons plateau and it shows not inconsistent with the simulated ω meson, however, it is hard to evaluate the values such as yield, peak and width. The more fully subtraction of background additional to the *event mixing* is needed. We're going to push forward simulation study and see the other particle's contribution, such as $K_S \rightarrow \pi^0\pi^0$ and also evaluate the ω to π^0 ratio in the Au+Au collisions. This particle contribution works will allow to extract the background in detail and help to approach the low momentum region where the in-medium modification mainly dominate.

Other thing we're going to touch is the systematic study. Cu+Cu collisions are also taken at PHENIX during 2004-2005, and the calibration is on-going. We will also analysis $\omega \rightarrow \pi^0\gamma$ in this different multiplicity (lower than Au+Au, and so ω mesons can be identified relatively clear) and see the differences. More statistics of Au+Au collisions are expected to taken in the near future and there is no reason not to analyze them, too.

Chapter 5

Conclusion

We measure ω mesons via radiative decay mode in Au+Au collisions at C.M.S. collisions energy per nucleon pair of 200GeV. The simulation is carried out in advance to calculate an acceptance and to check a multiplicity. Furthermore, we search the best cuts; transverse momentum of π^0 , energy of γ and width of π^0 mass; that improve S/\sqrt{B} the most by using both simulation and real data. After applying determined best cuts, it turns out S/\sqrt{B} goes up to 4 for all statistics and it is sufficiently possible to measure ω mesons in the heavy ion collisions.

Seeing the results of reconstructed invariant mass after applying the best cuts, ω appears in the high p_T region, however, the combinatorial background especially the contribution of " $\eta\gamma$ " makes them hide. To try to extract them, we introduce *event mixing* method and subtract the background that correlating to " $\eta\gamma$ ". Finally, ω mesons come to appear more than before the subtraction. The further analysis to evaluate parameters such as yield, mean and width of ω mesons is on-going.

Acknowledgment

First, I would like to express my gratitude to Prof. Kenta Shigaki who mainly supervise this work. The study of ω mesons via radiative decay mode at RHIC is coming from his idea. Prof. Toru Sugitate, the boss of our laboratory gave me many chances to go to the BNL and international conferences. Needless to say, those experiences had been good educations and strongly helped to maintain my motivation. I appreciate Sasha Milov who instructed me the vector mesons' analysis in the BNL and Chris Pinkenburg who had been taking care of the computing system. Dr. Kensuke Homma and Dr. Hisayuki Torii gave me crucial suggestions a lot and helped an improvement of this analysis. I would like to thank Dr. Takuma Horaguchi, Tomoaki Nakamura, Yuji Tsuchimoto and Yoshihide Nakamiya for giving me precious advices and teaching some computing techniques. I also give my thanks to Kazuhisa Yamaura and Megumi Oki for the mutual encouragement.

I could not keep working without the existence of my family. It is impossible to fully express my thanks to my father and mother; Nobuyuki and Chizuko, two brothers; Tomoki and Tsukasa, and two sisters; Killa and Laicca. In the end, I would like to dedicate this thesis to my best partner, John, who had been with me for 13 years and passed away in 2006 February.

Appendix A

Kinematics

Here, we describe the coordinate and kinematic variables that are used in the relativistic heavy ion experiments.

Coordinate

The coordinate system for the experiment is shown in the Figure A.1. The axis of collision (beam axis) is defined as the z axis. Components along the beam axis are called as the *longitudinal* components, while components lying in the x - y plane are called as the *transverse* components. ϕ is the polar angle measured from the z axis and θ is the azimuthal angle measured clockwise from the x axis.

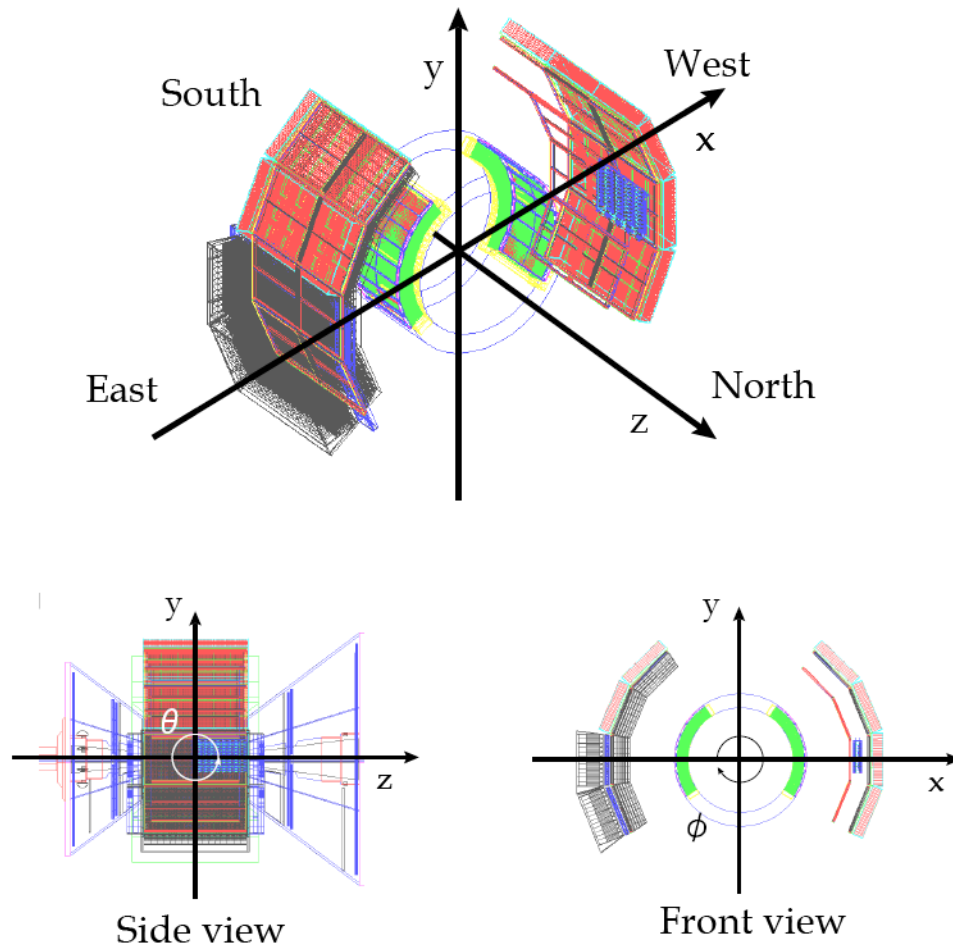


Figure A.1: Coordinates of the PHENIX experiment

Energy and Momentum

The relativistic energy allows to use the natural units, $c = \hbar = 1$. So then the energy of the particle is written as,

$$E = \sqrt{\mathbf{p}^2 + m^2},$$

and the momentum composed of 4-vectors is written as,

$$p = (E, \mathbf{p}),$$

The component along the beam-axis, the *longitudinal* momentum is defined as,

$$p_z = p \cos \theta,$$

where p is the magnitude of particle's momentum. While the *transverse* momentum, which is a Lorentz invariant is given as,

$$p_T = \sqrt{p_x^2 + p_y^2} = p \sin \theta.$$

Rapidity and Pseudorapidity

The longitudinal variable, the rapidity y , is commonly used. It is defined as,

$$y = \frac{1}{2} \ln \left(\frac{E + p_z}{E - p_z} \right) = \frac{1}{2} \ln \left(\frac{1 + \beta \cos \theta}{1 - \beta \cos \theta} \right)$$

If we go to higher energy that the momentum relatively much higher than the mass, i.e. $E \simeq p$, the rapidity is translated as the *pseudorapidity* defined as,

$$\eta = -\frac{1}{2} \ln \left(\tan \frac{\theta}{2} \right).$$

Bibliography

- [1] Frank Wilczek, Physics Today August 2000, p.22
- [2] Mikhail A.Stephanov, Int.J.Mod.Phys.A20:4387-4392(2005)
- [3] P.Braun-Munzinger, K.Redlich and J.Stachel, nucl-th/0304013
- [4] Itzhak Tserruya, talk in the PHENIX Focus 2006
- [5] W.-M.Yao *et al.*, Journal of Physics G 33,1(2006)
- [6] R.Rapp and J.Wambach, hep-ph/9909229v1(1999)
- [7] Y.Nambu and G.Jona-Lasinio, Phys.Rev.122,345-358(1961)
- [8] C.Djalali for the CLAS Collaboration, talk in the Quark Matter 2006
- [9] K.Adcox *et al.*, Nucl.Phys.A757,184-282(2005)
- [10] R.Rapp, nucl-th/0608022
- [11] R.Rapp, H.Hees and T.Strong, hep-ph/0611339
- [12] M.F.M.Lutz, Gy.Wolf and B.Friman, Nucl.Phys.A706,431-496(2002)
- [13] T.Hatsuda and S.H.Lee, Phy.Rev.C46(1992)R34
- [14] R.Rapp and J.Wambach, hep-ph/9909229v1(1999)
- [15] Volker Metag, talk in the Quark Matter 2006
- [16] M.Naruki *et al.*, Phys.Rev.Lett.96,092301(2006)
- [17] KEK-PS E325 Collaboration: R.Muto *et al.*, nucl-ex/0511019

- [18] C.Djalali, talk in the Quark Matter 2006
- [19] CBELSA/TAPS Collaboration: D.Trnka *et al.*, Phys.Rev.Lett.94,192303(2005)
- [20] CERES Collaboration: D.Adamova *et al.*, nucl-ex/0611022
- [21] NA60 Collaboration: R.Arnaldi *et al.*, Phys.Rev.Lett.96,162302(2006)
- [22] J.G.Messchendorp *et al.*, Eur.Phys.J.A11,95(2001)
- [23] P.Mühlich *et al.*, Eur.Phys.J.A20,499(2004)
- [24] A.Sibirtsev *et al.*, Phys.Lett.B483,405(2000)
- [25] RHIC Official Website, <http://www.bnl.gov/rhic/>
- [26] PHENIX Official Website, <http://www.phenix.gov/>
- [27] K.Adcox *et al.*, Nuclear Instruments and Methods A499 469-479(2003)
- [28] M.Allen *et al.*, Nuclear Instruments and Methods A499 549-559(2003)
- [29] H.Akikawa *et al.*, Nuclear Instruments and Methods A499 537-548(2003)
- [30] K.Adcox *et al.*, Nuclear Instruments and Methods A499 489-507(2003)
- [31] Y.Tsuchimoto for the PHENIX/BBC group, Talk in the PHENIX Focus 2004
- [32] C.Adler *et al.*, Nuclear Instruments and Methods A499 433-436(2003)
- [33] S.H.Aronson *et al.*, Nuclear Instruments and Methods A499 480-488(2003)
- [34] K.Adcox *et al.*, Nuclear Instruments and Methods A499 489-507(2003)
- [35] M.Aizawa *et al.*, Nuclear Instruments and Methods A499 508-520(2003)
- [36] S.Takagi *et al.*, Talk in the PHENIX Focus 2004
- [37] L.Aphecetche *et al.*, Nuclear Instruments and Methods A499 521-536(2003)

- [38] Hisayuki Torii, Ph.D. thesis at Kyoto University (2004)
- [39] Chirstian Klein-Bösing, Ph.D. thesis at the Westfälischen Wilhelms-Universität Münster (2005)
- [40] S.S.Adler *et al.*, Nucl.Instr.Meth.A499 560-592 (2003)
- [41] Chris Pinkenburg, talk in the Spin Festa in 2006
- [42] A Primer Manual for PISA, <http://www.phenix.gov/phenix/WWW/simulation/primer4/>
- [43] CERN Official Website, <http://www.cern.ch>
- [44] A Primer Manual for PISA, <http://www.phenix.gov/phenix/WWW/simulation/primer4/>
- [45] CERN Official Website, <http://www.cern.ch>
- [46] Embedding software, <http://www.phenix.gov/phenix/WWW/simulation/primer4/>
- [47] S.S.Adler *et al.*, Phys.Rev.Lett.91:241803(2003)
- [48] S.S.Adler *et al.*, nucl-ex/0611031
- [49] Glauber Results, <https://www.phenix.bnl.gov/phenix/WWW/p/draft/reyers/glauber>